

ABSTRACT

MAKALA, Raghuveer Satya. Pulsed Laser Deposition of Bi_2Te_3 based thermoelectric thin films. (Under the guidance of Dr. Jagannadham Kasichainula.)

Thin film thermoelectric coolers offer several advantages that include reliability and integration with device processing. Successful thin film thermoelectric cooling requires integration with thin film diamond or aluminum nitride heat spreaders and the device wafers. Numerous deposition techniques have been attempted previously including evaporation, flash evaporation, molecular beam epitaxy, chemical vapor deposition, and sputtering. In the case of thermoelectric thin films, a primary difficulty is maintaining stoichiometry. In the present effort, thin films of p-type $\text{Bi}_{0.5}\text{Sb}_{1.5}\text{Te}_3$, n-type $\text{Bi}_2\text{Te}_{2.7}\text{Se}_{0.3}$ and n-type $(\text{Bi}_2\text{Te}_3)_{90}(\text{Sb}_2\text{Te}_3)_5(\text{Sb}_2\text{Se}_3)_5$ (with 0.13 wt.% SbI_3) were deposited on mica and aluminum nitride substrates using Nd-YAG pulsed laser deposition.

The film quality in terms of composition and crystal perfection was studied as a function of growth temperature. The films were characterized by X-ray diffraction (XRD), transmission electron microscopy (TEM) for crystalline quality, and by scanning electron microscopy (SEM) for surface morphology. The films showed uniform thickness and high crystalline quality with a preferred (0 0 n) alignment with the substrates. The Seebeck coefficient, electrical resistivity and Hall mobility were measured and compared with the bulk properties. An improvement in the thermoelectric properties by reduction in laser induced particulates has been demonstrated by the use of lower incident laser energy. The thermoelectric characteristics of the films deposited on AlN/ Si substrates were found to be superior to those deposited on mica substrates. X-ray mapping and

energy-dispersive-spectroscopy were performed to determine the composition and homogeneity of the thin films. The results showed that pulsed laser deposition has the ability to produce congruent transfer of the target composition to the thin films under the suitable conditions of lower laser fluence, low density plume and ideal substrate temperature. The present work has illustrated the use of AlN/ Si (an efficient heat spreader) as a favorable substrate material for thin film deposition. Thus, it has been shown that there exists great potential for producing efficient thermoelectric thin films by means of pulsed laser deposition. In addition, the ability to deposit nanocrystalline thermoelectric thin films has also been demonstrated.

Pulsed Laser Deposition of Bi_2Te_3 based thermoelectric thin films

By

RAGHUVeer S. MAKALA

A dissertation submitted to the Graduate Faculty of
North Carolina State University
in partial fulfillment of the
requirements for the Degree of
Master of Science

DEPARTMENT OF MATERIALS SCIENCE AND ENGINEERING

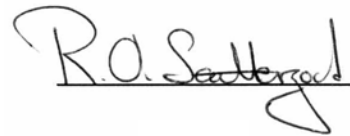
RALEIGH, NORTH CAROLINA

2002

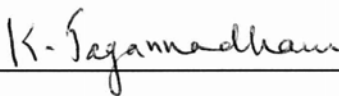
APPROVED BY:



Dr. C.M. Osburn
Electrical & Computer Engineering
Minor representative



Dr. R.O. Scattergood
Materials Science & Engineering
Member



Dr. K. Jagannadham
Materials Science & Engineering
Chair of advisory committee

PERSONAL BIOGRAPHY

Raghuveer S. Makala was born on 22nd March 1979 in Visakhapatnam, India. He started his education at B.H.P.V. Senior Secondary School and completed his high school education from Mrs. A.V.N. College in 1996. After that, he attended Andhra University, Visakhapatnam, for his undergraduate studies. While at Andhra University, he worked with Dr. N.R. Bhargava on Al-Mg alloys and cored extrusion. He obtained a Bachelor's degree with distinction in Metallurgical Engineering at Andhra University in May 2000 and was also awarded the K. Linga Murty gold medal. In August 2000, he joined the graduate program in the Department of Materials Science & Engineering at North Carolina State University, Raleigh, NC, USA. During his graduate studies, he conducted research in the Deposition and Characterization of Semiconductor Thin Films under the guidance of Dr. Jagannadham Kasichainula.

ACKNOWLEDGEMENTS

First of all, I would like to thank Dr. Jagannadham Kasichainula, my advisor, for all the encouragement while working on this project. I would like to thank him for his constant support, training, guidance, and patience throughout the course of my study. I would also like to thank Dr. Ronald Scattergood and Dr. Carlton Osburn for agreeing to be on my advisory committee and their helpful comments.

I sincerely appreciate Dr. W.A. Jesser of the University of Virginia and Dr. J.W. Sharp of Marlow Industries for supplying us with the target materials. I would like to thank Dr. B. C. Sales of Solid State Division, Oak Ridge National Laboratory for his help and advice in conducting thermopower measurements. I would like to thank Dr. Hsin Wang of ORNL for allowing me to use the facilities in HTML. I would like to thank Southeastern Universities Research Association, SURA and Oak Ridge Associated Universities, ORAU for supporting this research effort. I would also like to thank Mr. Roberto Garcia and Ms. Laura Smith of AIF for training me initially in the use of SEM and helping me when I encountered problems. I also thank my friend and erstwhile group member Mr. Yoganand Saripalli for good discussions and support during the course of my research. I also thank Mr Kiran Sagi for the accommodation provided and making my stay at Oak Ridge-Knoxville a pleasurable and memorable one. I would like to thank all the staff of the Department of Materials Science and Engineering, especially Ms. Edna Deas for being so helpful during my entire MS program.

This research work was also partly supported by National Science Foundation. Part of this research was also sponsored by the assistant secretary for energy efficiency and renewable energy, Office of Transportation Technologies, as part of the High

Temperature Materials Laboratory fellowship program, Oak Ridge National Laboratory, managed by UT-Battelle, LLC, for the U.S. Department of Energy.

I would like to thank my ever-reliable friends: Aashika, Sai, Ravi, and Srikanth for sharing the ups and downs in my life. I also thank my roommates: Naresh, Srinivas, Kamesh and Dipankar for making me feel at home, away from home. Last but not the least, I would like to thank my family – my parents, my brother Srinivas for their unconditional love and support. If not for them, I would not have been what I am today.

TABLE OF CONTENTS

LIST OF TABLES	viii
LIST OF FIGURES	ix
CHAPTER 1 INTRODUCTION	1
§ Motivation	7
§ References	9
CHAPTER 2 LITERATURE REVIEW	12
§ 2.1 History and Development	13
§ 2.2 Bi ₂ Te ₃ based materials	14
§ 2.3 Pulsed Laser Deposition	21
§ 2.4 Deposition of Bi ₂ Te ₃ based thermoelectric thin films	26
§ 2.5 Growth of aluminum nitride	28
§ 2.6 Characterization Techniques	32
§ 2.6.1. <i>X-ray Diffraction</i>	32
§ 2.6.2 <i>Scanning Electron Microscopy</i>	33
§ 2.6.3. <i>EDS, X-ray mapping and Quantitative analysis</i>	35
§ 2.6.4 <i>Transmission Electron microscopy</i>	36
§ 2.6.5 <i>Electron Energy Loss Spectroscopy</i>	37
§ 2.6.6 <i>Determination of thermopower</i>	37
§ 2.6.7 <i>Hall mobility</i>	38
§ References	39

CHAPTER 3	EXPERIMENTAL DETAILS	44
§	3.1 Growth	45
§	3.2 Deposition of aluminum nitride	46
§	3.3 PLD of thermoelectric thin films	47
§	3.4 Characterization	50
§	3.4.1 <i>X-ray Diffraction</i>	50
§	3.4.2 <i>Scanning electron microscopy</i>	50
§	3.4.3 <i>Transmission electron microscopy</i>	51
§	3.4.4 <i>Electron Energy Loss Spectroscopy</i>	52
§	3.4.5. <i>Thermopower Measurements</i>	52
CHAPTER 4	RESULTS	54
§	4.1 X-ray diffraction	55
§	4.2 Scanning electron microscopy	57
§	4.3 Transmission electron microscopy	59
§	4.4 Measurement of Thermopower	60
§	4.5 Hall-effect Measurements	61
CHAPTER 5	DISCUSSION	63
§	5.1 X-ray diffraction	64
§	5.2 Scanning electron microscopy	65
§	5.3 Transmission electron microscopy	67
§	5.4 Transport Properties	69
§	References	72
CHAPTER 6	CONCLUSIONS	73

§	6.1. Conclusions	74
§	6.2 Future Work	75

LIST OF TABLES

Table 2.2.1 Crystal structure, average atomic mass and bandgap of Bi_2Te_3 , Sb_2Te_3 , and Sb_2Se_3	77
Table 2.5.1 Fundamental properties of aluminum nitride	77
Table 3.1 Summary of characterization techniques	78
Table 4.2 Composition analysis of films deposited at 350°C using energy dispersive spectroscopy	79
Table 4.4.1 Thermopower and Hall-Mobility experimental data obtained on films deposited on mica substrates	80
Table 4.4.2 Thermopower and Hall-Mobility experimental data obtained on films deposited on aluminum nitride substrates	81
Table 4.4.3 Thermopower values obtained on films deposited on $\text{AlN}/\text{Si}(100)$ substrates at better pre-deposition vacuum	82
Table 5.4.1 Summary of best values of the films in terms of the highest Seebeck values, highest mobility and highest carrier concentration	82
Table 5.4.2 Best values of ZT obtained on n-type and p-type films	83
Table 5.4.3 Values of ZT reported on n-type and p-type target materials	83

LIST OF FIGURES

Fig. 1.1 Schematic showing thin film thermoelectric device integrated with diamond substrates. The proposed metallization and bonding scheme can also be seen	84
Fig. 2.1.1 Schematic showing a single thermocouple that constitutes a simple thermoelectric cooling sub-assembly. The labels p (positive) and n (negative) refer to the sign of the charge carriers in each leg, where as filled circles correspond to electrons and open circles correspond to holes	85
Fig. 2.2.1 Crystal structure of the Bi_2Te_3 unit cell	86
Fig. 2.2.2 Representation of the dependence of thermoelectric power S , electrical conductivity σ , thermal conductivity K , and the product of $S^2\sigma$ on the extent of extrinsic charge carriers	87
Fig. 2.2.3 Plot of figure of merit, Z as a function of Seebeck coefficient for Bi_2Te_3 at 300 K. The upper curves illustrate the higher values of Z possible with ternary alloys	88
Fig. 2.3.1 Illustration of basic thermal cycle induced by laser pulsing. (a) absorption of laser plume and beginning of melting and vaporization, shaded area indicates molten material, arrows indicate motion of solid- liquid interface (b) advancing of melt front into solid, accompanied by vaporization (c) melt front receding, cross hatched region indicates re-solidification (d) complete re-solidification, frozen capillary waves alter topography	89
Fig. 2.3.2 Schematic illustrating the various mechanisms responsible for splashing. (a) Subsurface boiling, (b) Shock wave recoil, and (c) Exfoliation	90
Fig. 2.5.1 Crystal structure of the AlN unit cell	91

Fig. 2.6.6.1 Specimen support plate used for measurement of Seebeck coefficient	92
Fig. 2.6.7.1 Specimen configuration used for Van-der-Pauw technique and Hall effect measurements	93
Fig. 3.3.1 Schematic of PLD experimental set-up used in this study	94
Fig. 4.1.1 (a) θ -2 θ x-ray diffraction scan obtained on $\text{Bi}_{0.5}\text{Sb}_{1.5}\text{Te}_3$ ingot used as a target material	95
Fig. 4.1.1 (b) θ -2 θ x-ray diffraction scan obtained on $\text{Bi}_2\text{Te}_{2.7}\text{Se}_{0.3}$ ingot used as a target material	95
Fig. 4.1.1 (c) θ -2 θ x-ray diffraction scan obtained on $(\text{Bi}_2\text{Te}_3)_{90}(\text{Sb}_2\text{Te}_3)_5(\text{Sb}_2\text{Se}_3)_5$ (+ 0.13 % wt SbI_3) ingot used as a target material	96
Fig. 4.1.2 (a) θ -2 θ x-ray diffraction scan obtained on $\text{Bi}_{0.5}\text{Sb}_{1.5}\text{Te}_3$ thin films deposited on mica substrates	96
Fig. 4.1.2 (b) θ -2 θ x-ray diffraction scan obtained on $\text{Bi}_2\text{Te}_{2.7}\text{Se}_{0.3}$ thin films deposited on mica substrates	97
Fig. 4.1.2 (c) θ -2 θ x-ray diffraction scan obtained on thin films deposited on mica substrates using a $(\text{Bi}_2\text{Te}_3)_{90}(\text{Sb}_2\text{Te}_3)_5(\text{Sb}_2\text{Se}_3)_5$ (+ 0.13 % wt SbI_3) target	97
Fig. 4.1.3 (a) θ -2 θ x-ray diffraction scan obtained on AlN thin films deposited on Si(1 0 0) substrates by dc reactive magnetron sputtering	98
Fig. 4.1.3 (b) θ -2 θ x-ray diffraction scan obtained on AlN thin films deposited on Si(1 1 1) substrates by dc reactive magnetron sputtering	98
Fig. 4.1.4 (a) θ -2 θ x-ray diffraction scan obtained on thermoelectric thin films deposited on AlN/ Si(1 0 0) substrates	99

Fig. 4.1.4 (b) θ -2 θ x-ray diffraction scan obtained on thermoelectric thin films deposited on AlN/ Si(1 1 1) substrates	99
Fig. 4.2.1 SEM micrograph obtained on n-type films deposited on mica substrates using a high incident laser fluence	100
Fig. 4.2.2 SEM micrograph obtained on n-type films deposited on AlN substrates using a high incident laser fluence	100
Fig. 4.2.3 SEM micrograph obtained on n-type films deposited on AlN substrates using a lowered incident laser fluence	101
Fig. 4.2.4 X-ray map of micrograph obtained on n-type films deposited from the $(\text{Bi}_2\text{Te}_3)_{90}(\text{Sb}_2\text{Te}_3)_5(\text{Sb}_2\text{Se}_3)_5$ (with 0.13 wt.% SbI_3) target on mica substrates using a high incident laser fluence at a low magnification	101
Fig. 4.2.5 X-ray map of micrograph obtained on n-type $\text{Bi}_2\text{Te}_{2.7}\text{Se}_{0.3}$ films deposited on AlN substrates using a high incident laser fluence at a higher magnification	102
Fig. 4.2.4 EDS spectra obtained on p-type films deposited on mica substrates	103
Fig. 4.2.5 EDS spectra obtained on n-type $(\text{Bi}_2\text{Te}_3)_{90}(\text{Sb}_2\text{Te}_3)_5(\text{Sb}_2\text{Se}_3)_5$ (with 0.13 wt.% SbI_3) films deposited on AlN substrates	103
Fig. 4.3.1 (a) Selected Area Diffraction Pattern (SADP) obtained from the mica sheet used as a substrate material	104
Fig. 4.3.1 (b) SADP obtained on the thermoelectric thin films deposited on mica substrates	104
Figs. 4.3.2 (a) and (b) Bright field TEM images obtained on thermoelectric thin films illustrating the presence of hexagon shaped crystallites	104

Fig. 4.3.3 High-resolution lattice image obtained on n-type thermoelectric thin films deposited with the aid of a nanofilter	105
Fig. 4.3.4 Electron energy loss data plot obtained on the nano-structured films shown in fig. 4.3.3	105
Fig. 4.4.1 Plot of Seebeck coefficient or thermopower as a function of temperature for the n-type films deposited at 300°C	106
Fig. 4.4.2 Plot of Seebeck coefficient or thermopower as a function of temperature for the n-type films deposited on mica	106
Fig. 4.4.3 Plot of Seebeck coefficient or thermopower as a function of temperature for the p-type films deposited on mica	107
Fig. 4.4.4 Plot of Seebeck coefficient or thermopower as a function of temperature for the p-type films deposited on AlN	107
Fig. 4.4.5 Plot of Seebeck coefficient or thermopower as a function of temperature for the n-type films deposited on AlN	108
Fig. 5.4.1 Plot of variation of thermoelectric power with carrier concentration for p-type films deposited on mica	109
Fig. 5.4.2 Plot of variation of thermoelectric power with carrier concentration for n-type films deposited on mica	109
Fig. 5.4.3 Plot of variation of thermoelectric power with carrier concentration for p-type films deposited on AlN	110
Fig. 5.4.4 Plot of variation of thermoelectric power with carrier concentration for n-type films deposited on AlN	110

Fig. 5.4.5 Plot of figure of merit, ZT versus carrier mobility for the thermoelectric films deposited on mica	111
Fig. 5.4.6 Plot of ZT versus carrier concentration for thermoelectric films deposited on mica	111
Fig. 5.4.7 Plot of ZT versus carrier mobility for thermoelectric thin films deposited on AlN	112
Fig. 5.4.8 Plot of ZT versus carrier concentration for thermoelectric films deposited on AlN	112

Chapter 1

Introduction

Introduction

Advances in the modern computer era have been accomplished with an increase in the packaging density of electronics that began with the transistor and continue into the new millennium with ultra large-scale integration at the chip level along with the use of multi-chip modules. Increased speed of integrated circuits is accompanied by higher power levels and higher packing densities that result in extraordinary heat dissipation requirements for these devices. Increased packing densities are required for increased processing speed because the signal delay times are directly related to the physical distance between components. In addition faster clock rates necessitate faster logic, and therefore, more power, while increased functional density of processors also result in larger power requirements. On the other hand, the functionality of these devices is affected by the metallization schemes for gates, interconnects, and ohmic contacts. Aluminum and more recently copper are being used for these applications and reliability is affected because of high current densities. Though integrated circuits normally operate in the range of 25 to 80°C, power devices and high power integrated circuits reach temperatures as high as 300°C¹. Metallurgical reactions and impurity redistribution can occur at such high temperatures. Thermally induced mechanisms like grain growth, thermal expansions and residual stresses can severely impact the performance of metallization. Electromigration, reaction of metallization with other layers, especially spiking in the case of aluminum², changes in the resistivity all contribute to device degradation. Thus, high-density electronic circuits require adequate temperature control and efficient heat removal for their proper operation³. Also, advantages of operating electronics at low temperatures include faster switching times, increased speed due to

lower electrical resistance of interconnects, and reduced thermally induced failures^{4 -6}. Hence, operation at lower temperature is considered one of the ways to enhance CMOS performance⁷. The best way is to ensure this by providing an efficient built in active cooling system with the device. Much research has been performed in the choice of an efficient cooling system and it is worth examining the several systems that have been in use.

Cooling techniques can be broadly classified into two categories: conventional and advanced cooling. The former comprises the use of external natural or forced convection and conduction; employing fans, wherein heat is removed by airflow. The hottest components are placed in the center of the board, as heat flow is the greatest there. In such cases, increased cooling is directly proportional to airflow and can be accomplished by using larger and/ or more number of fans. The limitations of using fans include noise and frequent maintenance. Other conventional cooling systems based on conduction employ high thermal conductivity materials such as copper, aluminum, molybdenum etc wherein heat is dissipated to the edges of the board and finally to the heat sinks. In this method, it is desired that the hottest components should be at the periphery of the board. However, both cases of conventional cooling suffer as a result of hot spots and cannot be prevented⁸. To solve the heat-buildup problem several advanced cooling techniques have been developed. In specialty microelectronic devices and laptop computers, microchip manufacturers have added small tubular heat pipes to the surfaces of microchips that help to carry away heat from the hottest circuitry and transfer it to other structural elements. In this case, either the phase change of water or methanol in a closed loop can be used or micro channels embedded in the silicon substrate can be used⁹.

Though this technique has a high heat transfer coefficient it suffers from the fact that the surface connections where tubular heat pipes meet substrate typically conduct heat very poorly and therefore aren't effective heat removers. Spray cooling is another promising method involving the phase change of a dielectric fluid when sprayed onto hot parts. Heat removal is accomplished by phase change from liquid to gas. However, a leak tight system is needed to collect, recondense and pump the fluid. The use of a pump also lends to reliability problems. Currently microelectronics systems use highly conductive materials such as aluminum nitride, diamond etc as heat spreader coatings to dissipate thermal energy to heat sinks.

The application of thermoelectric cooling modules has several advantages. They can be effectively used in spot cooling of discrete devices¹⁰. They also possess the capability of cooling below the ambient which none of the above mentioned cooling techniques possess. This aspect is advantageous in the sense that reliability, lifetime and clockspeed can all be increased. Thermoelectrics also permit the usage of high module heat loads at a particular chip temperature level. Thermoelectric coolers are also very compact, quiet, and absolutely have no moving parts except electrons. They have the ability of handling high heat fluxes and also offer the benefit that the degree of cooling can be easily controlled as a function of current supplied to the thermoelectrics. The main disadvantages of using thermoelectrics is that, they cannot accommodate large heat fluxes as compared to vapor-compression based refrigeration and have a lower coefficient of performance (COP). Also, additional heat could be introduced into the board that would increase the heat output of the device and would have to be removed using high thermal conductivity substrates or by heat pipes¹¹. These factors have basically limited the

thermoelectrics to applications involving low heat flux. Much research has been performed in the development of new bulk materials and thin film microcoolers^{12,13}. The above mentioned properties of thermoelectric coolers enable them to be used for effective cooling of electronic systems. Thermoelectrics can be used for the following thermal management applications:

1. Many high power electronic devices like solid state power amplifiers used in microwave applications require increasing heat dissipation ranging from 5 W to 30 W. These problems of spot cooling can be effectively solved by a combination of diamond substrates and thermoelectric coolers¹⁴.
2. Thermoelectric coolers are widely used in modern optical telecommunications to control the characteristics of laser sources, switching/ routing elements, sensors used in wavelength division multiplexed systems.
3. Operating efficiencies of charge coupled devices, infrared detectors, imaging sensors, laser diodes, and optoelectronic circuits are expected to improve with the use of thermoelectric coolers. Mission critical military equipment used in electronic warfare and radar are bound to benefit with the use of more advanced and reliable coolers.
4. Other applications include low temperature modules in the fields of biology and medicine. Bismuth-Telluride based thermoelectric coolers have been developed for use in DNA amplification and sequencing reactions¹⁵. In another interesting application, a cryoconcentration cell was built using thermoelectric modules and was used to separate orange juice and water¹⁶. Also, thermoelectric cooling has been used for cooling seats in automobiles¹⁷.

There are several potential advantages of using thin film thermoelectric coolers as compared to bulk materials that are listed below:

1. Thermocouples with extremely high aspect ratio of length to width of cross section can be fabricated. As a result, cooling power density can be increased remarkably, since it is inversely proportional to the length of the legs⁸.
2. Thin film coolers allow high packaging density of thermocouples that result in lighter and smaller devices. They could be placed exactly beneath the hottest parts like power amplifier chips allowing closer packaging of components.
3. Thin film deposition technology is also compatible with the planar technology essential to the construction of integrated circuits.
4. Thin film thermoelectric coolers also offer several advantages that include reliability, integration with device processing, lower temperatures that can be achieved and large improvement in lifetime and performance.
5. More number of modules can be produced in a cost-effective manner.

It can be seen that thermoelectric thin films score over bulk materials with their unmatched properties and can thus be used in a wide range of cooling applications. High cost of thermoelectric modules resulting mainly from that of the thermoelectric material is the main reason for limiting their wider use for cooling. At the same time, the thermoelectric material that takes part in the energy conversion is confined to comparatively thin layers near the interface with metal contacts. From this point of view, using thin film thermoelectric devices is most appropriate with electronic components. Micro-miniaturization of thermoelectric cooling is both physically and economically

most attractive. In the present study, the deposition of thermoelectric thin films using Pulsed Laser Deposition (PLD) and its characterization is explored.

Motivation

It is realized that in place of a bonded heat spreader substrate, lower temperatures and higher thermal loads can be handled if thin film thermoelectric coolers integrated with diamond films are deposited directly in contact with discrete or localized devices. Bi_2Te_3 -based materials are well known to be good materials for thermoelectric devices near room temperature. The crystal structure of these materials is composed of atomic layers in the order of $\text{Te/Bi/Te/Te/Bi/Te/Bi/Te/Te/.....}$ oriented along the c-axis and the Te/Te layers are held together by weak Van der Waal forces¹⁸. Ternary compounds: $\text{Bi}_{0.5}\text{Sb}_{1.5}\text{Te}_3$ and $\text{Bi}_2\text{Te}_{2.7}\text{Se}_{0.3}$ have better thermoelectric characteristics for p-type and n-type, respectively. The p-type and n-type thermoelectric components are usually connected in series electrically and in parallel thermally with flow of electrons driven from cold side to hot side and holes vice versa. Electrical contacts made with copper or gold metal pads between p- and n-type are used to transmit thermal loads from the cold to hot side by ceramic plates. When a positive voltage is applied, electrons from low energy p-type are driven to high-energy n-type with the energy transmitted to heat sinks from cold sources. When electrons from n-type return to p-type, energy is dissipated at the heat sinks. The reverse is expected for thermoelectric generators. Hitherto thermoelectric devices are made of long legs with smaller areas, thus with high aspect ratio, but with very thin active regions of energy conversion. The main benefit of thin film thermoelectric coolers is the dramatic increase in cooling power density. However, the figure of merit, a measure of the efficiency of cooling is reduced with decreasing

thickness of the film. Therefore, an optimum thickness for a given cross-section of the thermoelectric films is essential. More importantly, deposition of good quality films of thermoelectrics, diffusion barriers, and metallization schemes is most important for successful development of thin film coolers suitable for electronic devices. It has been further established that the use of diamond or aluminum nitride substrate with high thermal conductivity is necessary to achieve two orders of magnitude higher power density dissipation using the thin film coolers⁸. Successful thin film thermoelectric cooling requires integration with thin film diamond or aluminum nitride substrate heat spreaders and the device wafers to obtain a device of the form shown in figure 1.1. Numerous deposition techniques have been attempted including evaporation, flash evaporation¹⁹, molecular beam epitaxy²⁰, chemical vapor deposition, sputtering²¹, and laser ablation²². A primary difficulty in the deposition of thermoelectric films is maintaining stoichiometry. The growth structure is very important since grain boundaries and crystalline defects effect the resistivity by scattering charge carriers. In the present effort, we have used pulsed laser deposition²³. Pulsed laser deposition (PLD) has the advantage of maintaining stoichiometry of the target composition in the thin films since it is a non-equilibrium process.

In the present effort, thin films of p-type $\text{Bi}_{0.5}\text{Sb}_{1.5}\text{Te}_3$, n-type $\text{Bi}_2\text{Te}_{2.7}\text{Se}_{0.3}$ and n-type $(\text{Bi}_2\text{Te}_3)_{90}(\text{Sb}_2\text{Te}_3)_5(\text{Sb}_2\text{Se}_3)_5$ (with 0.13 wt.% SbI_3) were deposited on substrates of mica and aluminum nitride (on silicon) using Nd-YAG pulsed laser ablation at temperatures ranging from 300⁰C to 500⁰C. The deposited films were characterized using X-ray diffraction and transmission electron microscopy for crystalline quality and epitaxial growth on the substrates. The surface smoothness and microstructure was

verified using scanning electron microscopy. X-ray mapping and energy-dispersive-spectroscopy were performed to determine the composition and homogeneity. The film quality in terms of composition and crystal perfection was studied as a function of growth temperature. The Seebeck coefficient, electrical resistivity and Hall mobility were measured and compared with the measurements on the bulk. Correlation of thermoelectric properties with microstructure of the films has been carried out.

References

1. S.P. Murarka, "Metallization, Theory and Practice for VLSI and ULSI," Butterworth-Hienemann, Boston, pp2-3, 1993.
2. P.H. Chang, R. Hawkins, T.D. Bonifield, and L.A. Melton, Appl. Phy. Lett. Vol.52, No.4, pp.272-274,1988.
3. M. Napolitano Jr., D.D. Andaleon, M.R. Daily, E. Meeks, D. Miller, D.P. Norwood, D.W. Peterson, C.A. Reber, J.E. Robles, and W. Worobey, 2nd International Conference on the application of diamond films and related materials, Editors: M. Yoshikawa, M. Murakawa, pp 275, 1993.
4. F.H. Gaensslen, "MOS Devices and Integrated Circuits at Liquid Nitrogen Temperature," 1980 IEEE ICCD Proceedings, pp. 450-452, 1980.
5. R.K. Kirschmann, "Cold Electronics: An Overview," Cryogenics, Vol.25, pp. 115-122, March 1980.
6. R.C. Jaeger, "Development of Low Temperature CMOS for High Performance Computer Systems," IEEE International Conference on Computer Design: VLSI in computers, pp. 128-130, 1986.

7. Y.Taur and E.J. Nowak, "CMOS Devices Below 0.1 μ m: How High Will Performance Go?", Electronic Devices Meeting Technical Digest, pp.215-218, 1997.
8. J.W. Vandersande and J-P. Fleurial, "Thermal Management of Power Electronics using Thermoelectric Coolers", 15th International Conference on Thermoelectrics, Pasadena, CA, pp. 252-255, 1996.
9. M.M. Sherman and G.O. Campbell in the proceedings of the Spacecraft Thermal Control Symposium, Albuquerque, Nov. 1994.
10. R.C. Chu and R.E. Simons, "Applications of Thermoelectrics to Cooling electronics: Review and Prospects", 18th International Conference on Thermoelectrics, Baltimore, MD, pp. 270-279, 1999.
11. J.W. Vandersande, R. Ewell, J-P. Fleurial and H.B. Lyon, "Thermoelectric Devices and Diamond Films for Temperature Control of High Density Electronic Circuits", 13th International Conference on Thermoelectrics, Kansas City, MO, AIP Conference Proceedings, pp. 174-176, 1994.
12. W.L. Kolander, H.B. Lyon, "Thermoelectric Cooler Utility for Electronic Applications", ASME HTD-Vol.239, National Heat Transfer Conference, Vol.7, 1996.
13. J.G. Stockholm, "Current State of Peltier Cooling", 16th International Conference on Thermoelectrics, Dresden, Germany, pp. 37-46, 1997.
14. J-P. Fleurial, A. Borshchevsky, M.A. Ryan, W. Phillips, E. Kolawa, T. Kacisch and R. Ewell, "Thermoelectric Microcoolers for Thermal Management

- Applications”, 16th International Conference on Thermoelectrics, Dresden, Germany, pp. 641-645, 1997.
15. J. Hansen and M. Nussbaum, “Application of Bismuth-Telluride Thermoelectrics in Driving DNA Amplification and Sequencing Reactions”, 15th International Conference on Thermoelectrics, Pasadena, CA, pp. 256-258, 1996.
 16. M.A. Sanz-Bobi, R. Palacios and A. Arenas, “Thermoelectricity Applied to the Cryoconcentration of Orange Juice”, 15th International Conference on Thermoelectrics, Pasadena, CA, pp. 259-263, 1996.
 17. S. Feher, SAE-931111 (society of Automobile Engineers, New York, NY, 1993).
 18. J. R. Weise and L. Muller, J. Phys. Chem. Solids 15, 13 (1960)
 19. F. Völklein et al.: Thin Solid Films 187, 1990, p253-262.
 20. A. Mzerd et al., “Effect of Substrate Temperature on Crystal Growth of Bi₂Te₃ on single crystal Sb₂Te₃”, J. Mat. Sci. Lett. 13, p301-304, 1994.
 21. M. Stölzer, V. Bechstein and J. Meusal, “Deposition of (Bi,Sb)₂Te₃ Films by Magnetron Co-sputtering from Two Targets – First Results”, 15th International Conference on Thermoelectrics, Pasadena, CA, pp. 422-424, 1996.
 22. A. Dauscher, A. Thomy, and H. Scherrer, “Pulsed laser deposition of Bi₂Te₃ thin films”, Thin Solid Films, Vol. 280, pp. 61- 66, 1996.
 23. D.B. Chrisey and G.K. Hubler, Eds., Pulsed Laser Deposition of Thin Films, Wiley, NewYork, 1994.

Chapter 2

Literature Review

In this section, a brief overview of the fundamental properties and the deposition techniques of Bi_2Te_3 , Sb_2Te_3 , and Sb_2Se_3 based thermoelectrics, aluminum nitride films (used as a buffer layer), and the characterization techniques performed in this research is provided.

2.1 History and Development

The principle of thermoelectricity dates back to the discovery of the Peltier effect. The junction between two dissimilar materials acts as a heat sink or as a heat source, depending on the direction of the electric current. The true nature of Peltier effect was later explained by Lenz as heat absorbed or generated between two conductors with the flow of current and demonstrated this effect by freezing a drop of water at a bismuth-antimony junction and melting the ice by reversing the current. In the beginning of 20th century, the German scientist Altenkirch investigated the physical properties that made it possible to drive heat with electricity¹. The first application of thermoelectric materials was for temperature measurement, as a thermocouple, which was simply a junction of two dissimilar metals. Even though the Peltier effect was discovered in 1834, it has begun to be seriously exploited only in the 1950's. Until then the poor thermoelectric properties of known materials made them inappropriate to fabricate a practical refrigerating device. The utility of thermoelectric materials for cooling is characterized by the thermoelectric figure of merit, Z and is given by:

$$Z = \frac{\alpha^2}{\rho \cdot K}$$

where α is the Seebeck coefficient, ρ is the electrical resistivity, and K is the thermal conductivity. It has also been established that the maximum figure of merit for a material

depends on the mobility μ , the effective mass m^* , of the charge carriers (electrons or holes), and the lattice component of thermal conductivity K_l ^{2,3}. Z can be expressed as:

$$Z \propto \frac{\mu m^{*3/2}}{K_l}$$

A basic cooling sub-assembly consists of a thermocouple made of an n-type material, which has a negative Seebeck coefficient, and a p-type material that has a positive Seebeck coefficient as shown in figure 2.1.1. A thermoelectric module consists of several of these thermocouples connected in series electrically and in parallel thermally. Ever since the mid-1950's, the major material design approach is that introduced by A.V. Ioffe⁴. This was based on selecting semiconducting compounds of heavy elements from the lower right part of the periodic table and then by reducing the lattice thermal conductivity by the formation of mixed crystals. This approach resulted in compounds such as Bi_2Te_3 , and solid solution alloys of Bi_2Te_3 with other compound semiconductors^{4,5} that are now extensively used in thermoelectric modules and are suitable for cooling around 300K.

2.2 Bi_2Te_3 based materials

The Bi_2Te_3 lattice can be represented by a trigonal unit cell that consists of five atoms per cell and possesses the point group symmetry $R3m$ ⁶. The crystal structure of Bi_2Te_3 is shown in figure 2.2.1. In the figure, the tellurium atoms are represented by dark circles where as the bismuth atoms are represented by open circles. The numbers along the edge of the drawing specify the number of atoms present in each layer. Also, the primitive trigonal unit cell is shown in the figure with the aid of dashed lines and consists of two bismuth atoms and three tellurium atoms. In addition, a hexagonal unit cell can also be realized from the figure that consists of 18 bismuth atoms and 27 tellurium atoms

whose c-axis is 30.5 Å and a-axis is 4.38 Å. This corresponds to a c-axis to a-axis ratio of nearly 7 and as a result, the material properties of pure Bi_2Te_3 are a strong function of the crystal orientation with respect to the c-axis.

In order for semiconductor compounds to be good candidates for thermoelectric cooling, they should be close to degeneracy for an optimum figure of merit as shown in figure 2.2.2⁷. Therefore, several experiments were carried out by the addition of many impurities over an extensive range of concentrations⁸. In the case of p-type materials, the problem could be easily solved by the addition of Group IV-V elements such as As, Pb, Sb, Sn and even excess Bi that provided holes of significantly high concentrations. However, for the n-type materials, compound doping was needed since many elements in Groups I, II, III, and VI formed tellurides that were either insoluble or had limited solid solubility in Bi_2Te_3 . Though, initially Cu_2S was used to prepare n-type Bi_2Te_3 , it was not effective in providing an increased carrier concentration in the $\text{Bi}_2\text{Te}_3\text{-Sb}_2\text{Te}_3$ alloys, owing to the preferential formation of Sb_2S_3 that had limited solubility in these alloys⁸. However, Cu_2S could adequately increase the carrier concentration in $\text{Bi}_2\text{Te}_3\text{-Bi}_2\text{Se}_3$ alloys. This was due to the higher free energy of formation of Cu_2S compared to Bi_2S_3 that prevented the formation of the latter compound. Therefore, the need for n-type dopants that have a higher free energy of formation and better chemical stability than the related compound with Bi or Sb arose. This demand could be successfully met by addition of halides of Ag, Bi, Cu, Sb most of which had significantly high solubilities in Bi_2Te_3 , $\text{Bi}_2\text{Te}_3\text{-Bi}_2\text{Se}_3$, and $\text{Bi}_2\text{Te}_3\text{-Sb}_2\text{Te}_3$ systems. However, materials doped with these halides showed a decrease in electrical conductivity with time, though they were initially stable. The halogen atoms of these compounds when added as dopants occupy the

substitutional sites⁹ of the electronegative Te atoms in the case of Bi_2Te_3 and provide free electrons while the metal atoms occupy interstitial positions between two adjacent layers of $\text{Te}(1) - \text{Te}(1)$. In these positions the inter-atomic distance is greatest and therefore, the binding energy is low¹⁰. The metal atoms in these positions are ionized and provide free electrons for conduction, but they diffuse out to the surface combining with oxygen¹¹ or precipitate out as tellurides. This leads to a reduction in the ionized metal ions from the solid solutions, causing a drop in the donor concentration and a subsequent increase in the resistivity. These considerations demand doping materials that possess greater chemical stability at room temperature over prolonged periods of time. SbI_3 is one such compound that has considerable solid solubility in Bi_2Te_3 and its alloys in addition to having adequate resistance to resistivity degradation with time¹².

Meanwhile, theoretical considerations by Ioffe *et al*¹³ suggested that solid solution alloying could improve the figure of merit, Z of semiconductors wherein impurity scattering is predominant, by decreasing the lattice thermal conductivity. At the same time the thermoelectric power and electrical resistivity would remain adversely unaffected. This can be attributed to the fact that alloying introduces short range distortions in the lattice that are effective in the scattering of phonons, but are ineffective in scattering charge carriers that have longer wavelengths. This particular concept pioneered research on the thermoelectric properties of compound semiconductors, especially of the generalized system $(\text{Bi}, \text{Sb})_2(\text{Te}, \text{Se})_3$.

$\text{Bi}_2\text{Te}_3 - \text{Sb}_2\text{Te}_3$ alloys, p-type:

Bismuth telluride, Bi_2Te_3 and Antimony telluride, Sb_2Te_3 possess the same kind of rhombohedral structure and form a continuous series of solid solutions. Undoped

Bi₂Te₃ - Sb₂Te₃ alloys result in a p-type material whose hole concentration increases remarkably with increasing Sb₂Te₃ content. Consequently, figures of merit in excess of $3 \times 10^{-3}/\text{K}$ at room temperature have been reported for p-type alloys in the pseudo-binary system Sb₂Te₃-Bi₂Te₃ with compositions ranging from 20 to 30 mole % Bi₂Te₃ and doped with Se, excess Te, and/or both¹⁴. However, undoped alloys that are rich in Sb₂Te₃ are considered so degenerate that they can not provide high figures of merit. The addition of either Te or Se, being donors is bound to reduce the acceptor concentration by charge compensation and as a result increase the electrical resistivity to an optimum value. However, there is one primary difference between Se and Te doping as pointed out by Rosi et al¹⁵. The addition of Se to Sb₂Te₃-Bi₂Te₃ would result in a preferential formation of selenides that have a higher energy of formation as compared to the tellurides of Bi or Sb. Therefore, alloying with excess Se can result in pseudo-ternary solid solutions of Bi₂Te₃- Sb₂Te₃-Sb₂Se₃ that possess excess Te. The best figure of merit is obtained for a binary alloy having the composition, 75% Sb₂Te₃- 25% Bi₂Te₃ and is about $3.2 \times 10^{-3}/\text{K}$ at a resistivity of about $1.1 \times 10^{-3} \Omega \text{ cm}$ when doped with Se. The same alloy results in a Z-value of $3.1 \times 10^{-3}/\text{K}$ at a resistivity of $8 \times 10^{-4} \Omega \text{ cm}$ when doped with Te. These values symbolize a substantial improvement over the Z- value of $2.2 \times 10^{-3}/\text{K}$ obtained for p-type Bi₂Te₃.

Bi₂Te₃ – Bi₂Se₃ alloys¹²:

Bismuth telluride and bismuth selenide are both isomorphous and there exists a complete solid solubility over the entire range of composition. In the Bi₂Te₃ rich regime, undoped alloys are p-type with the conductivity changing to n-type at about 33% Bi₂Se₃. However, the p-type materials for this particular alloy system resulted in figures of merit

that were much inferior compared to p-type Bi_2Te_3 system. Moreover, for the n-type material, Bi_2Te_3 alloys with 10 to 25 mole % Bi_2Se_3 doped with monovalent metal halides resulted in figures of merit up to $2.8 \times 10^{-3}/\text{K}^{16}$ in the resistivity range of 1 to $1.5 \times 10^{-3} \Omega \text{ cm}$. These values are comparable to those obtained for n-type Bi_2Te_3 and do not show any significant improvement.

$\text{Bi}_2\text{Te}_3 - \text{Sb}_2\text{Te}_3 - \text{Sb}_2\text{Se}_3$ pseudo - ternary alloys^{12,14}:

Bismuth telluride, antimony telluride are both rhombohedral and antimony selenide is orthorhombic in crystal structure. These three compounds form extensive solid solutions over a broad range of compositions except in the regime of large Sb_2Se_3 concentrations¹⁴. These pseudo-ternary solid solutions exhibit p-type conductivity when they are undoped. It was shown that considerable improvement in the figure of merit for p-type alloys could be obtained with slight additions of Sb_2Se_3 in the solid solubility regime, especially for alloys in the Bi_2Te_3 rich region. This could be attributed to the increase in the bandgap of these alloys with addition of Sb_2Se_3 and is considered necessary to combat the deleterious effect of an overlap between the onset of degeneracy and an ambipolar contribution to the thermal conductivity caused by the diffusion of electron-hole pairs¹⁴. For example, the alloy $\text{Bi}_2\text{Te}_3 - 20\% \text{ Sb}_2\text{Te}_3 - 5\% \text{ Sb}_2\text{Se}_3$ alloy results in a figure of merit of $2.8 \times 10^{-3}/\text{K}$ that is a significant improvement over the Z-value of $2.2 \times 10^{-3}/\text{K}$ that was obtained for the $\text{Bi}_2\text{Te}_3 - 20\% \text{ Sb}_2\text{Te}_3$ binary alloy¹². In general, the figure of merit will be lower in materials that have a small bandgap where the ambipolar contribution and the onset of degeneracy overlap. Sb_2Se_3 has a bandgap of about 1.2 eV that is much higher than those of both Sb_2Te_3 and Bi_2Te_3 . The crystal structure and average atomic mass are also much different as shown in Table. 2.2.1. This

may also lead to enhanced scattering of phonons owing to random mass fluctuations and induced lattice strains that in turn can reduce the lattice thermal conductivity. It should be noted that doping in Bi_2Te_3 rich alloys reduces the resistivity whereas doping in Sb_2Te_3 alloys increases the resistivity, though addition of Sb_2Se_3 in both alloys increases the bandgap and improves the figure of merit. In order to obtain n-type materials of these pseudo-ternary solid solutions suitable impurity additions are required. SbI_3 was established to be the most effective impurity addition and contributes about 4.4 electrons/mole. However, the pseudo-ternary alloys that were rich in Bi_2Te_3 gave the best figures of merit for the n-type in spite of Sb_2Te_3 rich compounds having a low lattice component of thermal conductivity. Sb_2Te_3 rich ternary alloys are shown to have n-type conductivity when doped with SbI_3 in excess of the solid solubility limit and hence, suffer from the presence of precipitates and a high degree of polycrystallinity. The best n-type alloy at 300K could be obtained with the composition: $(\text{Bi}_2\text{Te}_3)_{90}(\text{Sb}_2\text{Te}_3)_5(\text{Sb}_2\text{Se}_3)_5$ doped with SbI_3 and resulted in a Z-value of $3.2 \times 10^{-3}/\text{K}$. Though the best p-type alloys could be obtained at Sb_2Te_3 rich compositions, the resistivity values were quite low ($\approx 6 \times 10^{-4} \Omega \text{ cm}$) to obtain an optimum value of Z and needed to be compensated. This resulted in the best p-type alloy compensated with Te having a composition of $(\text{Sb}_2\text{Te}_3)_{72}(\text{Bi}_2\text{Te}_3)_{25}(\text{Sb}_2\text{Se}_3)_3$ that resulted in a Z-value of $3.4 \times 10^{-3}/\text{K}$ at a resistivity of $1.1 \times 10^{-3} \Omega \text{ cm}$. The addition of Te dopants serves to compensate the non-stoichiometric holes to attain the desired conductivity. These values for Z remained the highest obtained for over a long period of time ranging over 25 years. Improvements in the figure of merit for these alloys have recently focussed on additions of multiple dopants, like tellurium, iodine and SbI_3 ^{17,18}. For the p-type material, $(\text{Sb}_2\text{Te}_3)_{72}(\text{Bi}_2\text{Te}_3)_{25}(\text{Sb}_2\text{Se}_3)_3$ a higher figure of merit,

$Z = 3.8 \times 10^{-3}/K$ could be obtained than was possible using Te alone¹⁷. This was attributed to an increased hole mobility that led to an increase in the Fermi energy. Increased Fermi energy results in a higher value for the Seebeck coefficient, thus enhancing the figure of merit. In the case of n-type, improvements were sought by changing composition to a higher level of Sb_2Te_3 . The earlier efforts were hampered by the difficulty to dope such alloys, as the material tends to become more p-type with increase in Sb_2Te_3 ¹⁴. However, addition of multiple dopants in the form of Te and SbI_3 led to improved n-type materials like $(Bi_2Te_3)_{70}(Sb_2Te_3)_{25}(Sb_2Se_3)_5$ that had a higher figure of merit ($Z = 3.4 \times 10^{-3}/K$)¹⁸. This was attributed to a decrease in the thermal conductivity and an increase in the effective mass.

The best known compositions for low temperature applications are $Bi_2Te_{2.7}Se_{0.3}$ for the n-type and $Bi_{0.5}Sb_{1.5}Te_3$ for the p-type respectively^{19,20} as illustrated in figure 2.2.3. $Bi_2Te_{2.7}Se_{0.3}$ with a carrier concentration of $2 \times 10^{18} \text{ cm}^{-3}$ can result in a thermopower, α of about 300 – 310 $\mu V/K$ and a figure of merit, $Z \approx 3.5 \times 10^{-3}/K$. The value of ΔT_{\max} obtained from a thermoelement fabricated from these materials can be as high as 70 K and cooling upto ΔT_{\max} of about 140 K can be reached with the usage of multistage cascade modules. Also, the n-type composition $(Bi_2Te_3)_{90}(Sb_2Te_3)_5(Sb_2Se_3)_5$ (with 0.13 wt.% SbI_3) results in a Z value of $3.5 \times 10^{-3}/K$ while the p-type compound results in a Z value of $2.6 \times 10^{-3}/K$. Deposition of these materials in the form of thin films is bound to have several advantages as outlined in the previous section. In implementing the idea of thermoelectric thin films, we have chosen the method of pulsed laser deposition for the thermoelectrics and dc reactive magnetron sputtering to grow

aluminum nitride as a substrate material. The techniques used for deposition and characterization of these thin films are outlined briefly in the subsequent sections.

2.3 Pulsed Laser Deposition

The use of laser energy in the form of monochromatic and coherent photons has gained wide spread momentum in the processing and characterization of materials. In the world of materials science, lasers have been in constant use over a broad range of applications ranging from process monitoring, localized melting, surface cleaning, to more diverse applications involving laser-induced rapid quenching to improve surface hardness, laser annealing of semiconductors, and pulsed laser deposition (PLD) for growing thin films^{19,20}. PLD is one of the most convenient thin film growth techniques that uses a high intensity pulsed laser beam as an external energy source to ablate a target, form a plume, and deposit thin films onto a substrate. In this case, both the target material and the substrate are housed in a vacuum chamber.

Though several models have been proposed to explain the dynamics of laser-target interaction, none of them are effective in accounting for all of the observations. However, a consensus between these models results in three types of absorptions that ought to be taken into account:

1. Energy absorbed by carriers at the surface of the target.
2. Energy absorbed by lattice phonons and electrons in the lattice of the target.
3. Absorption by the plume.

The mechanism of laser ablation depends on the optical, topological and thermodynamical properties of the target material in addition to the laser characteristics. As an example, metallic surfaces absorb by free carriers, dielectric surfaces absorb by

below bandgap radiation inside the lattice as free carriers are absent and in semiconductors it is a mixed mechanism. However, the ultraviolet radiation of the laser beam is absorbed by most surfaces to a depth of about 1000 Å. At the incidence of laser radiation, electromagnetic energy is initially converted into electronic excitation and then into thermal, chemical and mechanical energy to result in evaporation, ablation, excitation, plasma formation and exfoliation¹⁹. The laser pulses are extremely short in the range of about 20 ns and increase the surface temperature rapidly to a few thousands of degrees Celsius as photons are absorbed on the surface, forming a molten layer also termed the Knudsen layer. However, the rest of the target volume remains virtually at room temperature. This vaporization process takes place in a short duration but with considerable mass transport resulting in a flash of evaporants that are deposited onto the substrate, producing a thin film with a composition identical to that of the target surface. The basic thermal cycle induced by a laser pulse is illustrated in figure 2.3.1²⁷. The evaporants form a plume that consists of a mixture of several energetic species including atoms, molecules, electrons, ions, clusters, micron sized solid particulates and molten globules. The collision mean free path inside the plume is so short that the plume rapidly expands away from the target surface to form a nozzle jet with hydrodynamical flow characteristics. This results in a highly forward-directed velocity distribution and confined plume of materials that condenses on the substrate with very little contamination. Another aspect to be considered is the secondary interaction between the plume and the laser beam. This high-order interaction is bound to increase the plasma temperature and make the evaporants more energetic thus, increasing the adatom surface mobility and resulting in better quality films.

The ability to replicate the exact composition of the target material in the deposited film is one of the incredible benefits of PLD compared to other thin film deposition techniques. This is similar to unconfined plasma in a sputter process. However, PLD does not require a constant glow discharge as compared sputtering in which independent control of process parameters is limited. PLD also scores over thermal evaporation, which produces a vapor composition dependent on the vapor pressures of elements in the target material, while the laser-induced expulsion produces a plume of a material with stoichiometry similar to the target. It is usually easier to obtain the desired film stoichiometry for multi-element materials using PLD than with other deposition technologies. PLD has been applied to the deposition of thin films of many compounds such as oxides, semiconductors, ferroelectrics, and even polymers and ceramics²¹⁻²⁵. The advantages of using pulsed laser deposition can be summed up as follows:

1. The use of an evaporation power source that is independent of vacuum hardware makes the technique extremely flexible and adaptable to different modes of operation even though the laser- target interaction is a complex phenomenon.
2. A dynamic range of deposition pressures can be reached and are considered to be the greatest compared to other deposition processes.
3. PLD has the ability to reproduce the target composition with relative ease even in the case of complex materials.
4. At wavelengths of 250 nm and below, most of the materials absorb laser energy via linear or non-linear processes, and hence, coupling of energy is possible to most surfaces²⁶.

5. PLD has the ability to fabricate films in high partial pressures of reactive gas, such as oxygen. In the deposition of many oxide films, it is critical to maintain the proper oxygen content in the chamber. The presence of reactive gas can help bind volatile species to a substrate and aid in preserving the film stoichiometry.
6. Well-oriented and crystalline films can be obtained using PLD owing to the high surface adatom mobility while working at room temperature.
7. Other advantages of PLD result from its minimal vacuum requirements, lack of a stringent need for specialized targets, and ability to deposit films of many different materials in situ for multilayer structures. Smaller targets can be used for deposition, making the process more economical.

The main limitation of PLD results from the presence of molten droplets, micron-sized particulates caused by splashing and the narrow forward angular distribution that make large area scale-up problematic. Also, PLD is relatively a new process and many issues related to industrial scale-up such as deposition of films on large-area substrates are yet to be addressed. Although scale-up problems can be solved in part, by rastering the laser or the substrate, splashing is an intrinsic problem that is more difficult to deal with. In the case of thin films for optoelectronic and device applications, particulates can induce defects and scattering centers that lower carrier mobility, shorten minority lifetime and reduce the damage threshold of optical films. Splashing is a common phenomenon that occurs in many materials with the exceptions of a few material systems that have high vapor pressure (much below the melting temperature), high thermal conductivity and targets that are dense and single-crystalline¹⁹. Any one or a combination of the following mechanisms can cause splashing: subsurface boiling, shock-wave recoil and

exfoliation. The various mechanisms responsible for splashing are illustrated in figure 2.3.2.

Subsurface boiling:

This mechanism can occur when the laser beam superheats the subsurface layer before the surface reaches its evaporation point. It leads to the surface breaking apart into large micron-sized globular particles when the subsurface expands. This usually happens when the laser energy is transferred into thermal energy much faster than the time taken for the surface layers (skin-depth) to evaporate. Though all materials are susceptible to subsurface boiling, it is more pronounced in systems that have low melting and boiling points.

Shock wave recoil:

The rapid expansion of plume causes a shock wave, which in turn exerts a sudden drop in pressure just above surface. These shock waves pull out droplets of liquid from the target surface and are carried over to the substrate where they get condensed.

Exfoliation:

In the first place, irregularities on the surface of the target are created by repetitive laser ablation, which leads to the formation of slender and needle shaped microdendritic structures. The thermal shock induced by the laser beam later on causes these fragile irregularities on the surface to break off. The chunks of loose particles thus, created are carried towards to the substrate by the rapidly expanding plume and condense onto the deposited film. The resulting particulates are randomly shaped depending on the parent structure from which they were created and the location of the thermal stress.

Several techniques have been established for reducing splashing and can be listed as follows:

1. A decrease in the incident laser power density can reduce splashing. However, it results in a decreased deposition rate as well.
2. A mechanical particle filter that rotates at a high speed can be used to prevent slow moving particles from getting deposited.
3. The trajectory of the plume can be manipulated by using two synchronized laser beams while the trajectory of the heavier particulates remains relatively unaffected. The substrate is suitably positioned so that the particulates can be avoided²⁸.
4. The use of highly dense and smooth target surfaces is effective in reducing splashing. In some cases molten targets have proved to reduce splashing occurring due to exfoliation²⁹.
5. Particulates can also be avoided by off-axis PLD in which the substrate faces away from the target³⁰. But, this technique can be only limited to reactive PLD where background pressure of the gases can provide sufficient scattering and diffusion.

2.4 Deposition of Bi₂Te₃ based thermoelectric thin films

Thin films of Bi₂Te₃ based materials have been deposited using various techniques like co-evaporation of different elements³¹, flash evaporation³², sputter deposition³³, chemical vapor deposition³⁴, molecular beam epitaxy³⁵, electro-deposition³⁶, and hot wall epitaxy³⁷. However, pulsed laser deposition has not been tried extensively. All the previous studies have reported the primary difficulty in maintaining stoichiometry that could be achieved only in a small range of substrate temperatures ranging from 250 to 300°C. Moreover, techniques like flash evaporation are difficult to control while hot

wall epitaxy demands very high substrate temperatures, ruling out the use of many substrates. Sputter deposition suffers from the problem of resputtering during the film growth while vacuum evaporation suffers from differences in volatility of component elements. The most important requirement for attaining high values for the figure of merit is the stoichiometric composition within the solubility limits of the phase diagram. The exasperating problem of strong deviation from stoichiometry results from the fact that the different elements have dissimilar sticking coefficients and the tendency for re-evaporation from the deposited films. Also, the growth structure is very important since grain boundaries and crystalline defects increase the resistivity by scattering charge carriers. In the present effort, we have used pulsed laser deposition²³ to deposit thin films from targets of p-type $\text{Bi}_{0.5}\text{Sb}_{1.5}\text{Te}_3$, n-type $\text{Bi}_2\text{Te}_{2.7}\text{Se}_{0.3}$ and n-type $(\text{Bi}_2\text{Te}_3)_{90}(\text{Sb}_2\text{Te}_3)_5(\text{Sb}_2\text{Se}_3)_5$ (with 0.13 wt.% SbI_3). The p-type and n-type materials under consideration are known to be the best known compositions for fabricating thermoelectric cooling devices for use at room temperature. Pulsed laser deposition has the advantage of achieving congruent transfer of the target composition to the deposited thin films. Moreover, PLD being a non-equilibrium process is expected to achieve good quality thermoelectric thin films. It has been shown that highly crystalline and stoichiometric Bi_2Te_3 films have been deposited on glass substrates under convenient experimental conditions of substrate and target configurations³⁸. The films were shown to have a similar orientation compared to the bulk, but exhibited a preferential direction during the early stages of growth. In the present study, attention has been focussed on the deposition of stoichiometric thermoelectric thin films by PLD by varying deposition conditions in relation to laser energy, target composition and substrate characteristics.

The films were deposited on substrates of mica and aluminum nitride (deposited on silicon) using Nd-YAG pulsed laser ablation at temperatures ranging from 300⁰C to 500⁰C.

2.5 Growth of aluminum nitride

Aluminum nitride is an essential component in integrated electronic circuits because of its superior dielectric properties coupled with a fairly high value of thermal conductivity. Other lucrative properties of AlN include high surface acoustic velocity, excellent elevated temperature stability, high value of dielectric constant, and a good hardness value³⁹. The fundamental properties of AlN are listed in Table 2.5.1⁴⁰ while the crystal structure of AlN is illustrated in figure 2.5.1⁴¹. AlN takes a hexagonal close packed (HCP) structure that can be visualized as a top and bottom plane containing 7 atoms of aluminum forming a regular hexagon around a central atom. The nitrogen atoms are present in between these planes in the form of a half-hexagon that consists of 3 atoms. The stacking sequence of Al, and N atoms are in the form of ABABAB... AlN with its excellent thermal conductivity and high dielectric constant is extensively used as a heat sink in electronic packaging. However, diamond is the best heat sink material due to its unmatched high thermal conductivity and its thermal expansion almost 2-3 times lower than that of AlN. In spite of these advantages, practical applications of diamond as a substrate in electronic circuits are limited by requirements of moderate thickness, homogeneity, and large area that are difficult to produce economically⁴². Although the low-pressure synthesis of diamond is economical, use of diamond films alone is not adequate as a heat dissipater. This is related to the low heat capacity of diamond that is about 6.19 Joules/moles-⁰C. Aluminum nitride serves to counter the effect of reduced

thermal conductivity in diamond attributed to the presence of voids and discontinuities. Moreover, it can also improve the adhesion of the first layer of discontinuous diamond to the subsequent deposited layers⁴³ which can be very critical when integrated with thin film thermoelectric devices (figure 1.1). Aluminum nitride can also serve as a buffer layer for diamond growth on silicon and at the same time act as a diffusion barrier for carbonaceous products into silicon from the gaseous atmosphere. Aluminum nitride has also shown to enhance the nucleation of diamond in HFCVD⁴⁴ based on the conclusion that the AlN surface undergoes some kind of chemical reaction with the CVD gases to provide sites for heterogeneous nucleation.

High quality aluminum nitride films can be grown on silicon (111) substrates by RF magnetron sputtering at elevated temperatures ranging from 700°C to 1000°C. These films are shown to be highly oriented possessing the basal plane (002) orientation. The growth of high quality crystalline aluminum nitride is often impaired by the presence of residual oxygen contamination that is quite difficult to avoid. High quality AlN can be grown in ultra-high vacuum conditions resulting from very little oxygen contamination⁴⁵. Chein-chuan et al⁴⁶ have dealt with the effect of temperature, sputtering power, pressure and the percentage of N₂ on the growth of aluminum nitride. Highly c-axis oriented AlN thin films on Si (100) substrates could be grown by rf magnetron sputtering at a pressure of 7.5 mtorr, rf power of 300W, and a substrate temperature of 350°C. The average grain size of these films was reported to be 100nm. It has been established that, increased concentration of nitrogen in the sputtering gas results in enhanced growth of the films along the (002) direction. Lowered pressures of nitrogen not only decreased the crystalline quality of the films but also resulted in different growth orientations like (100)

and (101). AlN films with a strong (002) orientation could also be produced with the introduction of hydrogen in the range of 0-20% while the nitrogen concentration was kept constant at 25%⁴⁷. Epitaxial growth of aluminum nitride on Si(111) substrates by dc reactive magnetron sputtering in the range of 500-800°C has also been reported⁴⁸ which indicates that temperature plays a crucial role in the deposition of high quality aluminum nitride. The orientation of the deposited films changed from being highly textured at 500°C to single crystalline, beyond 600°C as observed by transmission electron microscopy. These films were shown to follow the epitaxial relationship AlN [0001]/Si[111]. Partially ionized beam deposition (PIB) can also be used for depositing aluminum nitride by use of aluminum as an evaporant in a nitrogen ambient at a temperature of 500-600°C⁴⁹. This is somewhat different to sputtering that uses Ar⁺ ions to bombard the surface, as the PIB technique utilizes self-ions (the ions of the deposited material) to assist in the film growth. In this method the evaporated species and the reactive gas are partially ionized by electron bombardment of the ionization zone. The dissociated and activated aluminum and nitrogen containing species get accelerated towards the substrate in the acceleration field. AlN can also be deposited using chemical vapor deposition and is usually performed at elevated temperatures in the range of about 800 to 1100°C^{50,51}. Chemical vapor deposition, CVD results in high purity AlN films with trace amounts of oxygen. In addition smoother films can be obtained in the case of MOCVD because of in-situ etching of the substrate by precursors which are AlCl₃ or Al(CH₃)₃, N₂, and NH₃. Layer by layer growth of AlN was performed by molecular beam epitaxy⁵², and by plasma assisted gas source epitaxy⁵³. Pulsed laser deposition using a KrF laser source ($\lambda = 248\text{nm}$) has also been demonstrated to deposit AlN thin films^{39,54}.

In this case, a compound AlN target was ablated in an ultra-high vacuum environment with the substrate temperature maintained at 600°C. The basal plane (002) growth orientation of AlN was observed in all these cases.

Deposition of aluminum nitride by DC reactive magnetron sputtering⁵⁵:

Aluminum nitride thin films were deposited by means of pulsed DC reactive magnetron sputtering (RMS). An inert gas is fed into the sputter deposition chamber at low pressure while a DC voltage is applied across two electrodes using a pulsed DC power source to create a plasma. The plasma is a conducting medium that consists of a mixture of neutral argon atoms, positive ions, and free electrons. The target material to be deposited is negatively biased by applying a negative DC voltage while the substrate and the chamber walls act as the anode. As the plasma is created, the positive ions in the plasma get accelerated towards the negatively biased target. These energetic ions strike the target surface and sputter away the target atoms. The sputtered atoms ionize, travel through the plasma and strike the surface of the substrate and the chamber walls where they condense and form the deposited film. In order to increase the efficiency of the ionization resulting from the collisions between the electrons and gas atoms, magnets placed behind the target are employed in magnetron sputtering. The magnetic field perpendicular to the electric field traps electrons near the target surface, and sends them spiraling away in a helical path until they collide with argon atoms. The ionization and sputtering efficiencies are improved and good deposition rates can be achieved in reactive magnetron sputtering (RMS). An electron trap is formed over the surface in the case of pulsed DC magnetron sputtering and intense plasma is generated³⁹. This results in enhanced deposition rates, which is the advantage of using pulsed DC RMS. However,

the surface of the chamber also gets coated with the insulating AlN film calling for periodic cleaning of the chamber. In RMS, the recorded effective and collective powers are used as an indication of the metallic nature of the films. The effective power accounts for the ions in the plasma while the circulating power is the power applied to generate the plasma. A higher effective power than the circulating power implies metallic nature of the deposited film while a higher circulating power implies insulating nature of the films³⁹.

In implementing the idea of growing thermoelectric thin films on highly conductive substrates we chose mica and aluminum nitride as the substrate materials. Both mica and aluminum nitride are excellent thermal conductors and at the same time possess a hexagonal crystal structure that is well suited for the growth of Bi₂Te₃ based materials that prefer the 00n orientation of growth. Since, aluminum nitride substrates are not readily available, we used dc reactive magnetron sputtering for depositing AlN on silicon (100) and (111) substrates. The substrates with aluminum nitride buffer layers were later used to deposit thermoelectric thin films by PLD. All the depositions were followed by characterization of the films. The techniques used for characterization are discussed briefly in the following sections while the experimental details are described in the next chapter.

2.6 Characterization Techniques

2.6.1. X-ray Diffraction:

The atomic planes of a crystal reflect incident x-ray beams that interfere with one another as they leave the crystal, provided the wavelength is closer to the magnitude of the inter-atomic spacing. This phenomenon is called x-ray diffraction. Diffraction arises

from the constructive or destructive interference between two or more waves and can be observed whenever Bragg's law is satisfied. Bragg's law refers to the simple equation: $n\lambda = 2d \sin\theta$, where θ is the angle of incidence, d the distance between atomic layers in a crystal, λ the wavelength of the incident x-ray beam and n an integer. Bragg's law can also be used to explain the interference pattern of ions, electrons, neutrons, and protons that have a wavelength similar to the distance between the atomic or molecular structures of interest. As a x-ray beam traverses through a material, its intensity decreases with the distance traveled and a x-ray diffractometer is used to measure the intensities of reflected beams from small areas. These results provide direct evidence of atomic-level spacing within the crystal lattice of the specimen. It also yields details of the crystal structure for the different phases present in the specimen. Moreover, finer details of the crystal structure, such as the state of atomic order, also can be derived. However, an arbitrary setting of a single crystal in a x-ray beam may not produce any diffracted beams. In order to obtain adequate information in a single crystal diffraction pattern using monochromatic radiation, θ is continuously varied over a range of values, to satisfy Bragg's law.

2.6.2 Scanning Electron Microscopy:

In a scanning electron microscope a beam of electrons is generated from an electron gun that is attracted through the anode, condensed, and focused as a very fine point on the sample by the objective lens. There are scan coils in the microscope that energize the beam by varying the voltage to create a magnetic field, that in turn deflects the beam back and forth in a controlled pattern. The electron beam strikes the sample and produces a wide range of signals that include: x-rays, backscattered electrons, secondary

electrons, photons, auger electrons, etc. The most commonly used signals in a SEM are the secondary electrons, the backscattered electrons and the x-rays. The secondary electrons yield topographical information where as the backscattered electrons yield information about the atomic number of the scattering species in addition to topography. The x-rays are also analyzed to give information about the composition.

Secondary electrons are generated from the specimen and gain energy by inelastic collisions with the beam electrons. Their energy is less than 50eV and are predominantly produced by the interactions between energetic beam electrons and weakly bonded conduction-band electrons in metals or the valence electrons in insulators and semiconductors. The backscattered electrons are obtained from elastic scattering that results in little ($<1\text{eV}$) or no change in energy of the scattered electron, although there is a change in momentum. As the mass remains constant, the direction of the velocity changes. The angle of scattering ranges between $0\text{-}180^\circ$, with a typical value being about 5° . Elastic scattering occurs between the negatively charged electrons and the positive nucleus.

During inelastic scattering, energy is transferred to the electrons surrounding the atoms. A single inelastic event can transfer a large amount of energy from the beam ranging from a fraction to many keV. The main processes include phonon excitation, plasmon excitation, secondary electron excitation, continuum X-ray generation, and ionization of inner shells. An electron detector is used in conjunction with the SEM to convert the radiation of interest into an electrical signal for manipulation and display by signal processing electronics. Most modern SEMs are equipped with an Everhart-Thornley (E-T) detector that consists of scintillator material that is struck by energetic

electrons. The collisions result in photons that are conducted by total internal reflection in a light guide to a photomultiplier tube. These photons are then converted back into an electron current where a positive bias attracts the electrons and collects them so that detection is possible. In a typical SEM, spatial resolution is as high as 1 nm for some instruments and magnification factors as high as 200,000X can be achieved.

2.6.3 Energy Dispersive Spectroscopy, X-ray mapping and Quantitative analysis:

As the electron beam of the SEM is scanned across the surface of the specimen, collisions with the atoms along its path produce x-ray fluorescence. The energy of each x-ray photon generated is characteristic of the element from which it is generated, as discussed in the previous section. These x-rays can be detected with the aid of an energy dispersive spectrometer that is essentially a solid state device capable of discriminating between x-ray energies. Typically, the lateral resolution and sampling depth are on the order of 1.0 μm . Energy dispersive spectroscopy (EDS) microanalysis systems are available that collect the x-rays, sort and plot them according to energy, and even automatically identify and label the elements responsible for the peaks in this energy distribution. The EDS data are usually compared with either known or computer-generated standards to produce a full quantitative analysis showing the sample composition. The K-ratio is one such simple method and can be taken as a first estimate of the elemental concentration within the specimen. The concentration of C_x of an element in a sample relative to the concentration C_s of the same element in a standard material of known composition can be expressed as: $C_x = (I_x/I_{sx}) \times C_s$ where I_x and I_{sx} are the intensities of X from the specimen and the standard respectively, without assuming any matrix effects. The standard is usually a pure element (100%) or a lower

concentration in a homogeneous compound. The ratio of the intensity of the unknown to the intensity of the standard is referred to as the K-ratio, K_x and is given by $C_x = K_x \times C_s$ where: $K_x = I_x/I_{sx}$. This method of analysis is accurate only when the sample and all the standards are closely similar in composition. The data output resulting from EDS can be either in the form of element analysis or the original spectrum depicting the number of x-rays collected at each energy or maps of distributions of elements over areas of interest.

2.6.4 Transmission Electron microscopy:

The principle of electron microscopy is based on the fact that electron wavelengths in the order of atomic dimensions can be used to observe microscopic features with a very high resolution. The image resolution of TEM can be related to the Rayleigh criterion for light microscopy. It states that the smallest distance that can be resolved, δ , is given approximately by the equation $\delta = 0.61\lambda/\mu \sin\beta$, where λ is the wavelength of the radiation, μ the refractive index of the medium, and β is the semi-angle of collection of the magnifying lens. From DeBroglie's equation, $\lambda \sim 1.22/E^{1/2}$, where E is the energy of the electrons in electron volts, and λ the wavelength in nm. Hence, we can obtain electrons with very small wavelengths by increasing the energy. Electrons produce ionizing radiation and possess the distinct advantage of producing a wide range of secondary signals upon interacting with the specimen. The transmitted electrons that are elastically and inelastically scattered are used in transmission electron microscopy to extract information about the atomic arrangement and composition. The momentum imparted to the electrons by accelerating them through a potential drop is responsible for providing the sufficient energy to penetrate the surface layers of the sample. Electrons may be generated from either a field emission or a thermionic emission source. The

accelerated electrons are used in conjunction with electron-optics consisting of electromagnetic lens; condenser, objective, and intermediate lenses. Electrons undergo coherent scattering and diffraction from lattice planes in crystalline materials yielding phase identification. The use of small electron wavelengths enables flat Ewald sphere construction in the reciprocal lattice. Imaging using diffraction or strain contrast in analytical mode and phase contrast in high resolution is performed onto a fluorescent screen.

2.6.5 Electron Energy Loss Spectroscopy:

EELS is a technique frequently used in conjunction with transmission electron microscopy (TEM) or scanning TEM (STEM) and involves the impingement of a sample with a monoenergetic beam of electrons. The electrons bombarding on the sample lose energy by a variety of mechanisms and can be used to reveal the composition of the sample in a TEM. Plasmon losses are one such frequent mechanism of energy loss. Plasmons are collective excitations of the electron gas in the material and are usually several eV in magnitude. In the TEM, the losses predominantly occur in the bulk of the sample, as the beam travels through the thin specimen to the EELS detector. This results in a sharp peak that corresponds to elastically scattered electrons with a number of peaks at lower energy that correspond to plasmon or other excitations. By examining energy losses due to plasmons at high resolution, data concerning the composition and nature of elements present in the sample can be determined.

2.6.6 Determination of thermopower:

Thermopower or Seebeck coefficient is defined as the derivative (rate of change) of thermal EMF with respect to temperature normally expressed as microvolts per degree.

In order to facilitate measurement of Seebeck coefficient, a steady thermal gradient should be established across the sample that can be controlled and monitored easily. The sample is mounted on a glass plate that has a chip heater mounted on its end along with a few thermocouple leads to record temperature and voltage generated across the sample. The chip heater is responsible for generating a thermal gradient across the glass plate. The sample chamber consists of three concentric cylindrical shells to thermally isolate the sample from the ambient. The arrangement also includes a power supply of a few μA of current that switches on and off once every minute. This current causes a potential drop in the specimen and another thermocouple is used to measure this ΔV . Also, the resistivity is measured from the geometry of the sample using the same potential difference. A schematic of the specimen support plate is shown in figure 2.6.6.1.

2.6.7 Hall mobility:

In order to determine both the mobility μ and the carrier concentration n_s , a combination of resistivity measurement and Hall measurement can be used. The Van der Pauw technique is widely used to determine the resistivity of uniform samples. As originally devised by Van der Pauw, an arbitrarily shaped thin-plate sample containing four very small ohmic contacts placed on the periphery are used. Van der Pauw demonstrated that there are actually two characteristic resistances R_A and R_B , that account for sheet resistance R_S through the van der Pauw equation $\exp(-\pi R_A/R_S) + \exp(-\pi R_B/R_S) = 1$ which can be solved numerically. The electrical resistivity, ρ can be calculated using $\rho = R_S d$. To obtain the two characteristic resistances, one applies a dc current I into contact 1 and out of contact 2 and measures the voltage V_{43} from contact 4 to 3 as shown in figure 2.6.7.1. Then current I is applied into contact 2 and out of contact 3 while

measuring the voltage V_{14} from contact 1 to contact 4. R_A and R_B are calculated by means of the following expressions: $R_A = V_{43}/I_{12}$ and $R_B = V_{14}/I_{23}$. The Hall measurement is used in conjunction to determine the sheet carrier density n_s by measuring the Hall voltage V_H . The Hall voltage measurement consists of a series of voltage measurements with a constant current I and a constant magnetic field B applied perpendicular to the plane of the sample. The same set-up can be used for the Hall measurement. To measure the Hall voltage V_H , a current I is forced through the opposing pair of contacts 1 and 3 and the Hall voltage $V_H (= V_{24})$ is measured across the remaining pair of contacts 2 and 4. Once the Hall voltage V_H is acquired, the sheet carrier density n_s can be calculated via $n_s = IB/q|V_H|$ from the known values of I , B , and q . Also, the hall mobility can be determined using the equation, $1/\rho = \mu.n_s.q$.

References

1. D.M. Rowe, "CRC Handbook of Thermoelectrics", CRC Press: Boca Raton, FL, 1995.
2. A.F. Ioffe, Semiconductor Thermoelements and Thermoelectric Cooling, Info-search, London, 1957.
3. H.J. Goldsmid and R.W. Douglas, Brit. J. Appl. Phys. Vol. 5, pp. 386, 1954.
4. A.V. Ioffe and A.F. Ioffe, Sov. Phys. Solid State, Vol. 2, p.719, 1956.
5. F.D. Rosi, B. Abeles, and R.V. Jensen, "Materials for Thermoelectric Refrigeration", J. Phys. Chem. Solids Vol. 10, pp. 191, 1959.
6. L.P. Caywood and G. Miller, Phys. Rev. B, Vol. 2, pp. 3210, 1970.
7. D.M. Rowe, MTS Journal, Vol. 27 (3), pp. 43-48, 1997.

8. F.D. Rosi and E.G. Ramberg, "Evaluation and Properties of Materials for Thermoelectric Applications", pp. 136- 137 in Thermoelectricity, ed. by P.H. Egli, John Wiley & Sons, New York and London, 1960.
9. H.J. Goldsmid, Proceedings of the International Conference on Semiconductors, Prague, 1960, Czechoslovak Academy of Sciences, 1961.
10. J.R. Drabble and C.H.L. Goodman, J. Phys. Chem. Solids, Vol. 5, pp. 142, 1958.
11. R.O. Carlson, J. Phys. Chem. Solids, Vol.13, pp. 65, 1960.
12. W.M. Yim and F.D. Rosi, Solid State Electronics, Vol. 15, pp. 1121-1140, 1972.
13. A.F. Ioffe, S.V. Airapetiants, A.V. Ioffe, N.V. Kolomoets, and L.S. Stil'bans, Dokl. Akad. Nauk. SSSR, Vol. 106, pp. 981, 1956.
14. W.M. Yim, E.V. Fitzke, and F.D. Rosi, J. Mat. Sci., Vol.1, pp. 52, 1966.
15. F.D. Rosi, E.F. Hockings, and N.E. Lindenblad, RCA Rev.. Vol.22, pp. 82, 1961.
16. F.D. Rosi, B. Ableles, and R.V. Jensen, J. Phys. Chem. Solids Vol. 10, pp. 191, 1959.
17. P.J. Taylor, J.R. Maddux, W.A. Jesser, and F.D. Rosi, J. Appl. Phys., Vol. 85, No.11, 1999.
18. M.H. Ettenberg, W.A. Jesser, and F.D. Rosi, Proceedings of the 15th IEEE-International Conference on Thermoelectrics, Pasadena, CA, 1996, pp.52.
19. D.B. Chrisey and G.K. Hubler, (eds.), Pulsed Laser Deposition of Thin Films, Wiley, New York, 1994, pp. 1- 15.
20. J.T. Cheung and H. Sankur, CRC Crit. Rev. Solid State Mater. Sci. Vol. 15, pp.63-109, 1988.
21. J.W. Horwitz and J.A. Sprague, in D.B. Chrisey and G.K. Hubler, (eds.), Pulsed Laser Deposition of Thin Films, Wiley, New York, 1994, pp. 229.

22. R. E. Muenchausen and X. D. Wu, in D.B. Chrisey and G.K. Hubler, (eds.), Pulsed Laser Deposition of Thin Films, Wiley, New York, 1994, pp. 357.
23. D. K. Fork in D.B. Chrisey and G.K. Hubler, (eds.), Pulsed Laser Deposition of Thin Films, Wiley, New York, 1994, pp. 393.
24. R.E. Leuchtner and K.S. Grabowski, in D.B. Chrisey and G.K. Hubler, (eds.), Pulsed Laser Deposition of Thin Films, Wiley, New York, 1994, pp. 473.
25. S.B. Ogale in D.B. Chrisey and G.K. Hubler, (eds.), Pulsed Laser Deposition of Thin Films, Wiley, New York, 1994, pp. 567.
26. T. Venkatesan in D.B. Chrisey and G.K. Hubler, (eds.), Pulsed Laser Deposition of Thin Films, Wiley, New York, 1994, pp. 313.
27. S.R. Foltyn in D.B. Chrisey and G.K. Hubler, (eds.), Pulsed Laser Deposition of Thin Films, Wiley, New York, 1994, pp. 91.
28. S.V. Gapanov, A.A. Gudkov, and A.A. Fraerman, Sov. Tech. Phys. Lett. Vol. 27, pp.9, 1982.
29. H. Sankur, W.J. Gunning, J. DeNatale, and J. Flintoff, Appl. Phys. Lett. Vol. 65, pp. 2475-2477, 1989.
30. R.J. Kennedy, Thin Solid Films, Vol. 214, pp. 223, 1992.
31. J. George and B. Pradeep, Solid State Commun., Vol. 56, pp. 117, 1985.
32. F. Völklein et al.: Thin Solid Films 187, 1990, p253-262.
33. M. Stölzer, V. Bechstein and J. Meusal, 15th International Conference on Thermoelectrics, Pasadena, CA, pp. 422-424, 1996.
34. R. Venkatasubramanian, M.L. Timmons and J.A. Hutchby, in K. Matsuura (eds.), Proc. 12th Int. Conf. on Thermoelectrics, IEE of Japan, Tokyo, pp. 322, 1994.

35. A. Mzerd et al., J. Mat. Sci. Lett. 13, p301-304, 1994.
36. P. Magri, C. Boulanger, and J.M. Lecurie, in B. Mathiprakasam (eds.), Proc. 12th Int. Conf. on Thermoelectrics, AIP Press, New York, pp. 277, 1995.
37. M. Stölzer, M. Stordeur, and I. Stark, 15th International Conference on Thermoelectrics, Pasadena, CA, pp. 445-449, 1996.
38. A. Dauscher, A. Thomy, and H. Scherrer, Vol. 280, pp. 61- 66, 1996.
39. K. Jagannadham, A.K. Sharma, Q. Wei, R. Kalyanaraman, and J. Narayan, Journal of vacuum science and technology, A 16 (5), Sep/Oct 1998.
40. Website: http://www accuratus.com/Aluminum_Nitride.htm
41. Website: www.jwave.vt.edu/crcd/farkas/lectures/structure/fig3.gif
42. J.B. Cui, Y.R. Ma, J.F. Zhang, H. Chen, R.C. Fang, (submitted paper).
43. K. Jagannadham, Journal of vacuum science and technology A, 17(2), Mar/Apr 1999.
44. V.P. Godbole, J. Narayan, Journal of Materials Research, Vol 11, N0.7, Jul 1996, pp 1810-1818.
45. F. Malengru and M. Veremeersch, Journal of material research, vol 12 No.1, Jan 1997, pp 175-188.
46. C. Chuan, Y.C. Chen, H.J. Wang, W.R. Chen, Journal of vacuum science and technology A, 14 (4), Jul/Aug(1996), pp 2238-2243.
47. H.C. Lee, K.Y. Lee, Y.J. Yong, J.Y. Lee, G.H. Kim, Thin solid films 271, pp 50-55, 1998.
48. W.J. Meng, J. Heremans, and Y.T . Cheng, Applied physics letters. Vol 59(17), October 1991, pp 2097-2099.

49. J. Xie, Q. Mo, and J. Feng, Nuclear instruments and methods in Physics Research B, vol 124, pp519-522, 1997.
50. C. Li, L. Hu, W. Yuan, and M. Chen, Materials chemistry and physics 47, pp273-278, (1997).
51. R.C. Buggeln, M. Meyyappan, and S.J, Shamroth, Journal of vacuum science and technology A, 14(4), Jul/Aug 1996.
52. B. Daundin and F. Widmann, Journal of crystal growth 182, pp1-5, 1997.
53. A. Bourret, A. Barski, J.L. Rouviere, G. Renaud, and A. Barbier, Journal of applied physics, vol 83, No. 4.
54. T. Ogawa.M. Okamoto, H. Yagi, Y. Mori, A. Hatta, T. Ito, T. Sasaki, A Hiraki, Diamond films and technology, Vol 6, No.2, pp 87-94 .
55. J.D. Plummer, M.D. Deal, and P.B. Griffin, Silicon VLSI Technology (Prentice Hall, New Jersy) pp539-551.
56. EDAX Corporation, USA, New Doornfontein

Chapter 3

Experimental Details

3.1 Growth

This chapter gives the experimental details of the preparation of the targets, substrates, deposition conditions, and characterization of the thin films. The different characterization techniques and the various samples that have been prepared during the development of thermoelectric thin films and their utility have been listed in Table 3.1.

3.1 Substrate surface cleaning and preparation

The surface of the substrate should be atomically clean and free from impurities because the contaminants can interact with the thin films being deposited and substantially degrade its quality and adhesion to the substrate. The presence of unwanted surface contaminants can also influence the growth and orientation of the films in an undesired manner. Most frequently, the presence of a thin layer of an amorphous oxide on the substrate surface can induce polycrystalline film growth during deposition that is considered detrimental. In our experiments, a thin mica sheet with an average thickness of 15 μm and p-type silicon wafers [both (100) and (111)] with an average thickness of 525 μm were chosen as the substrate materials. The preparation of these substrate surfaces included numerous steps. Initially, the substrates were cleaned with acetone to dissolve any contaminants adhering to the surface such as grease, oils, etc. This was followed by rinsing with methanol to remove any residues left behind after cleaning with acetone. Furthermore, the substrates were rinsed in distilled water and dried. In addition, the silicon wafers were etched in a 49% hydrofluoric acid solution for about 3 minutes, followed by rinsing in distilled water and drying. This procedure is used only for the silicon wafers as it is designed to etch away the native oxide present on the surface. The mica substrates were then used for the deposition of thermoelectric thin films while on

the silicon substrates; aluminum nitride was sputter deposited, prior to the deposition of thermoelectric thin films using PLD.

3.2 Deposition of aluminum nitride

Aluminum nitride was deposited on silicon substrates by employing the technique of dc reactive magnetron sputtering that uses a mixture of ultrahigh purity argon and nitrogen gases. In our experiments, the partial pressures of argon and nitrogen were both maintained between 0-1 mTorr that resulted in a total pressure of 1-2 mTorr in the deposition chamber. A high purity aluminum (99.999%+) disc 4 inches in diameter and powered by a pulsed DC source was used as the target material. After the substrates were cleaned, they were loaded into the stainless steel deposition chamber that was then evacuated to a pre-deposition vacuum of 5×10^{-6} Torr using a turbo-molecular pump. The substrate temperature was slowly raised to 600 °C by means of a resistance heater powered by an externally controlled variac and the temperature was monitored by a thermocouple placed on the ceramic substrate holder. Initially, an argon atmosphere was established at a partial pressure of 0-1 mTorr in the chamber and plasma generated at a target current of 0.5 amperes. This stage is intended to cleanse the target and a movable shutter was used to mask the substrates. The duration of target cleaning lasted about two minutes. Soon after, the target current was increased to 2 A, while ultra pure nitrogen gas at a partial pressure of 0-1 mTorr was introduced into the chamber. At this juncture, the ratio of circulating to effective power was noted to be in the range of 0.62 to 1.05. The significance of effective and collective powers has been described earlier in the section 2.5. These ratios are indicative of the insulating nature of the film being deposited. This observation is in tune with the expectations since aluminum nitride is a highly insulating

material. The deposition time for different experiments was varied between 30 to 90 minutes depending on the thickness desired.

3.3 PLD of thermoelectric thin films

The $\text{Bi}_{0.5}\text{Sb}_{1.5}\text{Te}_3$ ingots used as targets were made by powder sintering where as the $\text{Bi}_2\text{Te}_{2.7}\text{Se}_{0.3}$ and $(\text{Bi}_2\text{Te}_3)_{90}(\text{Sb}_2\text{Te}_3)_5(\text{Sb}_2\text{Se}_3)_5$ (with 0.13 wt.% SbI_3) ingots were grown by the Bridgman method. A stoichiometric mixture of high purity Bi, Sb, Te for the p-type (supplied by Alfa Aesar) and Bi, Se, Te for the n-type with slightly excess concentration of Te (supplied by Marlow Industries Inc.) were used as the starting materials. Also, an n-type target with 0.13 wt.% SbI_3 prepared at the University of Virginia was used. The targets used for pulsed laser deposition were obtained by cutting the ingots with a diamond saw parallel or perpendicular to the growth axis to yield small circular disks about 25mm in diameter and 10 mm in thickness. The same target materials were used for the deposition of several films. These target materials were loaded in a stage that was capable of being rotated both manually and by means of a motor. Either mica or AlN/ Si (100) or AlN/ Si (111) substrates were loaded in the stainless steel vacuum chamber after proper cleaning as described in the earlier part of this section. The substrates were loaded in such a manner that the center of the target approximately coincides with the center of the substrates that is approximately 40mm away (see Fig.3.3.1). The substrate support plate is also equipped with a tungsten bulb heater. The stainless steel vacuum chamber was pumped down first by means of a rotary pump and second by a turbo-molecular pump to a base pressure of 1×10^{-7} to 5×10^{-7} Torr for the required vacuum. The substrate was slowly heated to the desired temperature by means of an externally controlled variac and the temperature was monitored by a thermocouple

placed on the ceramic substrate holder. The substrate temperature was varied in the range of 300°C to 500°C for various depositions.

A pulsed Nd-YAG (neodymium-doped yttrium aluminum garnet) laser made by Spectraphysics (Quanta-Ray GCR 100 class) operating at 10 Hz frequency and delivering a first harmonic wavelength of 1064 nm that was transformed to the fourth harmonic $\lambda = 266$ nm by four-folding the frequency (Q-switch) was used to ablate the thermoelectric target material. The Quanta Ray GCR 100 laser is a lamp-pumped, Q-switched, Nd-YAG solid state laser. The key operating parameters include a peak pulse energy of 2.5 J at 1064 nm with a 10 Hz repetition rate and a cavity lifetime of 3 ns. The Quanta Ray laser is based on an electro-optic crystal that provides high loss in one state and lower loss in the second state. The threshold of the laser could be varied by adding a variable high/ low loss element into the laser cavity. This is equivalent to the quality factor of the cavity and therefore, the name Q-switching. This permits the laser cavity to store in a low Q state and then release it rapidly during a high Q state. The Quanta Ray laser used in our experiments is equipped with two gain elements; one of which is inside the cavity and provides the lasing and another element outside the cavity to increase the energy of each pulse.

The laser beam is focussed onto a small spot on the surface of the target by means of a converging lens of 50 mm focal length. The density of the laser fluence was adjusted by means of tuning the harmonic generators. The laser beam is made to strike the target at an approximate angle of 45° with respect to the normal. The schematic of our experimental PLD set up is illustrated in Fig. 3.3.1. The beam is rastered across the target to avoid non-stoichiometry resulting from localized evaporation in the target material.

The plume generated in this manner was deposited on mica and the substrate of aluminum nitride. The laser fluence was controlled by means of tuning the harmonic generators and the maximum energy used was about 0.25 to 0.3 J/ cm². The base pressure in the vacuum chamber was recorded to be in the range of 8×10^{-7} to 7×10^{-6} Torr (depending on the conditions) during the deposition and the deposition time was varied between 30 min to 1 hr. In addition, the films deposited on aluminum nitride substrates were deposited at a lower fluence of laser energy and were subsequently annealed at 200°C in the deposition chamber for 2 hours. During annealing, the base pressure in the vacuum chamber was the same as that obtained prior to start of the deposition. The deposition parameters that were varied over different experiments in this study were the laser fluence, substrate temperature, time of deposition, substrate orientation, and base pressure in the chamber. However, almost all of the depositions on aluminum nitride substrates were carried out at lower laser fluences that resulted in a finer plume, with less or no particulates.

The feasibility of depositing nanocrystalline thermoelectric films by means of pulsed laser deposition was also explored. A polycarbonate membrane filter about 13 mm in diameter and containing cylindrical pores with diameters of 0.2 µm was placed on top of a carbon holey grid specimen support and mounted on the substrate holder. The polycarbonate filter used in these experiments belongs to the Nuclepore[®] brand marketed by SPI Supplies Inc. The thermoelectric target material was ablated in the same manner as outlined above and the resulting plume passes through the nanopore filter. The filter restricts the size of the particles/ energetic species being deposited onto the holey grid. In

this experiment, the duration of deposition was 10 min and substrate was maintained at room temperature.

3.4 Characterization

3.4.1 X-ray Diffraction:

The thermoelectric thin films deposited using pulsed laser deposition and aluminum nitride films deposited using magnetron sputtering were characterized using x-ray diffraction to evaluate the crystallinity and growth orientation. A Rigaku diffractometer was used for x-ray diffraction analysis and θ - 2θ scans using nickel filtered copper- K_{α} radiation ($\lambda = 1.5406\text{nm}$) were obtained. An accelerating voltage of 27.5 kV and an anode current of 20 mA was used in these experiments.

3.4.2 Scanning electron microscopy:

Scanning electron microscopy (SEM) was used to examine the surface morphology and map the chemical composition of the deposited thin films and compare it with the target materials used in PLD. Since planar samples were used, there was no specific sample preparation necessary apart from the cleaning of the surface with acetone and methanol prior to observation in the SEM. The instrument used in this study was a Hitachi environmental scanning electron microscope, Hitachi S-3200 SEM. The samples were examined in the secondary electron mode while the Robinson backscatter detector was introduced during elemental quantification. The samples examined constituted all the target materials used in PLD and the resulting thin films deposited on mica and aluminum nitride substrates. An accelerating voltage of 10kV was applied and a magnification ranging from 100X to 7000X was used to examine the samples while the images were digitally captured using NIH image and ISIS softwares. The SEM is also equipped with

an IR chamberscope for viewing the sample. Since the substrate materials were electrically insulating, the samples were examined in a nitrogen atmosphere at a pressure of 30 Pa to avoid charging of surfaces.

3.4.3 Transmission electron microscopy:

Transmission electron microscopy calls for a very thin electron transparent sample. In order to determine the growth characteristics of the thermoelectric thin films on mica substrates, plan-view specimens were prepared. The sample was carefully cut into 3 mm by 4 mm pieces normal to the interfaces, using a pair of scissors. Since, the thickness of the mica substrates was only about 15 μm and the deposited films about 1.5 μm , there was no necessity to reduce the thickness further by means of a disc grinder and dimpling wheel. The samples were directly glued onto a copper O-ring by using M-Bond 610 adhesive, and baked on a hot plate at 100°C for 30 minutes. These discs were then loaded in a Gatan Duo Ion mill for the final stage of ion milling. The samples were milled only from the backside (starting from the mica side) at an incident angle of 12° with a high-energy argon gun. The ions are accelerated through a voltage of 5 kV and an ion beam current of 1 mA was used. The samples are milled till perforation occurs or till the sample becomes transparent. This enabled a large amount of the specimen area to become electron transparent and conducive for electron microscopy. Subsequently, a low-energy argon gun at an incident angle of 6° was used to clean the sample from the products generated during the milling operation. The plan-view samples were then examined in a TOPCON EM002B microscope at an accelerating voltage of 200 kV (with spherical aberration, $C_s = 0.5 \text{ mm}$, and a 0.18 nm point-to-point and 0.12 nm line-to-line resolution).

3.4.4 Electron Energy Loss Spectroscopy:

Electron energy loss spectroscopy (EELS) is a useful tool that provides information about chemical composition to prove segregation to defects, electrical, bonding and optical information with high spatial resolution. The nanocrystalline films deposited on the carbon holey grid with the aid of the polycarbonate filter were examined directly in a JEOL-JEM 2010 field emission electron microscope equipped with Gatan image filter and x-ray EDS system. Holey grids are covered with a fine layer of carbon and the carbon film is deposited in such a way that there are holes of a desired size in the carbon. The main purpose of these holes is to eliminate any absorption and scattering of the electron beam by the carbon film, which will generate noise and obstruct the signal. Carbon support films are quite robust and very popular for doing EELS where no support can be tolerated, and the data can be taken from those portions of the sample suspended over holes. In the JEOL 2010, Parallel Electron Energy Loss Spectroscopy (PEELS) can be simultaneously carried out to determine atomic structure and chemistry. It is capable of providing chemical information and bonding characteristics down to a resolution of 0.16 nm. High-resolution electron microscopy was performed on the nanocrystalline films deposited (on the carbon holey grid) at a magnification of 600,000X to 800,000X and EELS was performed in order to identify the different phases observed.

3.4.5. Thermopower Measurements:

Seebeck coefficient or Thermopower is basically defined as the rate of change of thermal emf (dV/dT) at a given temperature. In order to measure this property, a steady thermal gradient ought to be established across the sample that can be controlled and monitored easily. The sample was mounted on a glass plate that has a chip heater of

resistance 51Ω mounted on its end along with a few thermocouple leads to record temperature and voltage generated across the sample. The current through the chip heater was varied by using a Keithley 220 programmable current source and was responsible for generating a thermal gradient across the glass plate. Three Keithley 195A digital multimeters were simultaneously used to measure the temperature gradient and voltage generated across the sample. The ends of the temperature measuring thermocouple leads were immersed in a liquid nitrogen tank as a reference standard. All the thermocouple leads are attached to the sample by means of an electrically conductive silver paint. The sample chamber consists of three concentric cylindrical shells to thermally isolate the sample from the ambient and the outermost shell is evacuated to a base pressure of 10 mTorr by means of a mechanical pump. The arrangement also included a Lakeshore 120 power source and a Keithley 199 system DMM scanner to supply about $15\ \mu\text{A}$ of current that switched on and off once every minute. This current causes a small potential drop in the specimen and another thermocouple was used to measure this voltage gradient. By knowing the geometry of the sample, and using the basic equation $\rho = R \cdot A / l$ the resistivity was determined using the same potential difference. The specimen support plate has been described in the earlier section and is illustrated in figure 2.6.6.1.

The experimental results are discussed in the next section.

Chapter 4

Results

The results of all the characterization techniques that have been performed to test the thermoelectric thin films deposited by pulsed laser ablation are presented below.

The main technological challenges for the development of thermoelectric thin films are to maintain the desired stoichiometry, adequate adhesion to the substrate, and to obtain the desired crystallographic growth orientation. Successful thin film thermoelectric cooling also requires integration with thin film diamond or aluminum nitride substrate heat spreaders and the device wafers. The microstructure of the films is very important since grain boundaries and crystalline defects increase the resistivity by scattering the charge carriers. In addition, to maintain sufficient purity and control the doping levels are also critical. The characterization techniques have been performed to study the microstructure, chemical composition, surface morphology and thermal transport properties. The samples used with the characterization techniques and the significance of the results were listed in table 3.1. The thickness of the films deposited was measured by means of a profilometer to be in the range of 1.5 μm . The duration of deposition for these films was one hour which indicates a deposition rate of 4.16 $\text{\AA}/\text{sec}$.

4.1 X-ray diffraction

X-ray diffraction was performed on the samples to evaluate the crystallinity and the crystallographic growth orientation of the thermoelectric thin films and further to compare with the respective target materials used in pulsed laser deposition. The results of X-ray diffraction on the target materials: p-Bi_{0.5}Sb_{1.5}Te₃, n-Bi₂Te_{2.7}Se_{0.3} and n-(Bi₂Te₃)₉₀(Sb₂Te₃)₅(Sb₂Se₃)₅ (0.13 % wt SbI₃ doped), shown in figures 4.1.1 (a)- (c), illustrate the polycrystalline nature of the target materials. The patterns obtained from the thermoelectric thin films deposited by pulsed laser ablation on mica at a substrate

temperature of 350°C are shown in figures 4.1.2 (a)- (c), and illustrate preferential growth with the c-axis along the growth direction. The (0 0 3n) family of peaks correspond to the thermoelectric film and are seen along with the mica substrate peaks that are designated by m(0 0 2p). Here n and p are positive integers that takes values from 3 to 8. For every m(0 0 2p) peak arising from the mica substrate there exists a (0 0 3n) peak corresponding to the film. This result confirms that the films are well textured. In addition, small peaks corresponding to weak reflections such as (0 1 11), (2 0 5) and (0 2 10) are also present in the n-type films.

X-ray diffraction was also performed to evaluate the crystal perfection and orientation of aluminum nitride deposited on silicon (1 0 0) and (1 1 1) substrates by reactive magnetron sputtering. The results are illustrated in figures 4.1.3 (a) and 4.1.3 (b), respectively, and indicate preferential growth of aluminum nitride on the (0 0 0 2) basal plane in both cases. The silicon (4 0 0) and (2 0 0) peaks arising from the (1 0 0) substrates and a weak (0 0 4) AlN reflection are also seen in fig. 4.1.3 (a). The full width at half maximum (FWHM) of the AlN basal plane (0 0 0 2) peak on the silicon (1 0 0) substrate was 1072.6 arcsecs ($\approx 0.3^\circ$). From figure 4.1.3 (b), the silicon (1 1 1) peak arising from the substrate and a weak (1 0 0) AlN reflection are seen in addition to the strong reflection from the (0 0 0 2) AlN basal plane. The full width at half maximum (FWHM) of the (0 0 0 2) basal plane in this case was found to be 71.99 arcsecs ($\approx 0.02^\circ$). Results of X-ray diffraction on thermoelectric films deposited on AlN/ Si (1 0 0) and AlN/ Si (1 1 1) are illustrated in figures 4.1.4 (a) and 4.1.4 (b), respectively. It is seen that peaks corresponding to strong reflections from only the (0 0 6) and (0 0 9) planes are present in addition to the reflections from silicon and aluminum nitride, and thus indicate

highly textured growth along the c-axis. In addition a small peak corresponding to (1 0 10) can also be seen in fig. 4.1.4(a). Thus, X-ray diffraction shows highly textured growth of the n-type and p-type films on both mica and aluminum nitride substrates.

4.2 Scanning electron microscopy (SEM)

The growth and morphology of thermoelectric thin films deposited on mica and aluminum nitride substrates have been studied using Scanning Electron Microscopy and the results are shown in figures 4.2.1 and 4.2.2, respectively. The images shown were obtained for the films deposited at a substrate temperature of 350 °C. The images reveal uniform film deposition on the substrates along with the presence of particulates that are indicative of high deposition rates. There are two types of particulates that are observed: micron or sub-micron droplets and large particulates that are shaped like flat disks. The particulates arise due to porous nature of the target material and high incident laser energy. The presence of the large droplets in the films has been reduced by lowering the incident laser fluence used to ablate the target material, as seen in the films deposited on aluminum nitride (fig. 4.2.3). In addition, the presence of stripes seen in fig. 4.2.1 are indicative of the cleavage steps present on the mica substrate.

A map of the constituent elements in the SEM image is obtained by using x-ray analysis. The ISIS software enables the beam to scan the sample and create digital images or maps for each element. Thus, we have detected the distribution of different elements comprising the n-type and p-type films from the x-ray maps. The x-ray maps of n-type films deposited at high laser fluences on mica and aluminum nitride substrates are shown here in fig. 4.2.4 and 4.2.5, respectively. These maps were obtained from regions similar to those shown in the SEM images. Figure 4.2.4 illustrates the presence of the elements

bismuth, antimony, tellurium and selenium from the film and the elements potassium, aluminum, silicon, and oxygen that constitute the mica substrate. The presence of aluminum, nitrogen and silicon from the substrates is seen in fig. 4.2.5, in addition to the elements: bismuth, selenium, and tellurium that comprise the thermoelectric film.

The electron-beam interactions with the specimen produce x-ray fluorescence. The energy of each x-ray photon generated is a characteristic of the element from which it is generated and is detected using an energy dispersive spectrometer. The EDS microanalysis system available with the SEM collects the x-rays, sorts and plots them according to energy, identifies and labels the elements responsible for the peaks in the energy distribution.

The EDS spectra obtained in this manner on the n-type films deposited on mica and aluminum substrates are illustrated in figures 4.2.6 and 4.2.7, respectively. The data collected in this manner was used to perform a full quantitative analysis of both the n-type and p-type thin films and the target materials showing their respective compositions. The results are summarized in Table 4.2. It is noted that all the films are deficient in tellurium compared to the target material. Tellurium has the highest vapor pressure among the elements in the target. It is also noted from the table that the films deposited on aluminum nitride are closer to the target stoichiometry than the films deposited on mica. The analysis also shows that the composition of many of the particulates is very much similar compared to the rest of the film. The results of quantitative analysis of films deposited at better base vacuum levels ($= 1 \times 10^{-7}$ Torr) on aluminum nitride are also listed in Table 4.2. It is seen that a slight improvement in the composition of the films is obtained.

4.3 Transmission electron microscopy (TEM)

Plan-view samples of thermoelectric thin films deposited on mica were examined in a TOPCON EM002B microscope at an accelerating voltage of 200 kV (with spherical aberration, $C_s = 0.5$ mm, and a 0.18 nm point-to-point and 0.12 nm line-to-line resolution). The selected area diffraction pattern (SADP) of the mica substrate is shown in fig. 4.3.1 (a) and illustrates the reflections obtained from the [0001] hexagonal zone axis. The SADP obtained from the thermoelectric film deposited on mica substrates is shown in fig. 4.3.1 (b). The presence of satellite spots in addition to those obtained for mica account for the reflections arising from the thermoelectric film. This is indicative of a highly preferred growth direction oriented along the c-axis of the substrate. The TEM bright field images obtained at high magnifications are shown in figures 4.3.2 (a) and (b). The presence of hexagonal crystallites in the film that are oriented with the c-axis perpendicular to the plane of the substrate are seen. In addition, high-resolution electron microscopy was performed on the nanocrystalline films deposited on a carbon holey grid using a polycarbonate filter that had 0.2 μm diameter pores. A JEOL-JEM 2010 field emission electron microscope equipped with Gatan image filter and x-ray EDS system was used for this purpose. A high-resolution lattice image obtained at a magnification of 600,000X to 800,000X is shown in fig. 4.3.3 and reveals the film to be composed of several nanocrystalline areas. Electron energy loss spectroscopy (EELS) was performed in the nanocrystalline grains to identify the different elements present and the results are shown in fig. 4.3.4. The edges detected at 463.6 eV and 572.1 eV correspond to Bi-N₄ and Te-M₅, respectively.

4.4 Measurement of Thermopower

The variation of Thermopower or Seebeck coefficient with temperature for a film deposited on mica is shown in fig. 4.4.1. A consistent decrease in the value of Seebeck coefficient with decrease in temperature that is characteristic of all thermoelectric materials is obtained. On all the films and their target materials, Seebeck coefficient was only measured as a function of dT and the results are summarized in Tables- 4.4.1 and 4.4.2. The values of the Seebeck coefficient remained fairly constant in the range of temperature measured, from about 292 K to 310 K (figures 4.4.2 and 4.4.3) for films on mica while the dT values ranged from about 0 to 16 K. However, for the films on AlN/ Si (1 0 0) and AlN/ Si (1 1 1) the temperature range was 296- 298 K while the dT values ranged between 0 to 3.2 K, as seen in figures 4.4.4 and 4.4.5. This result is attributed to the higher thermal loads involved in heating the thicker samples using a chip heater as compared to the films on thin mica sheets. In order to obtain thermopower measurements on the target materials, they were cut in the form of bars that were about 2 cm in length. It is seen that the Seebeck values are as high as $-224.51 \mu\text{V/K}$ for the n-type $\text{Bi}_2\text{Te}_{2.7}\text{Se}_{0.3}$ bulk sample from which the targets were made. In comparison, the best n-type films on mica obtained at a substrate temperature of 350°C showed a value of $-74.15 \mu\text{V/K}$. The Seebeck coefficient obtained for the p-type $\text{Bi}_{0.5}\text{Sb}_{1.5}\text{Te}_3$ bulk sample was only $40.52 \mu\text{V/K}$. Compared to this value, the Seebeck coefficient in the best p-type films deposited on mica was $86.64 \mu\text{V/K}$. However, the Seebeck coefficient could not be experimentally determined from the n-type $(\text{Bi}_2\text{Te}_3)_{90}(\text{Sb}_2\text{Te}_3)_5(\text{Sb}_2\text{Se}_3)_5$ target material since it was too small to be made in the form of a long bar. The thermoelectric thin films deposited on aluminum nitride however resulted in larger values of thermopower compared to those on

mica substrates. The best n-type films on aluminum nitride showed a Seebeck value of – 154.69 $\mu\text{V/K}$ while the best p-type films resulted in a value of 142.20 $\mu\text{V/K}$ and were both obtained at a substrate deposition temperature of 350 °C. The improved values of thermopower can be related to the use of lower incident laser fluence and inclusion of an additional annealing step for two hours at 200°C. A more detailed analysis of this data will be presented in the next section. Also, in order to obtain improvement in thermopower, depositions were carried under at better pre-deposition vacuum levels in the range of 1×10^{-7} Torr. The data obtained has been summarized in Table- 4.4.3 and illustrates a marginal improvement in thermopower with better pre-deposition vacuum.

4.5 Hall-effect Measurements

Hall effect measurements were performed on all the thin film samples to measure Hall mobility, carrier concentration and electrical resistivity and the results are shown in Tables- 4.4.1 and 4.4.2. It is seen from the results shown in tables- 4.4.1 and 4.4.2 that the films deposited from the SbI_3 doped target showed a higher Seebeck value and also a higher mobility in most of the cases. When the mica substrates were used, better n-type films were obtained at a substrate temperature of 350°C whereas better p-type films were obtained at 300°C. The electrical resistivity was found to be $1.71 \times 10^{-3} \Omega\text{-cm}$ for the n-type $\text{Bi}_2\text{Se}_{2.7}\text{Te}_{0.3}$ films deposited on mica at 350°C compared to a bulk resistivity of $1.02 \times 10^{-3} \Omega\text{-cm}$. The n-type film deposited from the $(\text{Bi}_2\text{Te}_3)_{90}(\text{Sb}_2\text{Te}_3)_5(\text{Sb}_2\text{Se}_3)_5$ (0.13 % wt SbI_3 doped) target, showed a slightly higher resistivity of $5.06 \times 10^{-3} \Omega\text{-cm}$. Also, the highest carrier mobility obtained in all these films was for the n-type films deposited at a substrate temperature of 350°C with SbI_3 doping and has a value of $40.4 \text{ cm}^2/\text{V}\cdot\text{sec}$ for a carrier concentration of $2.63 \times 10^{19} \text{ cm}^{-3}$. The best p-type films on mica showed a

mobility of $26.32 \text{ cm}^2/\text{V}\cdot\text{sec}$ while the resistivity was measured to be $1.04 \times 10^{-2} \Omega\text{-cm}$. Improved n-type films and p-type films in terms of both thermopower and mobility were obtained on the aluminum nitride substrates. A mobility of $68.84 \text{ cm}^2/\text{V}\cdot\text{sec}$ was obtained on the n-type films (with SbI_3 doping) deposited on $\text{AlN}/\text{Si}(1\ 1\ 1)$ at a substrate temperature of 350°C . The resistivity measured on this particular film was about $9.48 \times 10^{-3} \Omega\text{-cm}$. Films deposited on $\text{AlN}/\text{Si}(1\ 0\ 0)$ showed better properties compared to those on $\text{AlN}/\text{Si}(1\ 1\ 1)$. The best p-type characteristics are obtained in the films deposited on $\text{AlN}/\text{Si}(1\ 0\ 0)$ at a substrate temperature of 350°C . The carrier mobility and electrical resistivity were found to be $35.33 \text{ cm}^2/\text{V}\cdot\text{sec}$ and $1.94 \times 10^{-2} \Omega\text{-cm}$, respectively.

Chapter 5

Discussion

5.1 X-ray diffraction

Initially single-crystal mica sheets were chosen as the substrate materials for the deposition of the thermoelectric thin films. Cleaved mica substrates provide the hexagonal in-plane symmetry with large and atomically smooth surfaces. In addition, mica sheets are flexible, thermally conducting and electrically insulating and hence, suitable for thin-film device applications. Bi_2Te_3 based thermoelectric compounds are expected to crystallize in a hexagonal unit cell with the growth oriented along the c-axis. Bi_2Te_3 based materials are highly anisotropic with highest Seebeck coefficient for films oriented along the c-axis. The presence of the (0 0 3) family of peaks in the x-ray diffraction scans [figures 4.1.2 (a)- (c)] illustrates that the growth is textured. Textured growth implies that all the grains are oriented along one particular direction that is the c-axis in this case. However, limited adhesion and presence of steps on mica substrates prompted us to investigate other substrate materials with higher thermal conductivity and favorable crystallographic orientation. In addition, it has been further established that the use of diamond or aluminum nitride substrate with high thermal conductivity is necessary to achieve two orders of magnitude higher power density dissipation using the thin film coolers¹. Hence, successful thin film thermoelectric cooling requires integration with thin film diamond or aluminum nitride substrates that are well-established heat spreaders².

The growth of hexagonal AlN is expected to be on the close packed or (0 0 0 1) basal plane. The presence of the predominant (0 0 0 2) basal plane peak [figures 4.1.3 (a) 4.1.3 (b)] indicates that the growth of AlN by reactive magnetron sputtering is highly textured. Textured AlN films are also good diffusion barriers since all randomly oriented and large angle grain boundaries are eliminated. The full width at half maximum

(FWHM) of the (0 0 0 2) peaks of the films deposited on both Si (1 0 0) and Si (1 1 1) substrates is an indication of the crystalline quality of the film and concentration of defects. A smaller value of FWHM indicates better crystallinity and less defects. The FWHM values of 0.3° and 0.02° indicate good crystalline nature of the films. Furthermore, thermoelectric films deposited on aluminum nitride substrates by pulsed laser ablation are highly adherent and textured. Peaks corresponding to strong reflections from only the (0 0 6) and (0 0 9) planes in addition to the reflections from silicon and aluminum nitride are indicative of textured growth along the c-axis as seen from figures 4.1.4 (a) and (b).

5.2 Scanning electron microscopy

Examination of the thermoelectric films by scanning electron microscopy revealed uniform film deposition on the substrates along with the presence of particulates. The presence of particulates is an indication of high deposition rates. Particulates are predominantly caused by the phenomena of surface roughening (exfoliation) and shock wave recoil. The incident laser beam produces surface irregularities on the target such as craters, columns and pits as a function of time. The laser-induced thermal and mechanical shock waves dislodge particles in the form of molten micron sized globules that get deposited on the substrate, as seen in figures 4.2.1 and 4.2.2. The films shown in these figures were deposited at an approximate incident energy of 0.25 J/ cm^2 . The density of these droplets could be decreased by lowering the laser fluence as seen from fig. 4.2.3. In this case the incident laser fluence was reduced by a factor of two. It has also been found that increase in substrate temperature beyond 450°C lead to deposition of coarser films. The x-ray maps obtained from these films

(figures 4.2.4 and 4.2.5) indicate the presence of the elements bismuth, antimony, tellurium, and selenium, in addition to the elements from the substrates. X-ray maps are useful for qualitative analysis and the uniform distribution of all the elements indicates no preferential segregation in the films. The particulates shown in fig. 4.2.5 are rich in bismuth and tellurium as seen in the X-ray map. Tellurium has the highest vapor pressure among the constituent elements in the target and the formation of tellurium rich particulates suggests that these are dislodged from the target without any evaporation during pulsed laser deposition.

Energy dispersive spectrometry (EDS) was used to analyze the chemical composition of the films and the results are shown in Table 4.2.1. Among the constituent elements of the target materials, tellurium has the highest vapor pressure. We have observed that tellurium deficiency is highly pronounced in the films deposited on mica substrates. The analysis also shows that the composition of most of the particulates is very much similar compared to the rest of the film. The interaction between the laser incident energy and target surface raises the temperatures at which tellurium gets preferentially depleted and thus the target surface gets depleted in tellurium³. Continuous laser ablation encounters target surface that is deficient in tellurium and thus, the film is also deficient in tellurium. There exists a possibility that these elements can be ejected out from the film or even get recondensed on the target or other areas. In addition, secondary interactions of the beam with the plume result in removal of volatile species like tellurium from the film. However, the composition of the films deposited on aluminum nitride are closer to the target stoichiometry and also showed less variation between the particulates and the film. This may be explained by the low density of plume

that was generated at lower laser fluence in the depositions on aluminum nitride substrates. In addition, the EDS analysis of films deposited on aluminum nitride at better pre-deposition vacuum conditions ($= 1 \times 10^{-7}$ Torr) show a slight improvement in composition. Hence, by generation of low density plume at lower laser fluences from the target, and at better pre-deposition vacuum nearly congruent transfer of target stoichiometry was obtained.

5.3 Transmission electron microscopy

Plan-view samples of thermoelectric thin films deposited on mica examined by transmission electron microscopy illustrate that the films are extremely well textured with a highly preferred growth direction oriented along the c-axis of the substrate. The TEM bright field images in figures 4.3.2 (a) and (b) show the presence of hexagonal crystallites that are oriented with their c-axis perpendicular to the plane of the substrate. Similar observations were made previously by J.C. Tedenac et al⁴. The crystal structure of these materials is composed of stacking of atomic layers in the order of Te/Bi/Te/Te/Bi/Te/Bi/Te/Te/..... oriented along the c-axis. The Te/ Te layers are held together by weak Van der Waal forces⁵. The microstructure of the films is very important since grain boundaries and crystalline defects increase the resistivity by scattering the charge carriers. High-resolution electron microscopy performed on the films deposited on a carbon holey grid using a polycarbonate nanofilter illustrates that nanocrystalline films are obtained by means of a template deposition using pulsed laser deposition. The corresponding high-resolution lattice image obtained at a magnification of 800,000X and shown in fig. 4.3.3 illustrates the presence of nanostructured crystallites in the deposited films. Electron energy loss spectroscopy (EELS) performed on these films detected

energy loss edges at 463.6 eV and 572.1 eV that correspond to Bi-N₄ and Te-M₅ respectively. These results are exciting considering the recent advances in thermoelectric properties that could be obtained using superlattices and quantum dots. In order to attain higher values of Z for simple materials the pre-requisite is higher thermopower values α , higher electrical conductivity σ , and lowered thermal conductivity κ . According to equation (5.1),

$$Z = \frac{\alpha^2 \sigma}{\kappa} = \frac{\alpha^2 \sigma}{\kappa_L + \kappa_e} \dots \dots \dots \text{eq. (5.1)}$$

However, increasing thermopower is accompanied by decrease in electrical conductivity while increasing electrical conductivity results in enhanced electronic contribution towards the thermal conductivity. Therefore, there exists a certain limit for conventional thermoelectrics beyond which modification of one parameter adversely affects other transport properties leading to insignificant changes in the values of Z. The above described barrier for improvement in Z can be surpassed with the use of multilayered superlattices. This enhancement in the values of ZT is a result of effects of quantum confinement and an increase in the electron density of states when either the layer thickness or the size of the nanocrystallites is around 1 nm, as suggested by Hicks and Dresselhaus⁶. Moreover, layering reduces the phonon thermal conductivity as phonons tend to get scattered by the interfaces between layers, thus increasing Z. ZT values in superlattices produced by alternately depositing 1 to 4 nm thin films of Bi₂Te₃ and Sb₂Te₃ using MOCVD were found to be as high as 2.4 and 1.2 for p-type and n-type, respectively⁷. Also, ZT values nearly equal to 2 just above room temperature for quantum dot superlattices produced using molecular beam epitaxy have been reported by Harman

et al⁸. From our preliminary experiments with templated deposition, we have shown that nanocrystallites of thermoelectric materials are obtained with pulsed laser ablation.

5.4 Transport Properties

The largest Seebeck values obtained for the films deposited on mica substrates are about 2.5 times lower than the bulk materials^{9,10}. A Seebeck coefficient of $-224.51 \mu\text{V/K}$ was obtained on the $\text{Bi}_2\text{Se}_{2.7}\text{Te}_{0.3}$ bulk sample. However, the p-type $\text{Bi}_{0.5}\text{Sb}_{1.5}\text{Te}_3$ bulk sample resulted in a Seebeck coefficient of $40.52 \mu\text{V/K}$. The p-type target was manufactured by powder sintering where as the n-type targets were grown by the Bridgman technique. The lower value of Seebeck coefficient in the p-type target may be attributed to higher porosity and anisotropy in the specimen. The lower values of Seebeck coefficient or thermopower for the films deposited on mica are related to the high density of particulates, defects and stresses in the films. Further investigation by TEM is needed to provide more information on the nature of line defects and grain boundaries. It is evident from the improved values obtained on the aluminum nitride substrates that when a low-density plasma was used, films contained fewer particulates. Also, an annealing step was used to relieve the large thermal stresses and reduce point defects that are inevitable to develop at the interface since there is a large difference in the values of thermal expansion coefficient between the thermoelectric films and the mica/ aluminum nitride substrates. The thermal expansion coefficient of Bi_2Te_3 based materials is on the order of $20 \times 10^{-6}/\text{K}$ while that of AlN/Si is about $2 \times 10^{-6}/\text{K}$. The large difference in the thermal expansion coefficients of the film and substrate are responsible for large tensile thermal strains in the thin films upon cooling from which the defects are generated. The thermoelectric compounds possess low thermal conductivity where as the

substrates used in this study are excellent thermal conductors. The highest Seebeck value, mobility and carrier concentration have been listed in Table 5.4.1. The thermal conductivity for the thin films has been assumed to be about one-tenth of the bulk materials. Phonon scattering at the grain boundaries and defects in the films are known to reduce the thermal conductivity below that of the bulk. We have assumed the thermal conductivity values of 0.0012 W/cmK and 0.0014 W/cmK for the n-type and p-type, respectively and determined the best values of figure of merit for our films at 300K. For films on mica, ZT values of 0.15 and 0.42 are obtained for the p-type and n-type that are quite low. However, the ZT value for the best n-type films deposited on aluminum nitride was found to be 0.63 and that for the p-type films was 0.22. These results have been summarized in Table 5.4.2 while the properties of the respective bulk materials are listed in Table 5.4.3. The value obtained for the n-type films is comparable to that obtained for optimized bulk materials ($ZT \approx 0.96$). It is known that the figure of merit is reduced with decreasing thickness of the films below $5 \mu\text{m}^1$. The thickness of the films deposited in our experiments is about $1.5 \mu\text{m}$. Therefore, optimization of film thickness to achieve the desired properties is needed.

The Seebeck values obtained on all our thin films were shown as a function of the carrier concentration in figures 5.4.1 and 5.4.2 for films on mica and figures 5.4.3 and 5.4.4 for films on aluminum nitride. The observed variation is an increase in the Seebeck values with decreasing carrier concentration, which is in tune with the following relation for α . The thermoelectric power, α of any material can be expressed by the basic equation¹¹:

$$\alpha_{n,p} = \pm k_B/q[r + 2 + \ln \frac{2(2\pi m_n k_B T)}{nh^3}]^{1.5}, \text{ (with -ve sign for n and +ve for p-type)}$$

$\Rightarrow \alpha_{n,p} \propto \pm \ln(n)$, since all other terms are constant.

Where k_B is the Boltzmann's constant, r the scattering parameter, m_n effective mass of the charge carriers, T the temperature, n the carrier concentration and h the Planck's constant.

This result is exactly reproduced in the $\alpha_{n,p}$ versus $\ln(n)$ and emphasizes the fact that carrier concentration is an important factor that determines the thermoelectric properties of the films. In order to improve the Seebeck values, target materials with varying compositions of dopants need to be experimented with, since dopant evaporation in the plume can significantly impact the carrier density in the thin films. Moreover, maximizing the value of ZT is equivalent to maximizing the parameter $N m^{*3/2} \mu / \kappa_L$ where m^* is the effective mass of the majority charge carrier, N the number of equivalent parabolic bands and μ the carrier mobility¹². This implies that enhancement in ZT is directly proportional to mobility μ , since all other factors are constants. The calculated values of ZT for all the thin films have been plotted as a function of mobility as well as carrier concentration as shown in figures 5.4.5 – 5.4.8. The variations extrapolated from the graphs corroborate the fact that higher carrier mobilities and optimized carrier concentration are necessary to obtain thin films with higher ZT values. The mobilities in the thermoelectric thin films deposited on mica and aluminum nitride substrates were when compared to the bulk values¹⁰. The lower values of mobility in the films may be attributed to scattering by point defects and impurities. Recombination centers and traps in addition to impurity scattering are present at the grain boundaries. Though it is evident from tables 4.4.1 and 4.4.2 that the films deposited from the n-type

(Bi₂Te₃)₉₀(Sb₂Te₃)₅(Sb₂Se₃)₅ (with 0.13 wt.% SbI₃) target showed a higher Seebeck value as well as a higher mobility, further improvements are need to attain higher ZT values.

References

1. J.W. Vandersande and J-P. Fleurial, 15th International Conference on Thermoelectrics, Pasadena, CA, pp. 252-255, 1996.
2. K. Jagannadham, Solid-State Electronics, Vol. 42, No. 12, pp. 2199-2208, 1998.
3. A. Dauscher, A. Thomy and H. Scherrer, Thin Solid Films, Vol. 280, pp. 61-66, 1996.
4. J.C. Tedenac, S. Dal Corso, A. Hadioux, S. Charar, B. Liautard, MRS Sym. Proc., Vol. 545, pp. 93, 1998.
5. J. R. Weise and L. Muller, J. Phys. Chem. Solids Vol.15, No.13, 1960.
6. L. D. Hicks, M. S. Dresselhaus, Phys. Rev. B. Vol. 47, No.19, pp. 12727, 1993.
7. R. Venkatasubramanian, E. Siilvola, T. Colpitts, B. O'Quinn, Nature Vol. 413, pp.597 2001.
8. T. C. Harman, P. J. Taylor, D. L. Spears, M. P. Walsh, J. Electron. Mater. Vol. 29, No.1 2000.
9. M.H. Ettenberg, W.A. Jesser and F.D. Rosi, 15th International Conference on Thermoelectrics Proceedings, Pasadena, CA, pp. 52-56, 1996.
10. J. Seo, K. Park, C. Lee and J. Kim, Mat. Res. Soc. Symp. Proc. Vol. 478, pp. 127, 1997.
11. A.F. Ioffe, Semiconductor Thermoelements and Thermoelectric Cooling, Infosearch Limited, London, pp. 20, 1957.
12. G.D. Mahan, B.C. Sales, J.W. Sharp, Physics Today, pp.43, March 1997.

Chapter 6

Conclusions

6.1 Conclusions

From the results obtained by X-ray diffraction, scanning and transmission electron microscopy, it has been shown that textured growth of thermoelectric films on aluminum nitride and mica substrates can be achieved using pulsed laser deposition. The films showed uniform thickness and high crystalline quality with a preferred (0 0 n) alignment with the substrates. However, a primary difficulty in the deposition of thermoelectric films is to maintain stoichiometry. Pulsed laser deposition has the advantage of maintaining congruent transfer of the target composition to the thin films under the suitable conditions of lower laser fluence, low density plume and ideal substrate temperature. The film quality in terms of composition and crystal perfection was studied as a function of growth temperature. It was found that films deposited at 300 to 350°C gave improved crystallinity and thermoelectric characteristics. The Seebeck coefficient, electrical resistivity and Hall mobility were measured as a function of temperature and compared with the bulk properties. The best n-type films were obtained by ablating the $(\text{Bi}_2\text{Te}_3)_{90}(\text{Sb}_2\text{Te}_3)_5(\text{Sb}_2\text{Se}_3)_5$ target that was doped with 0.13 wt.% of SbI_3 onto aluminum nitride substrates and exhibited a ZT value of 0.63. The p-type films deposited from a $\text{Bi}_{0.5}\text{Sb}_{1.5}\text{Te}_3$ target however, showed a lower value of 0.22. Compared to the properties of the bulk materials, we find that the values of Seebeck coefficient are lower and the electrical resistivity is higher. These results indicate that the carrier concentration is higher than the optimum values required for higher ZT values and most importantly the mobility of the charge carriers in the films are low. These values can be improved by better control of stoichiometry, increase in film thickness, and minimization of the volume fraction of particulates, pores and atomic level point defects. An

improvement in the thermoelectric properties by reduction in laser induced particulates has been demonstrated by the use of lower incident laser energy for ablation of the target. In addition an annealing step after the deposition of the films is found to reduce the defect density. Also, the thermoelectric figure of merit, ZT is smaller with lower thickness of the films. Therefore, optimization of the thickness of the films is essential. The present work has illustrated the use of AlN/ Si (an efficient heat spreader) as a favorable substrate material for the deposition of thermoelectric thin films. Thus, by direct growth of the thermoelectric films on composite heat spreaders on silicon, interfacial thermal resistances associated with bonding and the solder layers has been eliminated. Also, the additional cost of bonding to silicon wafers has been reduced and reliability of the heat spreaders and cooling devices is improved.

In summary, it has been conclusively shown that there is great potential for producing efficient thermoelectric thin films by means of pulsed laser physical vapor deposition. In addition, we have demonstrated the ability to deposit nanocrystalline thermoelectric thin films that show improvement in the values of ZT . Since, thin film deposition by pulsed laser deposition, and DC RMS, is less expensive, easy to implement, and operate, the choice of deposition of thermoelectric thin films integrated with composite aluminum nitride/diamond heat spreaders is definitely a cost effective alternative for effectively cooling the devices.

6.2 Future work

Though the results obtained in the present study are significant, it cannot be considered complete unless higher values for thermopower and figure of merit comparable to or better than bulk values are achieved. Since, the formation of microscopic particulates is

considered a drawback in the effective deposition of thin films; it should be minimized in pulsed laser deposition. A more extensive characterization of the defects like dislocations, voids, impurities, point defects, and presence of complex and amorphous phases present at the grain boundaries and at the interface of the films with the substrate need to be performed. Also, sequential deposition of the n- and p-type films should be chosen to complete a thermoelectric module formation with the help of a suitable mask. Optimization of the thickness of the film and the cross-section of the legs will be an important part of the research. Diffusion barrier coatings and metallization layers also need to be deposited to produce a working module. More importantly, the multilayer structure needs to be characterized for microstructural and interfacial integrity. Electrical and thermal conductivity ought to be determined accurately and correlated with the microstructure. New thermoelectric film compositions that include new skutterudite compounds with rattling rare earth atoms (void filling) at the center of unit cell (RM_4B_{12} ; $R=Ce$, $M=Fe$, Ru ; $B=P$, As , Sb) that will exhibit low lattice thermal conductivity and thereby high figure of merit need to be experimented with. Moreover, deposition of quantum well structures with periodicity of 10 to 50 Å by laser physical vapor deposition will pose a challenge and holds a great promise for low cost formation of high quality thermoelectric devices suitable for the cooling of advanced electronic devices.

Compound	Structure	Average Atomic Mass	Bandgap, eV Thermal	Bandgap, eV Optical
Bi ₂ Te ₃	Rhombohedral	16.02	0.16	0.13
Sb ₂ Te ₃	Rhombohedral	125.3	0	0.3
Sb ₂ Se ₃	Orthorhombic	96.1	---	1.2

Table 2.2.1 Crystal structure, average atomic mass and bandgap of Bi₂Te₃, Sb₂Te₃, and Sb₂Se₃.

Thermal conductivity	140-180 W/m-K
Bandgap	6.2ev
Resistivity	10 ¹⁴ ohm-cm
Thermal expansion (RT-400°C)	4.5 x 10 ⁻⁶ /°C
Dielectric constant	9
Flexural strength	320Mpa
Young's Modulus	350Gpa
Density	3.26 gm/cm ³
Specific heat	0.74J/gm/K
Chemical resistance	Good, but etchable like other nitrides with a combination of HF/HNO ₃ .

Table 2.5.1 Fundamental properties of aluminum nitride.

Characterization technique	Samples prepared	Reason
X-Ray diffraction.	(a) AlN/ Si. (b) p-type and n-type films on mica and on AlN/Si(100).	(a) To check for the growth orientation of AlN over Si. (b) To check for the growth orientation of the TE films on the respective substrates.
Scanning electron microscopy (SEM).	(a) p-type and n-type films on mica and on AlN/Si(100).	(a) To check for the surface morphology of the thermoelectric films deposited using PLD. (b) To determine the film composition and map the various constituents using energy dispersive spectroscopy.
Transmission electron microscopy (TEM).	(a) Plan-view sample of thermoelectric films on mica. (b) Nanocrystalline films deposited on Carbon holey grid.	(a) To check for growth orientation and characteristics of p- and n-type films on mica. (b) To check the feasibility of depositing nanocrystalline films using PLD and study the composition using EELS and orientation using HREM.
Thermopower measurements.	(a) Thermoelectric films on mica. (b) Thermoelectric films on AlN/ Si (100).	To determine the thermopower or Seebeck coefficient of the thermoelectric thin films deposited by PLD.
Four point probe and Hall mobility.	(a) Thermoelectric films on mica. (b) Thermoelectric films on AlN/ Si (100).	To determine the resistivity, sheet resistance, number, type and mobility of charge carriers.
Thermal Conductivity – 3ω technique.	(a) Reference AlN/ Si (100) with Fox-17 film. (b) Thermoelectric films on AlN/ Si(100) with Fox-17 film.	To determine the thermal conductivity of the thermoelectric thin films on AlN/ Si(100) by comparing with reference AlN/ Si (100).

*TE refers to thermoelectric

Table 3.1 Summary of characterization techniques.

	Element	Target	Films on Mica			Films on AlN/ Si(100)			Films on AlN/Si(100) deposited at base pressures of 1×10^{-7} Torr		
			over-all	particulates	film	overall	particulates	film	overall	particulates	film
p-Bi _{0.5} Sb _{1.5} Te ₃	Bi	11.57	12.48	11.35	13.2	11.18	10.32	11.55	11.06	10.12	11.81
	Sb	29.18	36.97	38.47	35.68	34.47	36.18	30.47	30.69	30.85	30.03
	Te	59.25	50.55	49.08	51.11	57.35	58.5	57.98	58.13	59.03	58.16
n-(Bi ₁₂ Te ₃) ₉₀ (Sb ₇ Te ₃) ₅ (Sb ₂ Se ₃) ₅ (0.13 wt% SbI ₃ doped)	Bi	27.48	32.01	31.35	32.75	30.26	29.72	31.14	28.59	29.18	28.44
	Sb	13.71	17.13	16.81	19.14	13.26	13.34	12.03	14.27	14.34	14.32
	Te	55.9	49.12	49.86	46.57	53.54	53.42	54.58	54.05	53.78	54.27
	Se	2.55	1.13	1.02	1.18	2.58	2.67	2.09	2.64	2.18	2.51
	I	0.35	0.61	0.96	0.24	0.36	0.85	0.16	0.42	0.31	0.46
n-Bi ₁₂ Te _{2.7} Se _{0.3}	Bi	39.62	46.24	46.81	47.39	42.94	43.01	42.74	42.48	41.02	41.68
	Te	54.44	46.16	48.06	48.77	51.72	51.01	51.43	52.39	53.78	52.63
	Se	5.94	7.43	5.08	4.3	5.31	5.98	5.83	5.08	5.17	5.69

Table 4.2 Composition analysis of films deposited at 350°C using energy dispersive spectroscopy.

Films Deposited on mica	Substrate deposition temp., °C	Seebeck coeff.($\mu\text{V/K}$)	Hall Effect Measurements		
			Resistivity, $\rho(\text{ohm-cm})$	Hall Mob. (cm^2/Vs)	Car. Conc. (/cc)
p- $\text{Bi}_{0.5}\text{Sb}_{1.5}\text{Te}_3$	300	86.64	1.04×10^{-2}	26.32	3.31×10^{18}
	350	37.74	2.58×10^{-2}	15.45	1.56×10^{19}
	400	49.76	8.01×10^{-3}	22.84	3.41×10^{19}
	450	49.00	3.9×10^{-2}	20.09	8.59×10^{18}
	500	34.65	1.16×10^{-2}	28.89	1.87×10^{19}
n- $\text{Bi}_2\text{Se}_{2.7}\text{Te}_{0.3}$	300	-31.10	1.69×10^{-3}	27.22	1.38×10^{20}
	350	-53.47	1.71×10^{-3}	35.37	1.21×10^{20}
	400	-45.04	2.85×10^{-3}	24.97	9.86×10^{19}
n- $(\text{Bi}_2\text{Te}_3)_{90}(\text{Sb}_2\text{Te}_3)_8$ (SbI_3 doped)	300	-30.80	1.39×10^{-3}	14.43	3.24×10^{19}
	350	-74.15	5.06×10^{-3}	40.42	2.63×10^{19}
	400	-49.13	5.03×10^{-3}	38.34	3.61×10^{19}

Table 4.4.1 Thermopower and Hall-Mobility experimental data obtained on films deposited on mica substrates.

Films deposited on AlN		Substrate deposition temp., °C	Seebeck coeff. ($\mu\text{V/K}$)	Hall Effect Measurements		
				Resistivity, $\rho(\text{ohm-cm})$	Hall Mob. (cm^2/Vs)	Car. Conc. (/cc)
$\text{Bi}_{0.5}\text{Sb}_{1.5}\text{Te}_3$ films	AlN/Si(100)	300	104.51	1.79×10^{-2}	29.07	9.89×10^{18}
		350	142.20	1.94×10^{-2}	35.33	1.02×10^{19}
	AlN/Si(111)	300	96.37	1.86×10^{-2}	15.48	4.46×10^{19}
		350	124.34	2.05×10^{-2}	19.41	1.28×10^{19}
n- $\text{Bi}_2\text{Se}_{2.7}\text{Te}_{0.3}$	AlN/Si(100)	300	-77.52	3.41×10^{-3}	41.37	1.39×10^{20}
		350	-54.89	1.86×10^{-3}	33.98	2.15×10^{20}
	AlN/Si(111)	300	-43.71	1.26×10^{-3}	24.63	1.78×10^{20}
		350	-28.91	1.27×10^{-3}	13.74	3.59×10^{20}
n- $(\text{Bi}_2\text{Te}_3)_{90}(\text{Sb}_2\text{Te}_3)_8(\text{Sb}_2\text{Se}_3)_2$ (Sb ₁₃ doped)	AlN/Si(100)	300	-147.64	9.43×10^{-3}	65.37	1.3×10^{19}
		350	-104.15	5.06×10^{-3}	40.42	5.63×10^{19}
	AlN/Si(111)	300	-62.94	3.69×10^{-3}	36.29	4.43×10^{19}
		350	-154.69	9.48×10^{-3}	68.84	9.58×10^{18}

Table 4.4.2 Thermopower and Hall-Mobility experimental data obtained on films deposited on aluminum nitride substrates.

Films deposited on AlN/ Si(1 0 0)	Seebeck coeff. ($\mu\text{V/K}$)	Resistivity, $\rho(\text{ohm-cm})$
$\text{Bi}_{0.5}\text{Sb}_{1.5}\text{Te}_3$	138.42	1.13×10^{-2}
$\text{Bi}_2\text{Se}_{2.7}\text{Te}_{0.3}$	-81.32	1.23×10^{-3}
n- $(\text{Bi}_2\text{Te}_3)_{90}(\text{Sb}_2\text{Te}_3)_5(\text{Sb}_2\text{Se}_3)_5$ (0.13 % wt SbI_3 doped)	-166.37	1.17×10^{-2}

Table 4.4.3 Thermopower values obtained on films deposited on AlN/ Si (100) substrates at better pre-deposition vacuum.

Parameter	Substrate	n-type	p-type
Highest α ($\mu\text{V/K}$)	Mica	-74.15	49.76
	AlN/Si(100)	-166.37	142.2
	AlN/Si(111)	-154.69	124.34
Highest μ ($\text{cm}^2/\text{V}\cdot\text{sec}$)	Mica	40.42	28.89
	AlN/Si(100)	65.37	35.33
	AlN/Si(111)	68.84	19.41
Highest carrier concentration (cm^{-3})	Mica	1.38×10^{20}	3.41×10^{19}
	AlN/Si(100)	2.15×10^{20}	1.02×10^{19}
	AlN/Si(111)	3.59×10^{20}	4.46×10^{19}

Table 5.4.1 Summary of best values of the films in terms of the highest Seebeck values, highest mobility and highest carrier concentration.

Films	α ($\mu\text{V/K}$)	$\rho(\Omega\text{-cm})$	κ_{assumed} (W/cmK)	ZT
p-type on mica	86.64	0.0104	0.0014	0.15
p-type on AlN	142.2	0.0194	0.0014	0.22
n-type on mica	-53.47	0.00171	0.0012	0.42
n-type on AlN	-154.69	0.00948	0.0012	0.63

Table 5.4.2 Best values of ZT obtained on n-type and p-type films.

Target composition	α ($\mu\text{V/K}$)	$\rho(\Omega\text{-cm})$	κ (W/cm K)	ZT
p-- $\text{Bi}_{0.5}\text{Sb}_{1.5}\text{Te}_3$	232.2	0.0017	0.014	0.68
n- $(\text{Bi}_2\text{Te}_3)_{90}(\text{Sb}_2\text{Te}_3)_5(\text{Sb}_2\text{Se}_3)_5$ (SbI_3 doped)	-206	0.0011	0.012	0.96

Table 5.4.3 Values of ZT reported on n-type and p-type target materials.

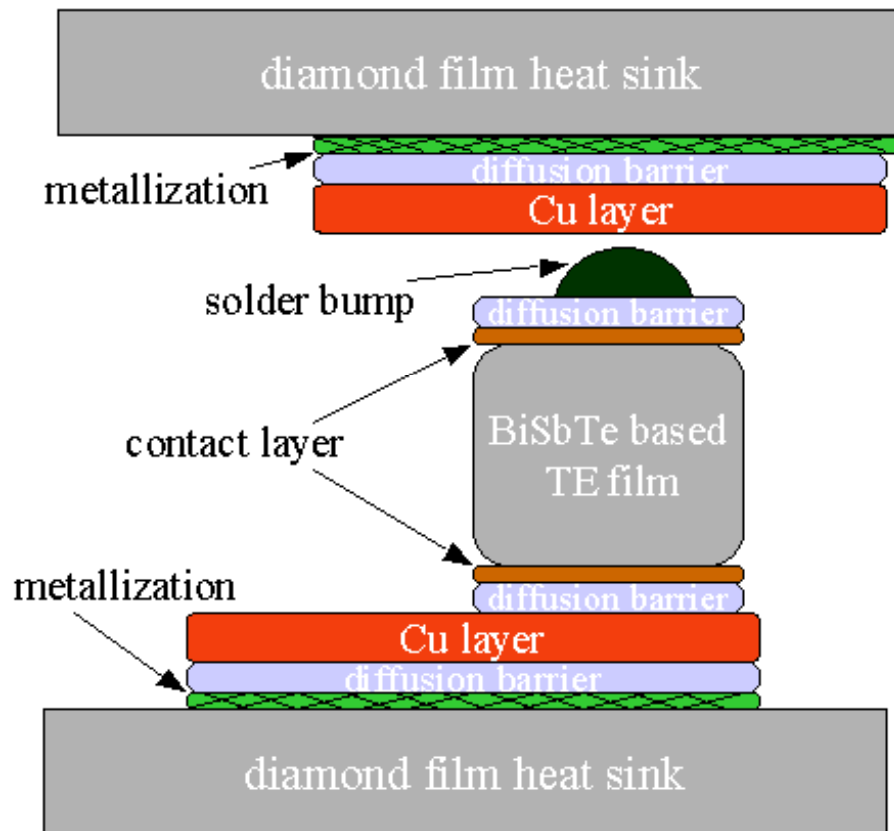


Fig. 1.1 Schematic showing thin film thermoelectric device integrated with diamond substrates. The proposed metallization and bonding scheme can also be seen.

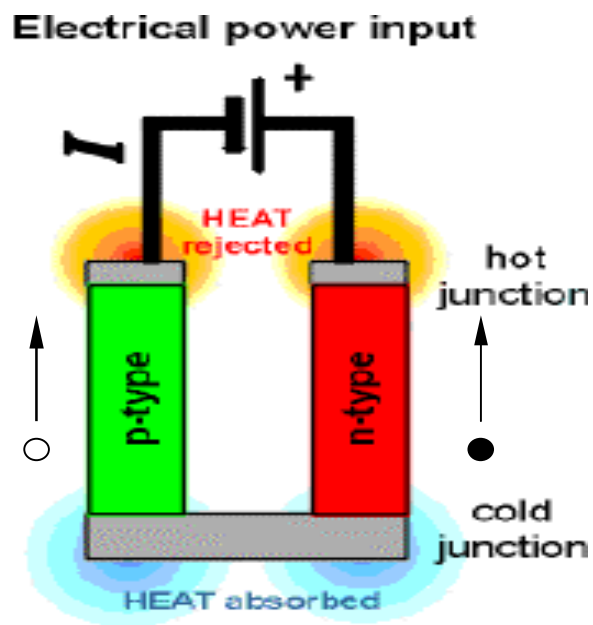


Fig. 2.1.1 Schematic showing a single thermocouple that constitutes a simple thermoelectric cooling sub-assembly. The labels p (positive) and n (negative) refer to the sign of the charge carriers in each leg, where as filled circles correspond to electrons and open circles correspond to holes.

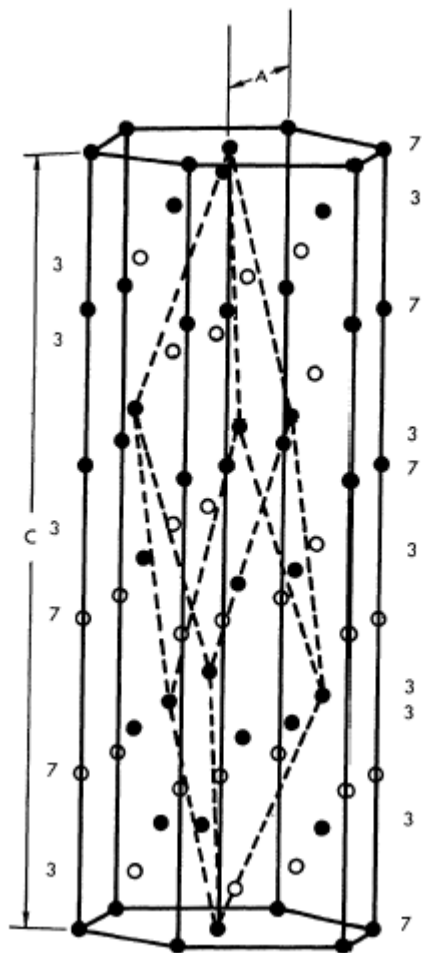


Fig. 2.2.1 Crystal structure of the Bi_2Te_3 unit cell.

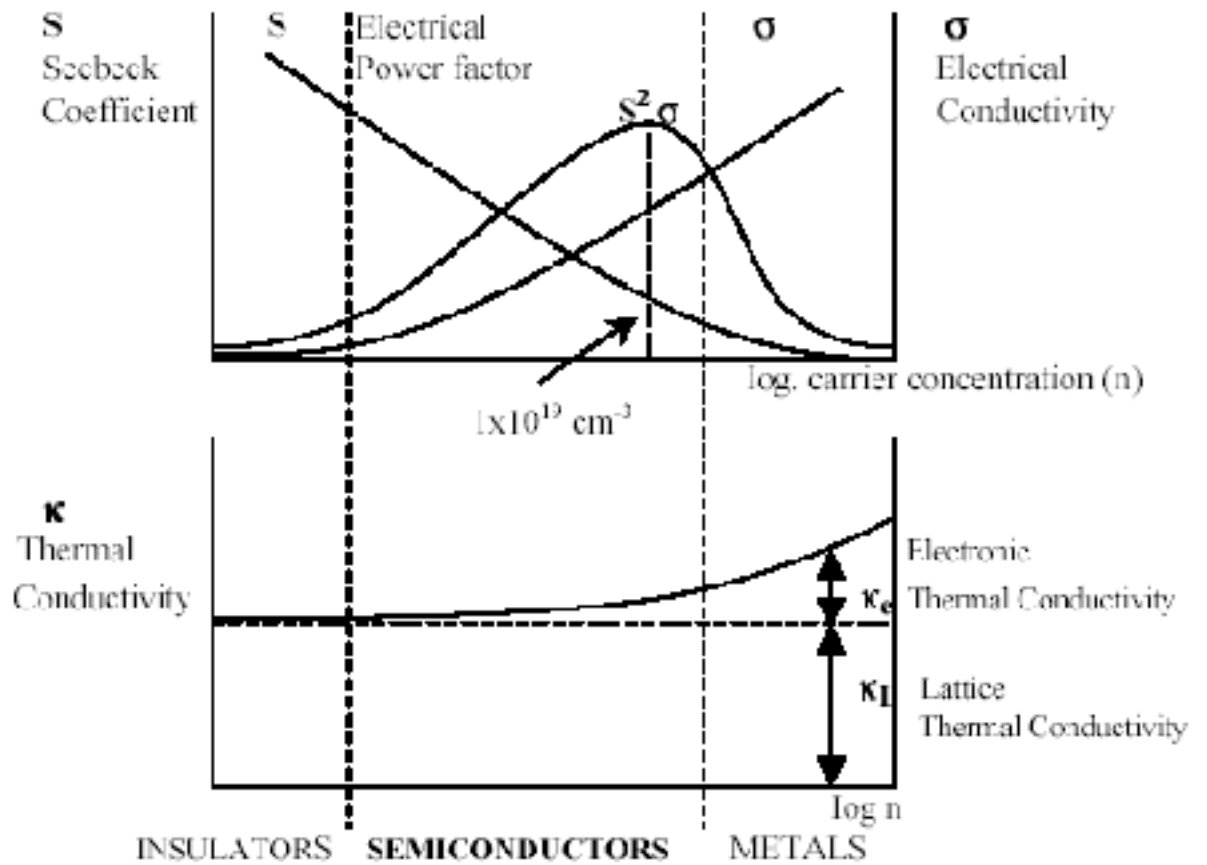


Fig. 2.2.2 Representation of the dependence of thermoelectric power S , electrical conductivity σ , thermal conductivity K , and the product of $S^2\sigma$ on the extent of extrinsic charge carriers.

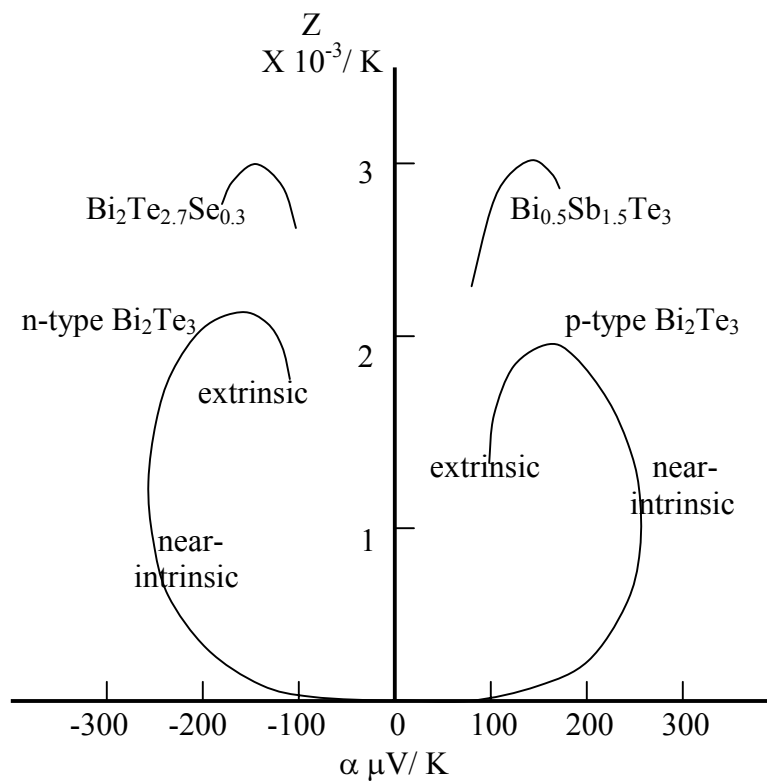


Fig. 2.2.3 Plot of figure of merit, Z as a function of Seebeck coefficient for Bi_2Te_3 at 300 K. The upper curves illustrate the higher values of Z possible with ternary alloys.

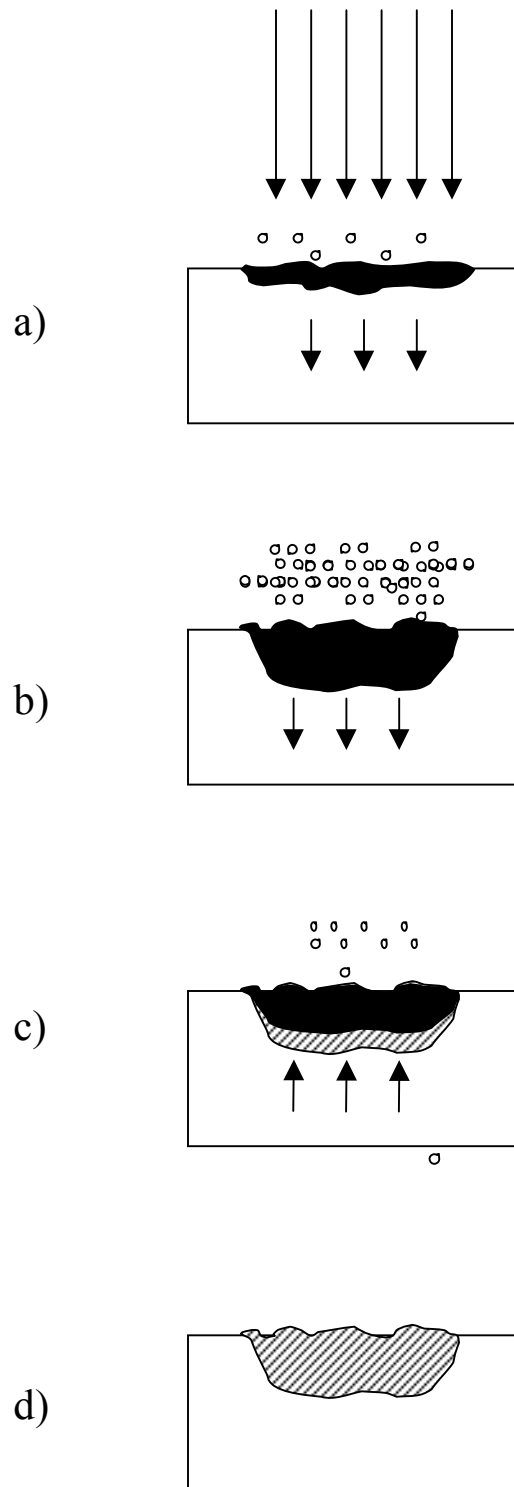


Fig. 2.3.1 Illustration of basic thermal cycle induced by laser pulsing. (a) absorption of laser plume and beginning of melting and vaporization, shaded area indicates molten material, arrows indicate motion of solid- liquid interface (b) advancing of melt front into solid, accompanied by vaporization (c) melt front receding, cross hatched region indicates re-solidification (d) complete re-solidification, frozen capillary waves alter topography.

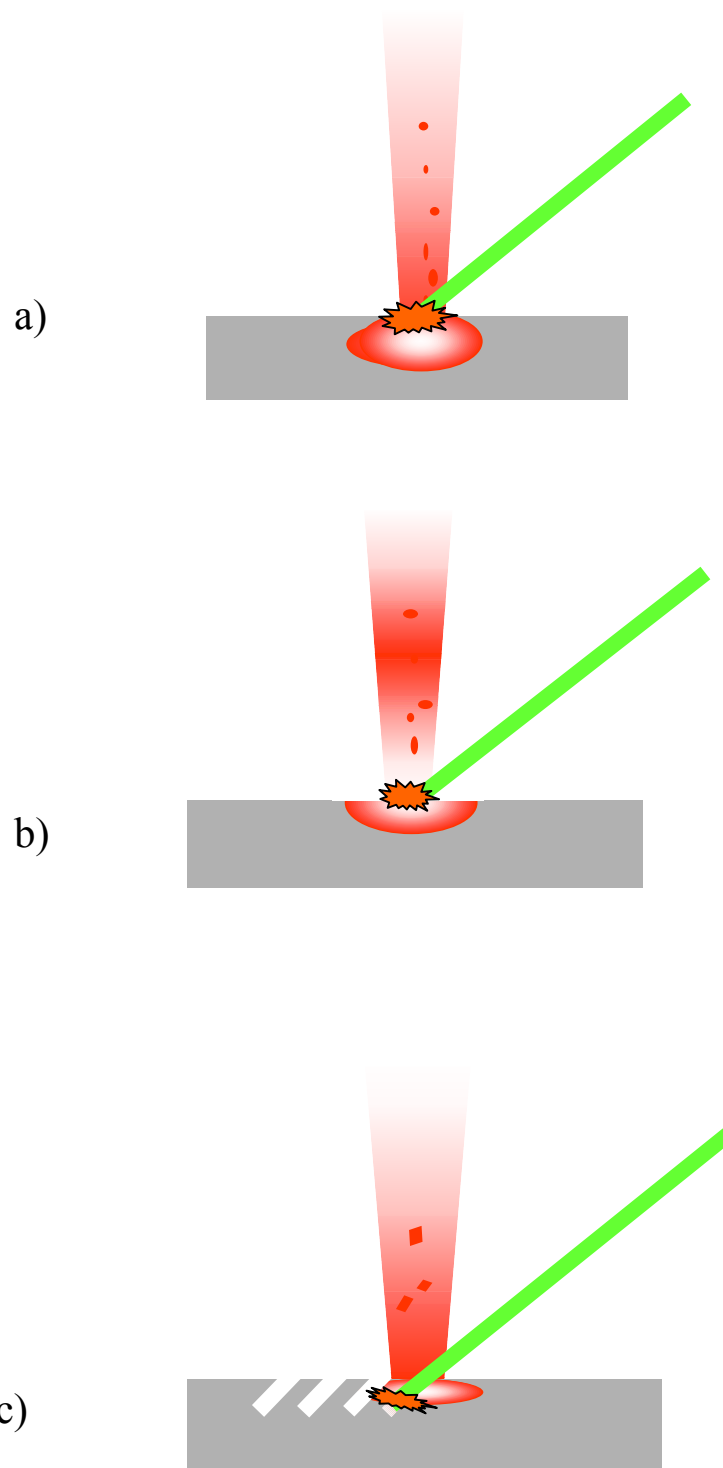


Fig. 2.3.2 Schematic illustrating the various mechanisms responsible for splashing. (a) Subsurface boiling, (b) Shock wave recoil, and (c) Exfoliation.

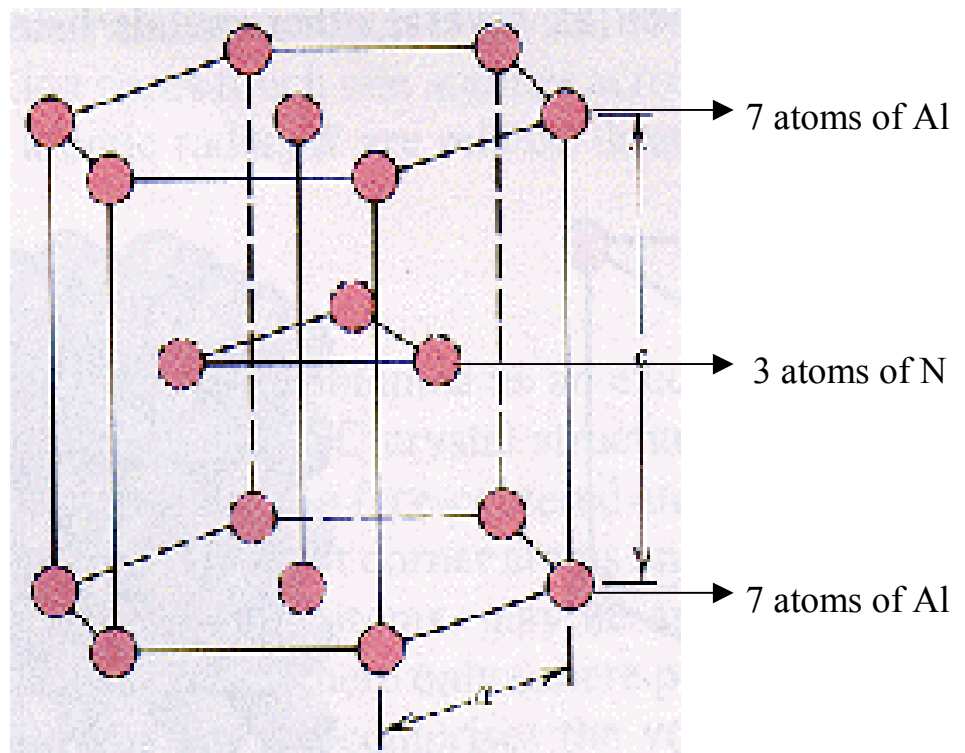


Fig. 2.5.1 Crystal structure of the AlN unit cell.

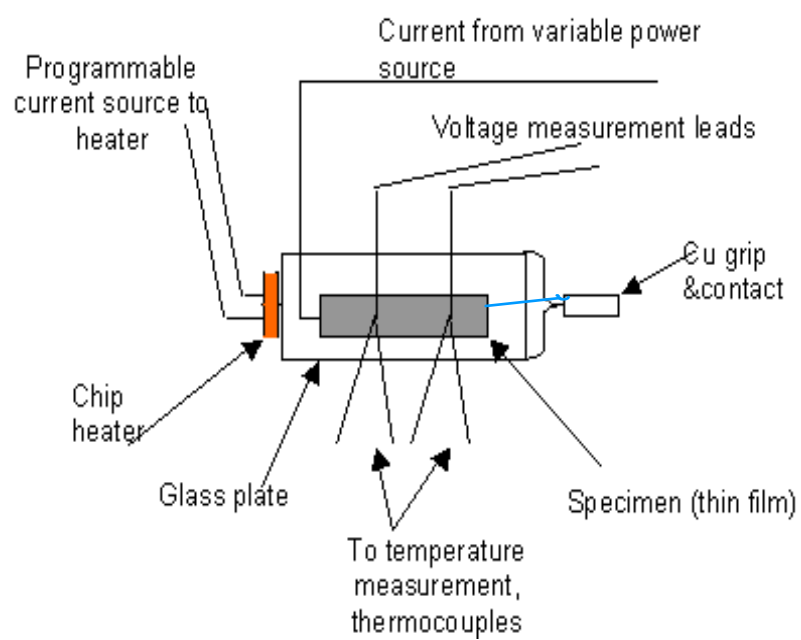


Fig. 2.6.6.1 Specimen support plate used for measurement of Seebeck coefficient.

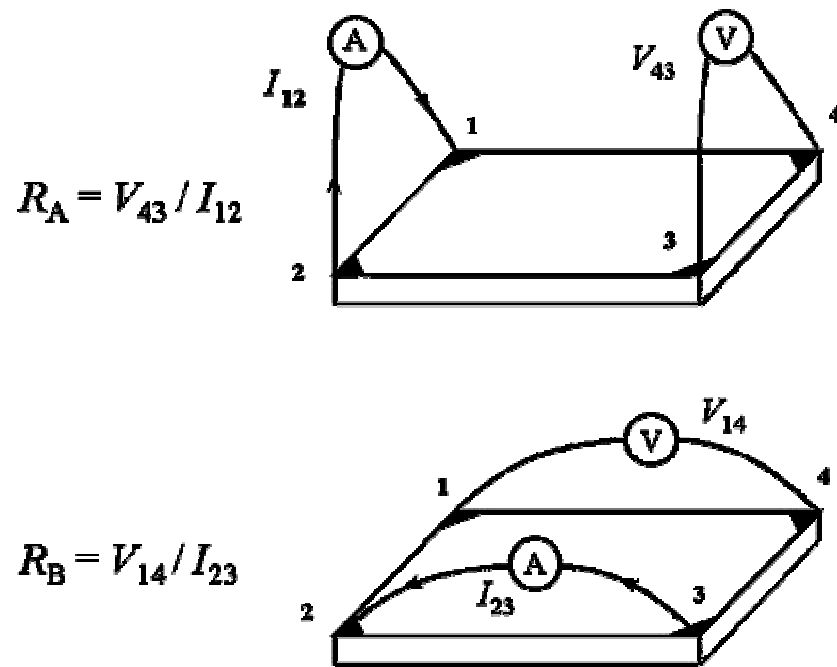


Fig. 2.6.7.1 Specimen configuration used for Van-der-Pauw technique and Hall effect.

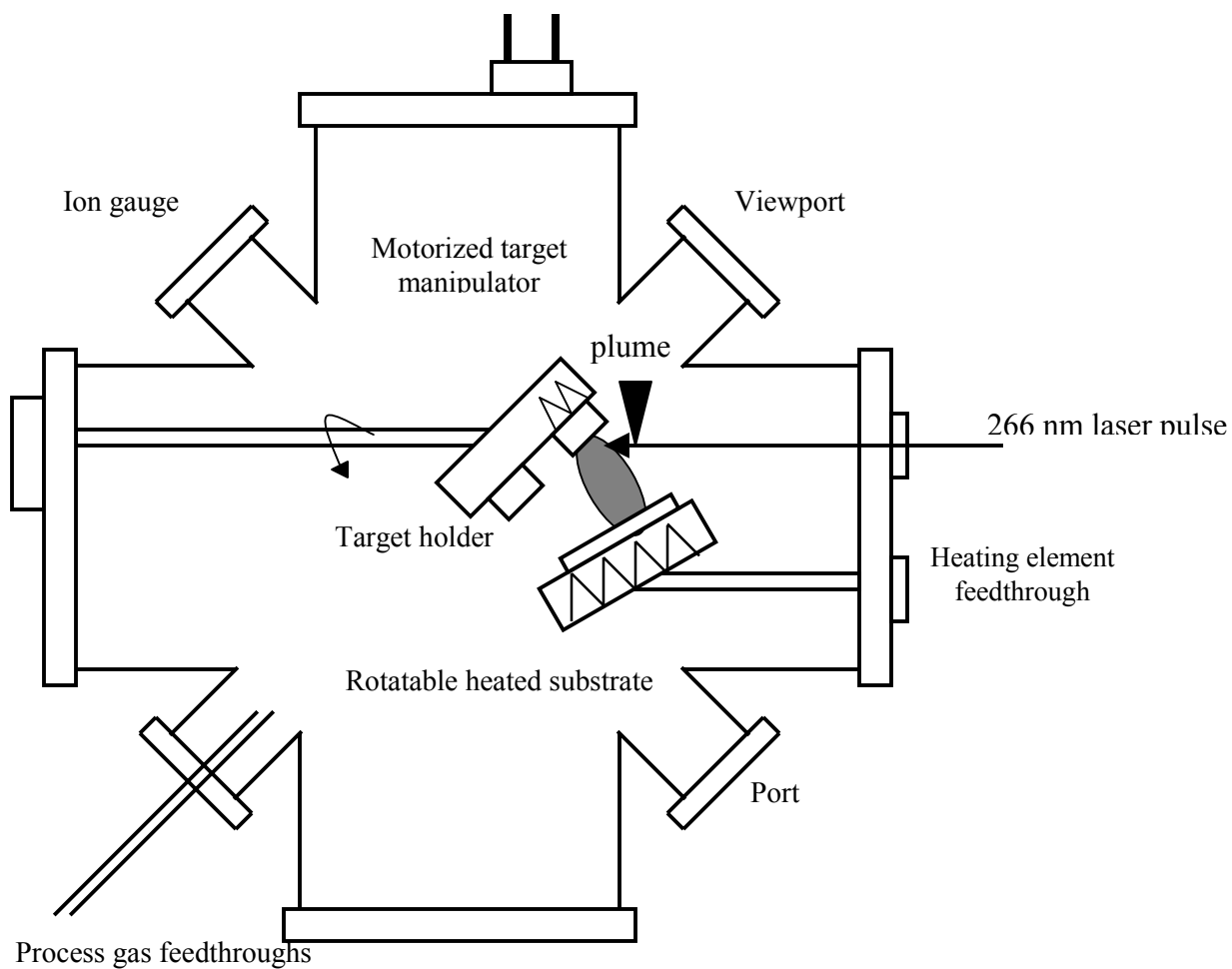


Fig. 3.3.1 Schematic of PLD experimental set-up used in this study.

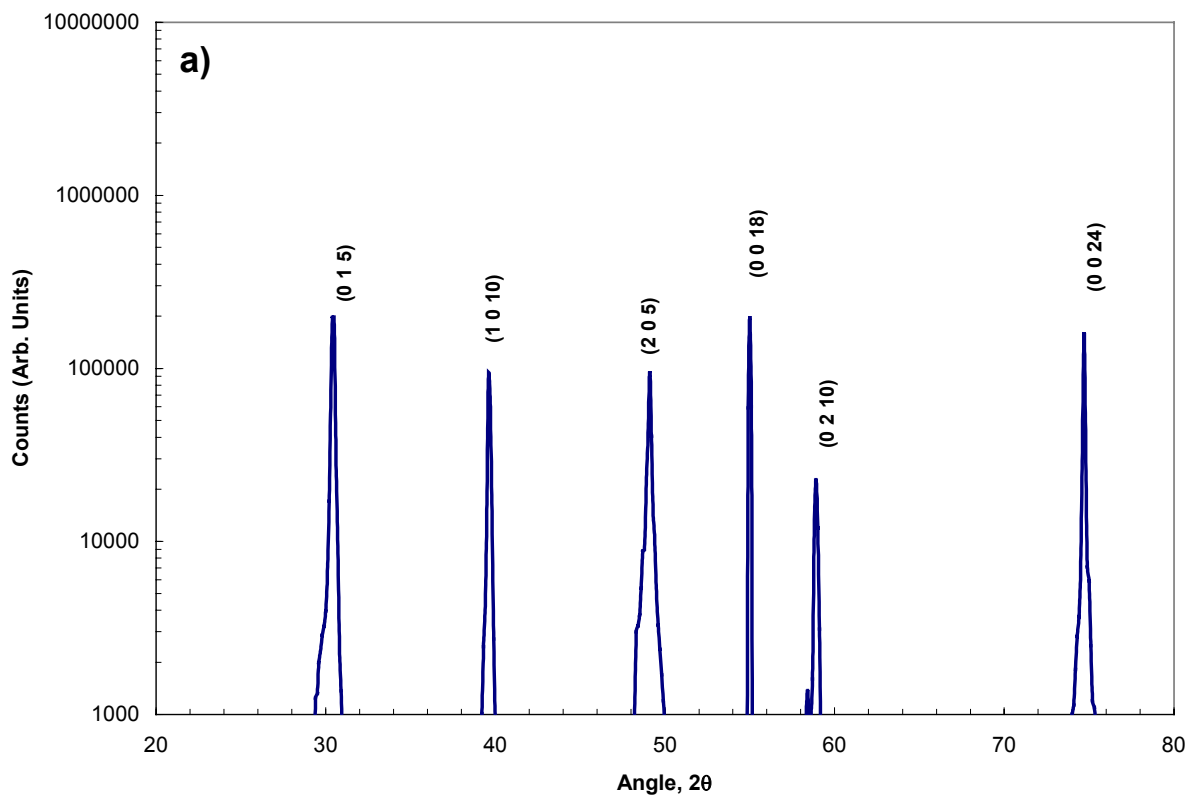


Fig. 4.1.1 (a) θ - 2θ x-ray diffraction scan obtained on $\text{Bi}_{0.5}\text{Sb}_{1.5}\text{Te}_3$ ingot used as a target material.

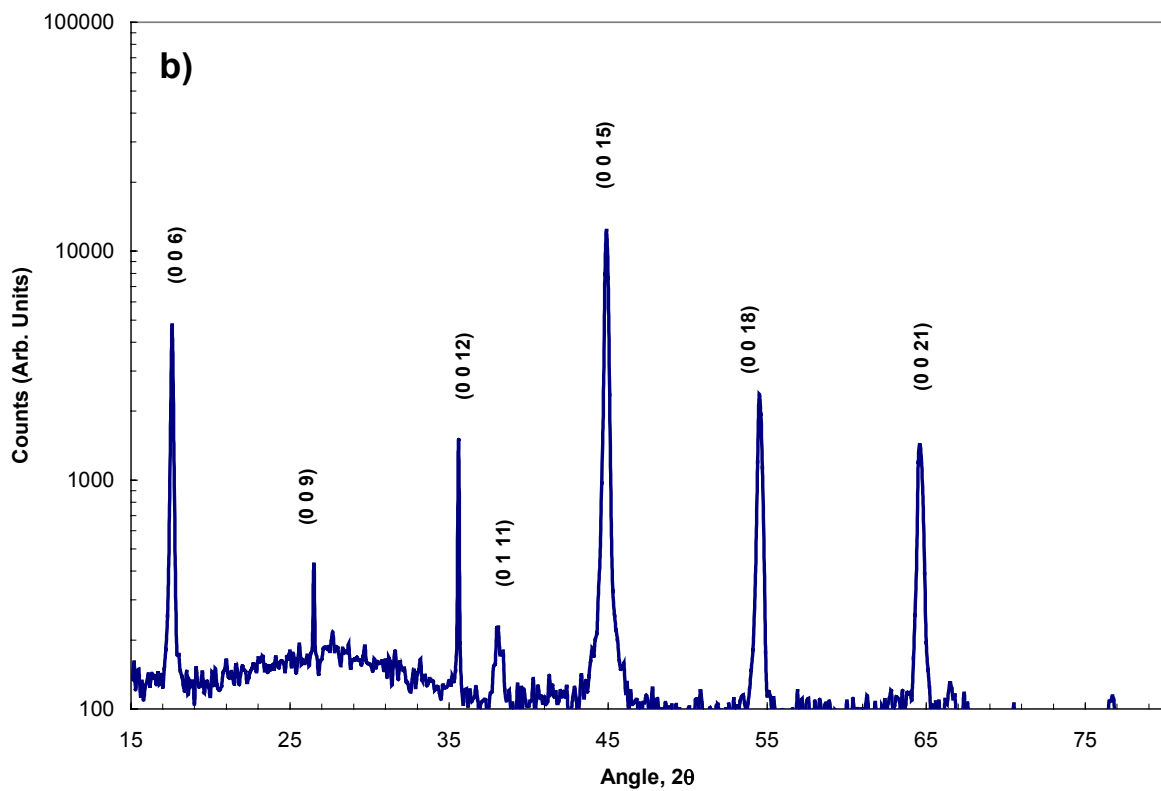


Fig. 4.1.1 (b) θ - 2θ x-ray diffraction scan obtained on $\text{Bi}_2\text{Te}_{2.7}\text{Se}_{0.3}$ ingot used as a target material.

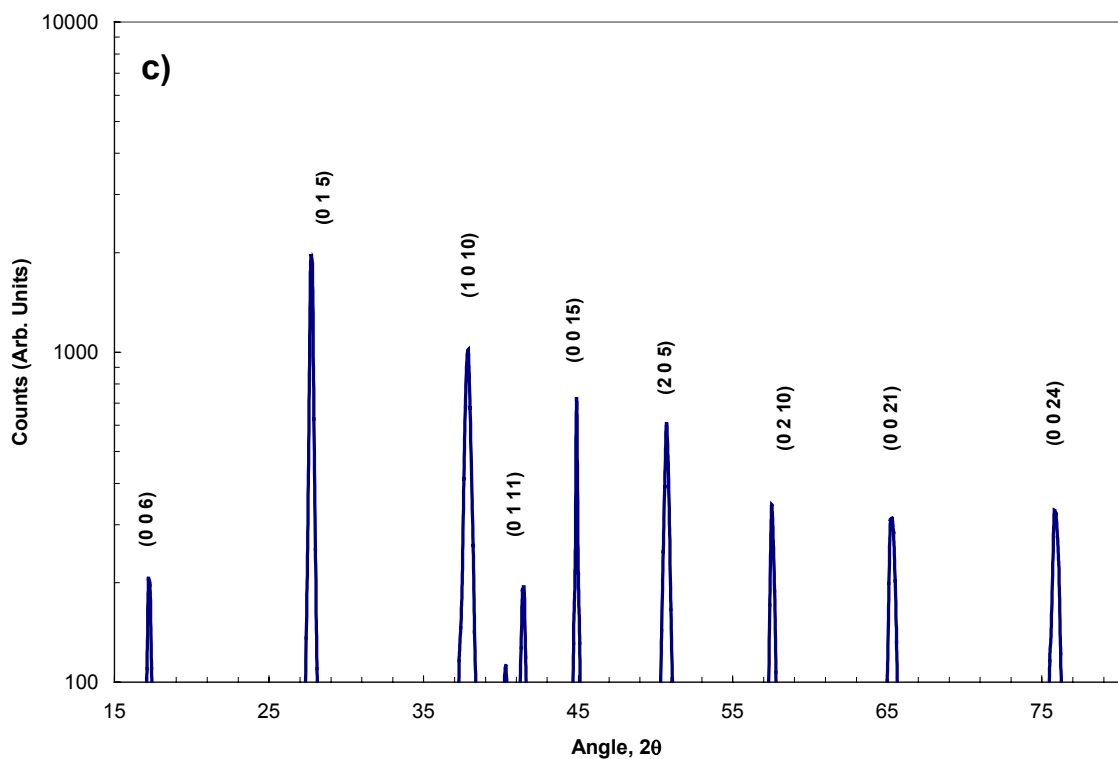


Fig. 4.1.1 (c) θ - 2θ x-ray diffraction scan obtained on $(\text{Bi}_2\text{Te}_3)_{90}(\text{Sb}_2\text{Te}_3)_{10}(\text{Sb}_2\text{Se}_3)_{10}$ (+ 0.13 % wt SbI_3) ingot used as a target material.

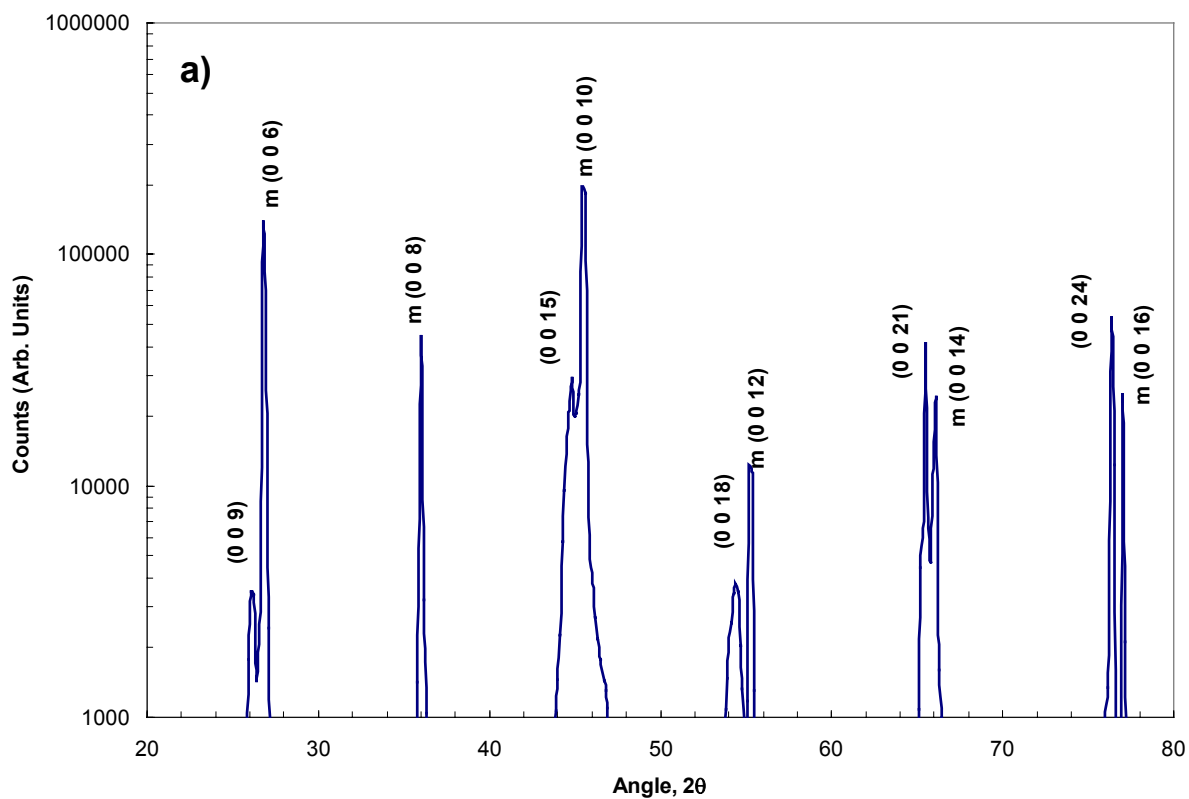


Fig. 4.1.2 (a) θ - 2θ x-ray diffraction scan obtained on $\text{Bi}_{0.5}\text{Sb}_{1.5}\text{Te}_3$ thin films deposited on mica substrates.

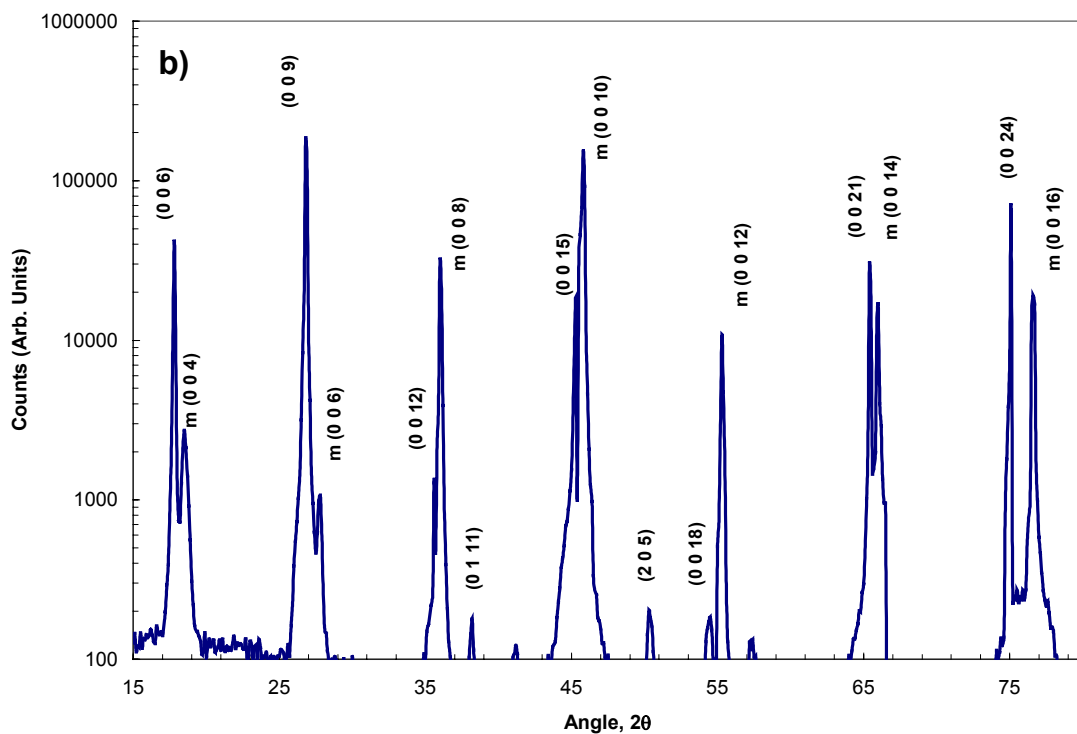


Fig. 4.1.2 (b) θ -2 θ x-ray diffraction scan obtained on $\text{Bi}_2\text{Te}_{2.7}\text{Se}_{0.3}$ thin films deposited on mica substrates.

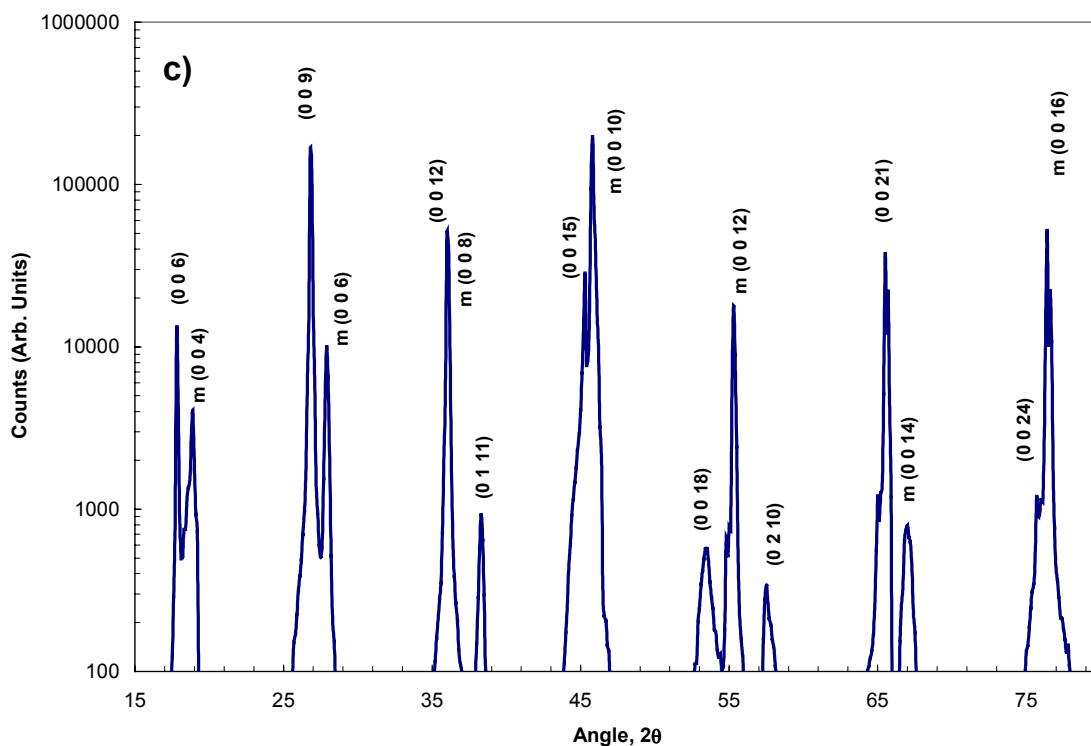


Fig. 4.1.2 (c) θ -2 θ x-ray diffraction scan obtained on thin films deposited on mica substrates using a $(\text{Bi}_2\text{Te}_3)_{90}(\text{Sb}_2\text{Te}_3)_{10}(\text{Sb}_2\text{Se}_3)_{10} (+ 0.13 \% \text{ wt SbI}_3)$ target.

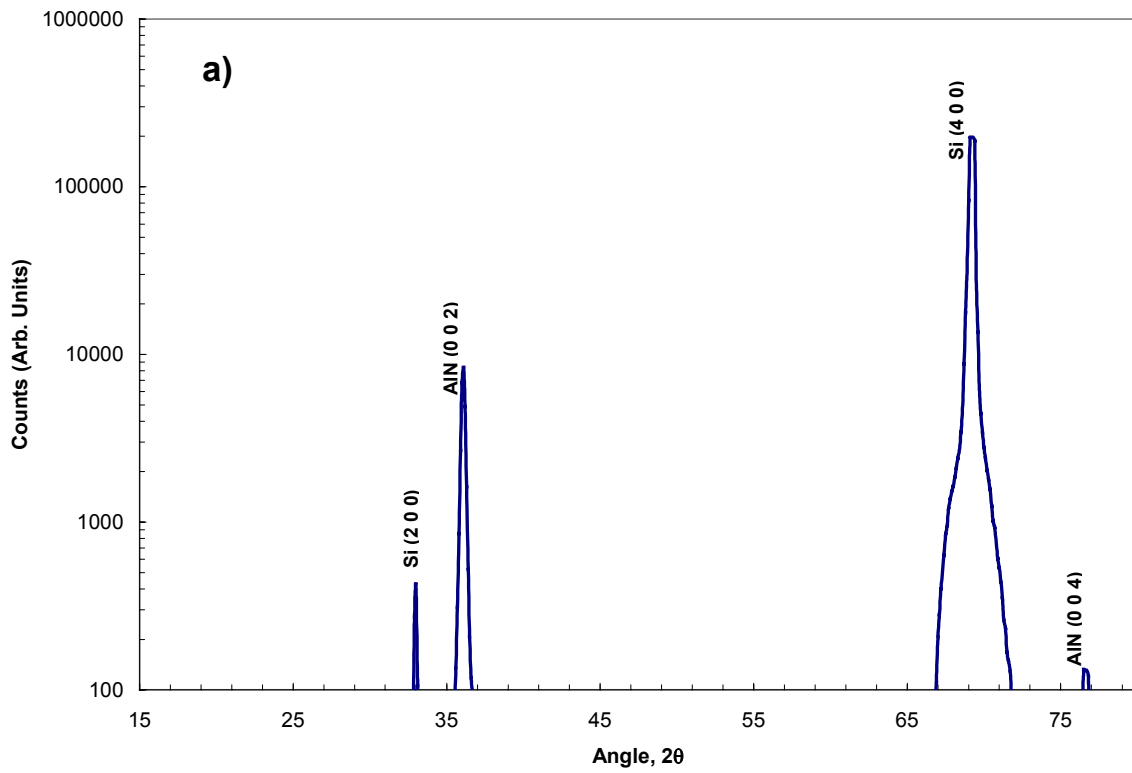


Fig. 4.1.3 (a) θ -2 θ x-ray diffraction scan obtained on AlN thin films deposited on Si(1 0 0) substrates by dc reactive magnetron sputtering.

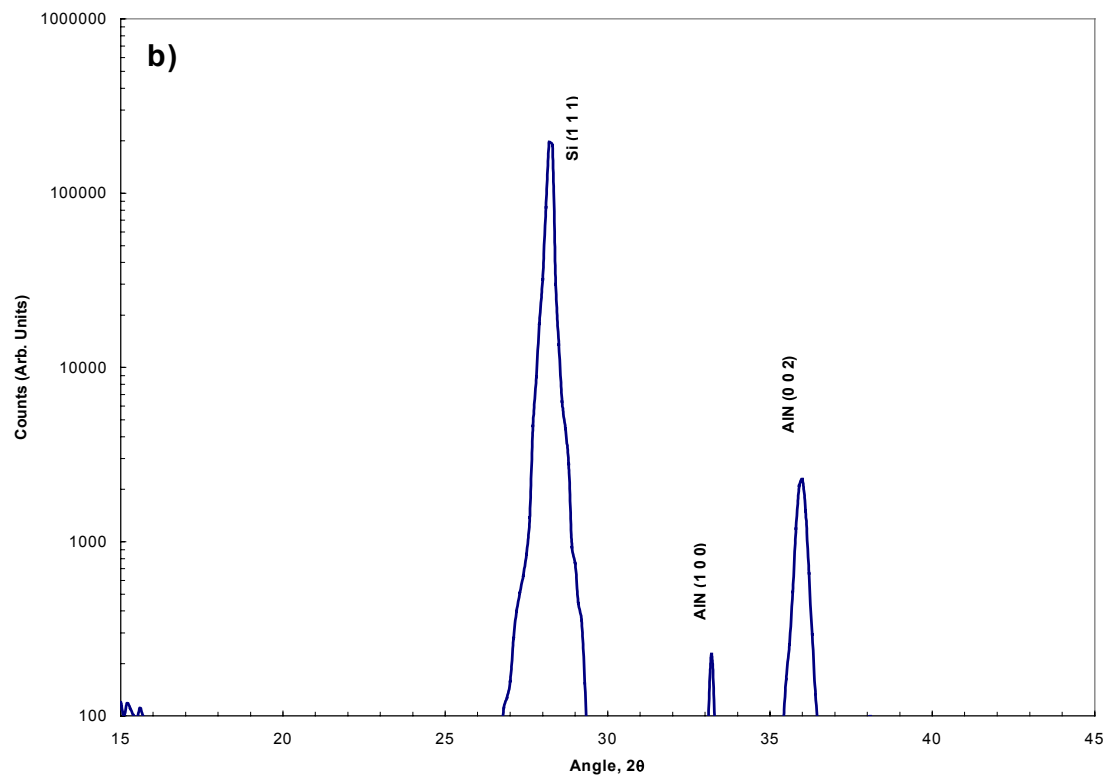


Fig. 4.1.3 (b) θ -2 θ x-ray diffraction scan obtained on AlN thin films deposited on Si(1 1 1) substrates by dc reactive magnetron sputtering.

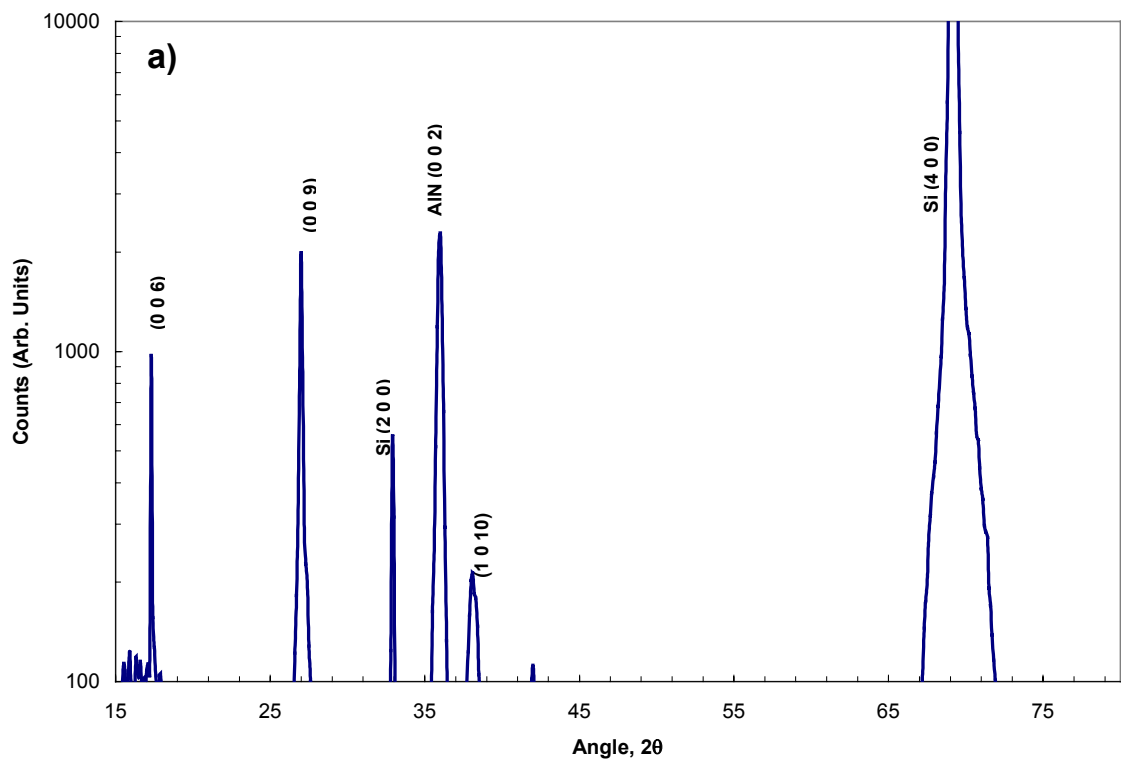


Fig. 4.1.4 (a) θ - 2θ x-ray diffraction scan obtained on thermoelectric thin films deposited on AlN/ Si(1 0 0) substrates.

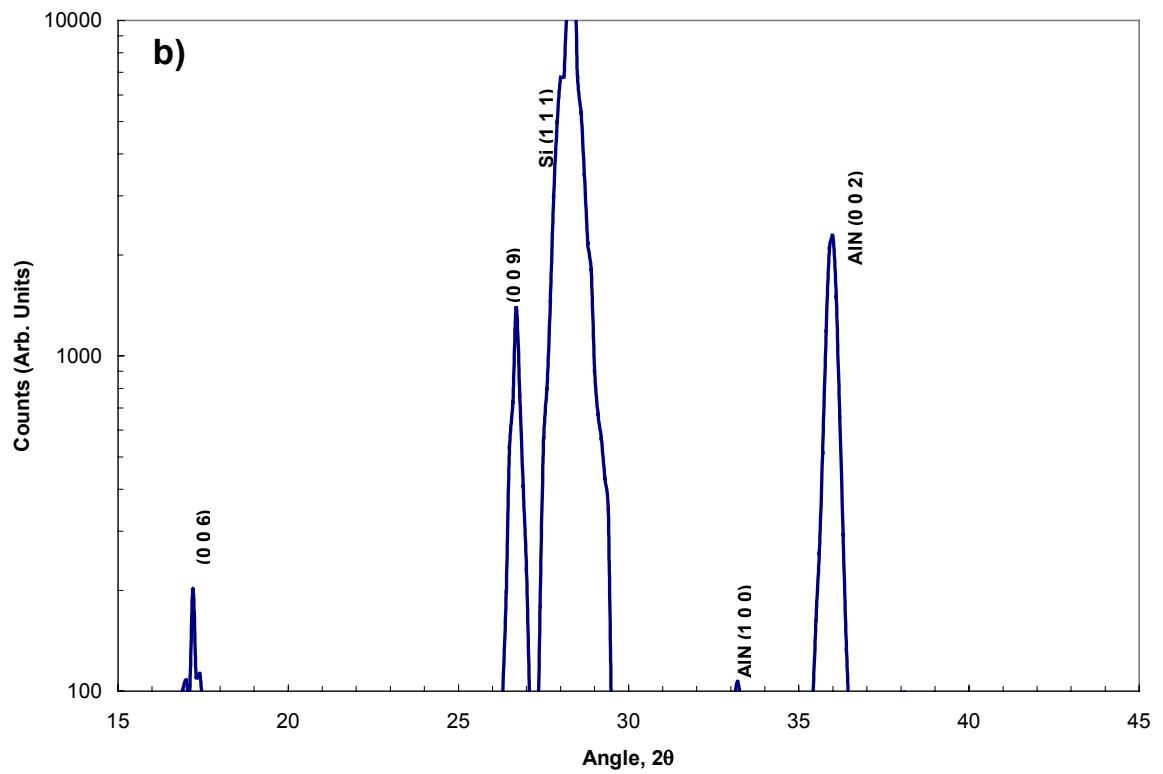


Fig. 4.1.4 (b) θ - 2θ x-ray diffraction scan obtained on thermoelectric thin films deposited on AlN/ Si(1 1 1) substrates.

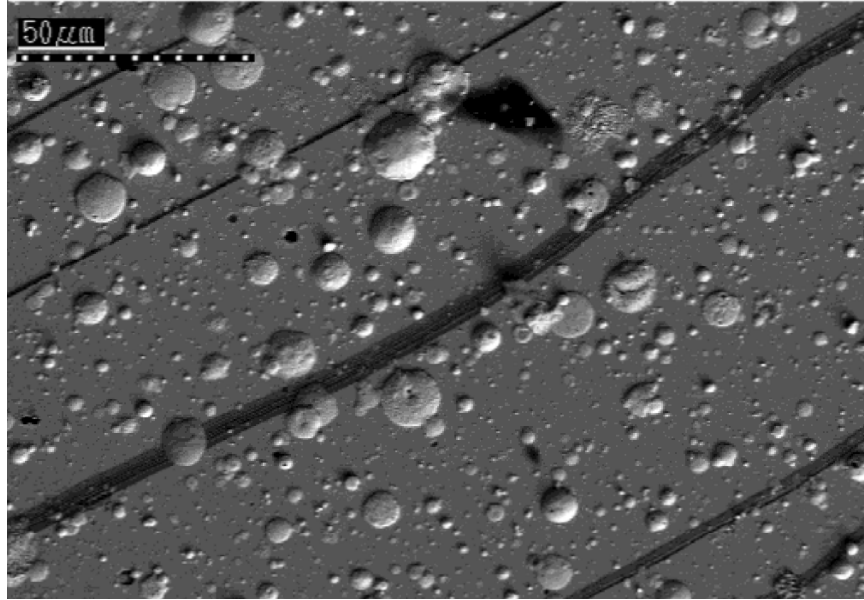


Fig. 4.2.1 SEM micrograph obtained on n-type films deposited on mica substrates using a high incident laser fluence.

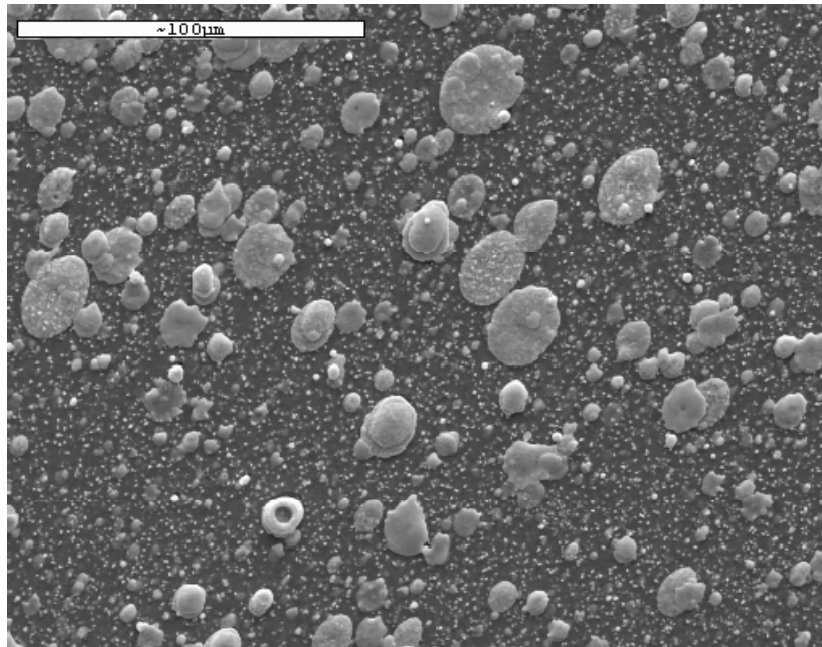


Fig. 4.2.2 SEM micrograph obtained on n-type films deposited on AlN substrates using a high incident laser fluence.

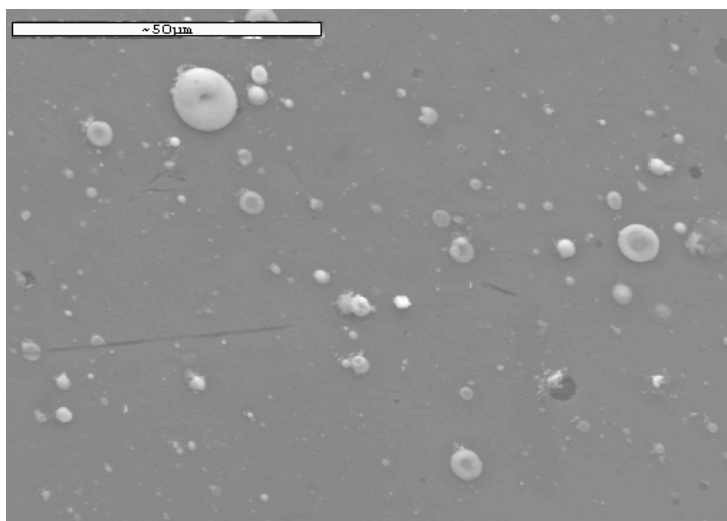


Fig. 4.2.3 SEM micrograph obtained on n-type films deposited on AlN substrates using a lowered incident laser fluence.

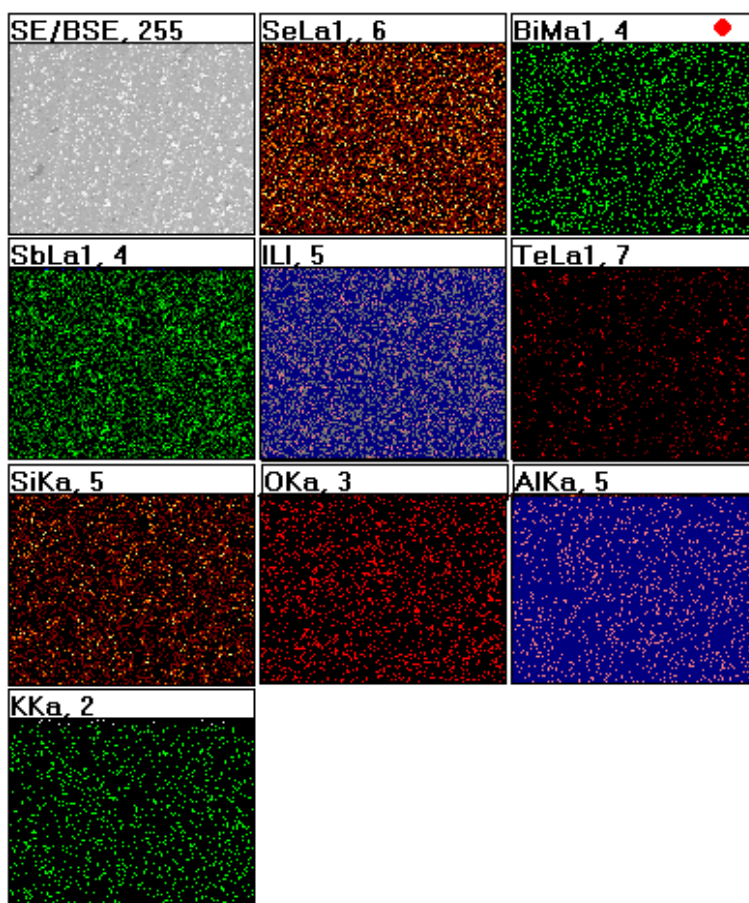


Fig. 4.2.4 X-ray map of micrograph obtained on n-type films deposited from the $(\text{Bi}_2\text{Te}_3)_{90}(\text{Sb}_2\text{Te}_3)_{10}(\text{Sb}_2\text{Se}_3)_{10}$ (with 0.13 wt.% SbI_3) target on mica substrates using a high incident laser fluence at a low magnification.

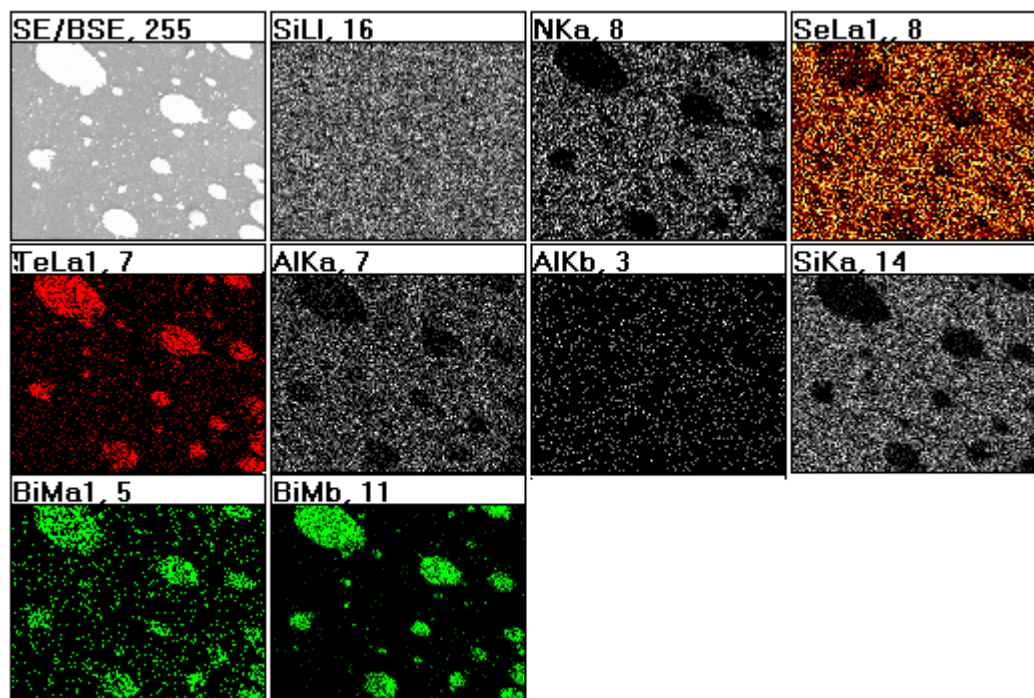


Fig. 4.2.5 X-ray map of micrograph obtained on n-type $\text{Bi}_2\text{Te}_{2.7}\text{Se}_{0.3}$ films deposited on AlN substrates using a high incident laser fluence at a higher magnification.

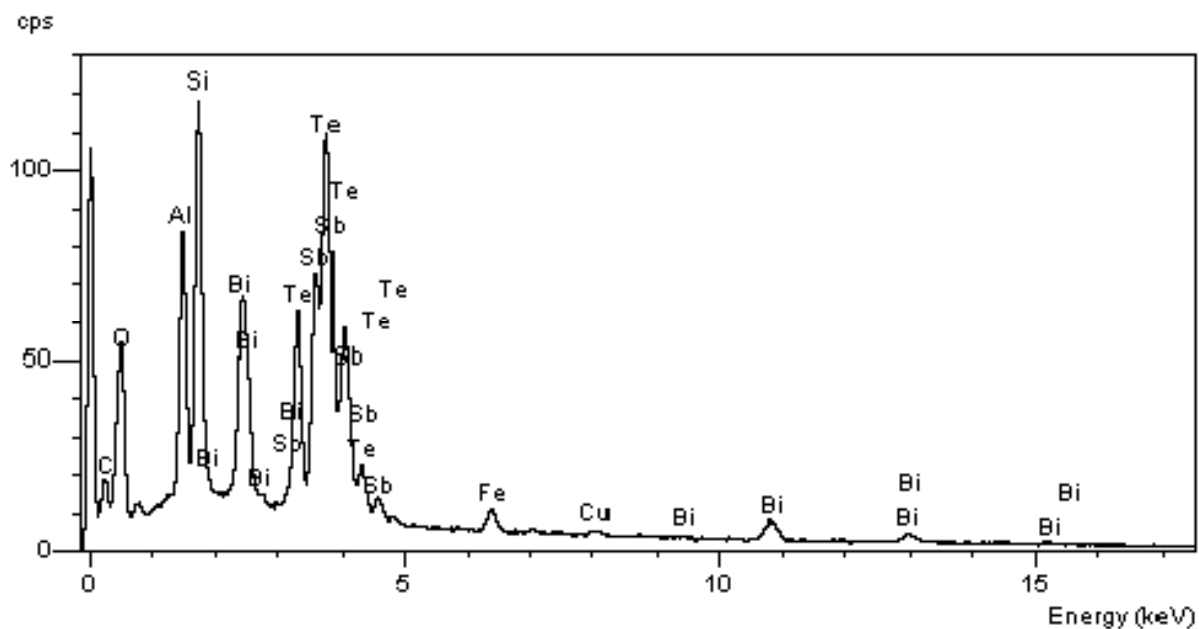


Fig. 4.2.6 EDS spectra obtained on p-type films deposited on mica substrates.

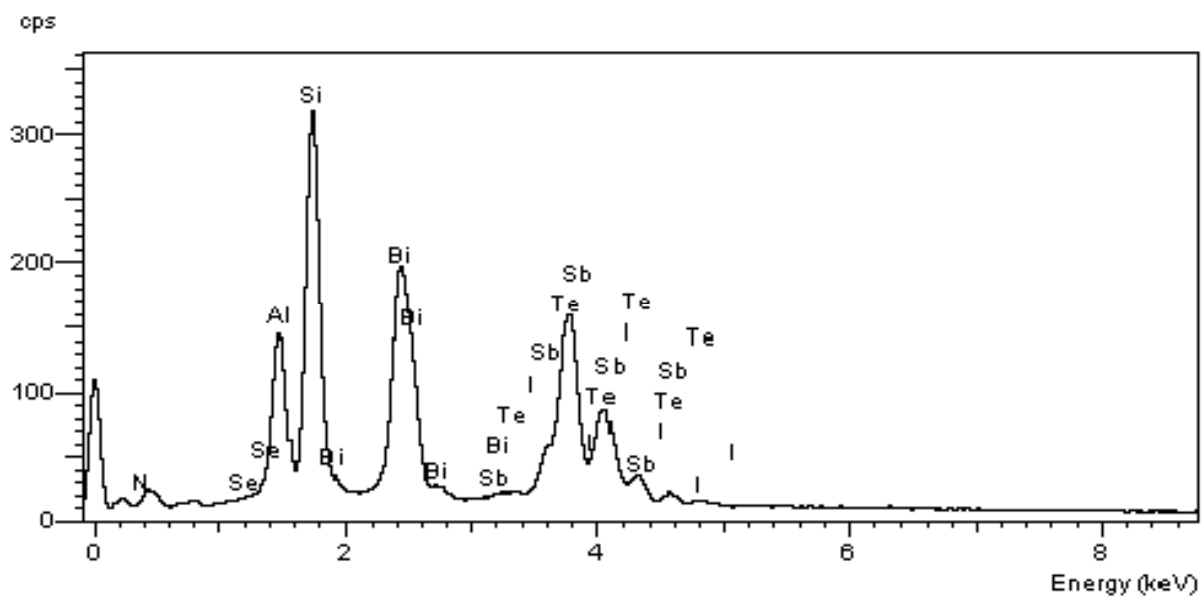


Fig. 4.2.5 EDS spectra obtained on n-type $(\text{Bi}_2\text{Te}_3)_{90}(\text{Sb}_2\text{Te}_3)_{10}(\text{Sb}_2\text{Se}_3)_{10}$ (with 0.13 wt.% SbI_3) films deposited on AlN substrates.

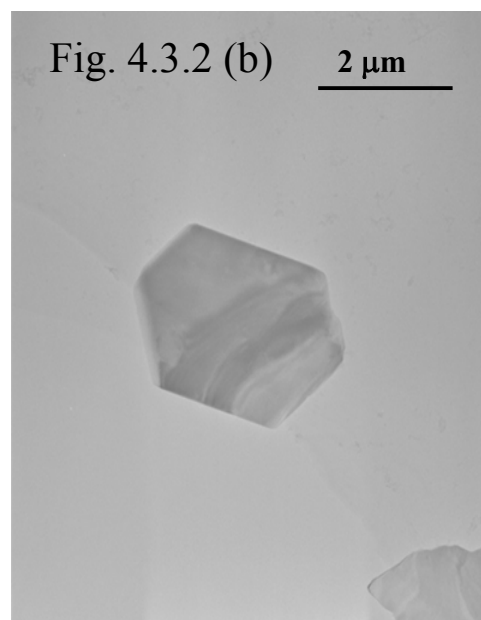
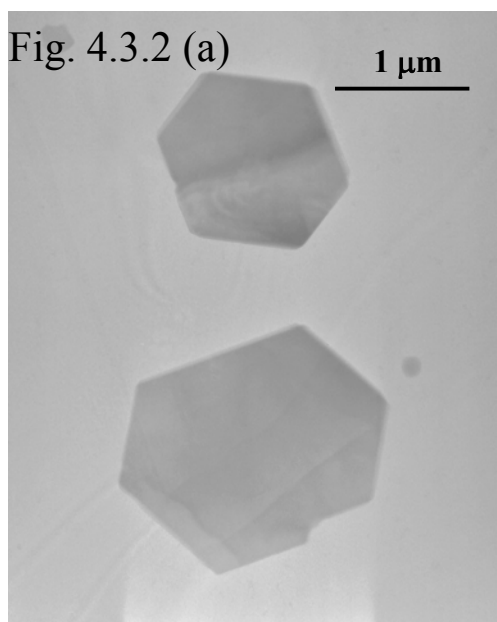
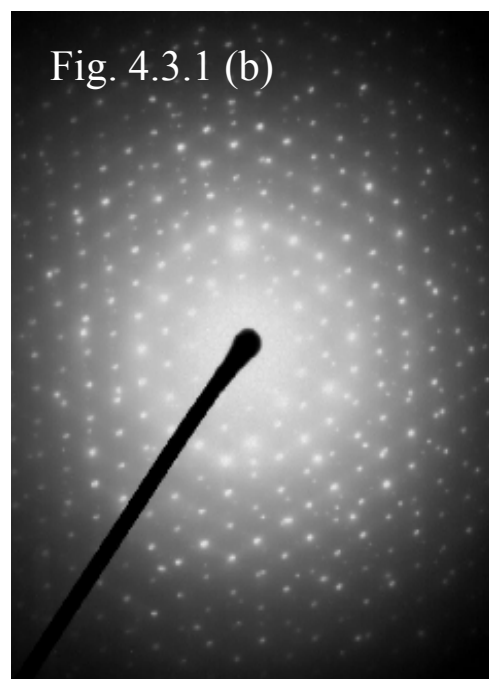
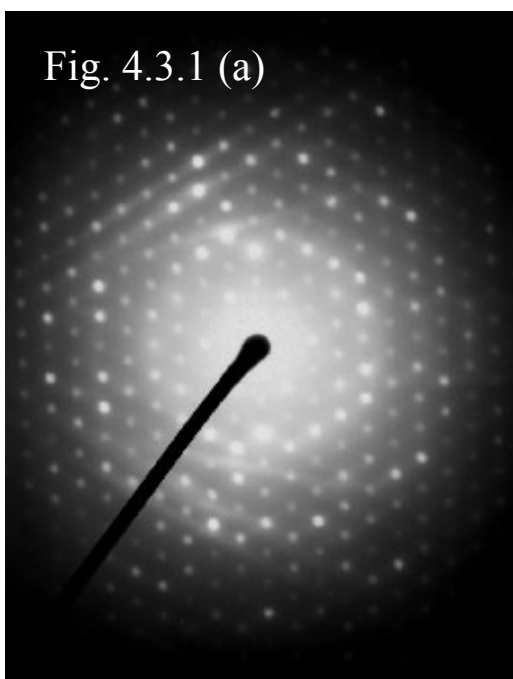


Fig. 4.3.1 (a) Selected Area Diffraction Pattern (SADP) obtained from the mica sheet used as a substrate material. Fig. 4.3.1 (b) SADP obtained on the thermoelectric thin films deposited on mica substrates. Figs. 4.3.2 (a) and (b) Bright field TEM images obtained on thermoelectric thin films illustrating the presence of hexagon shaped crystallites.

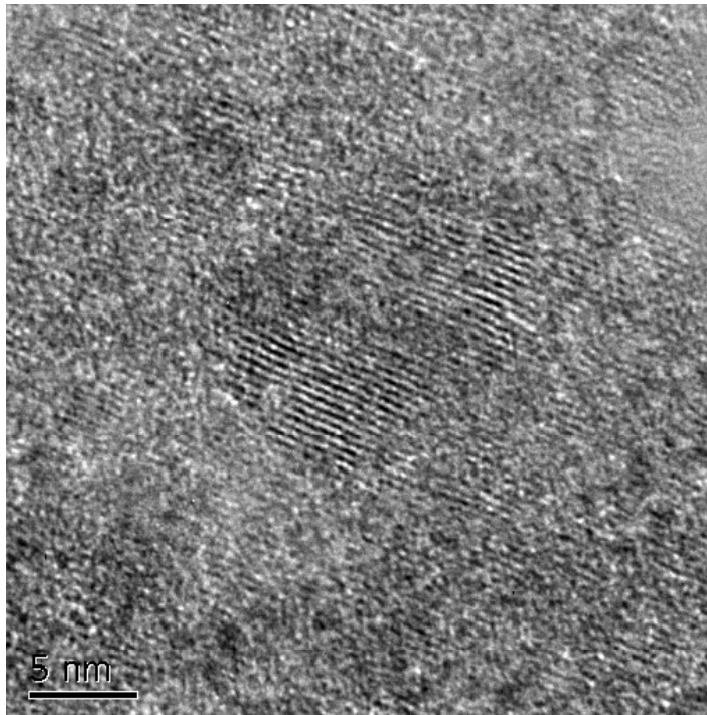


Fig. 4.3.3 High-resolution lattice image obtained on n-type thermoelectric thin films deposited with the aid of a nanofilter.

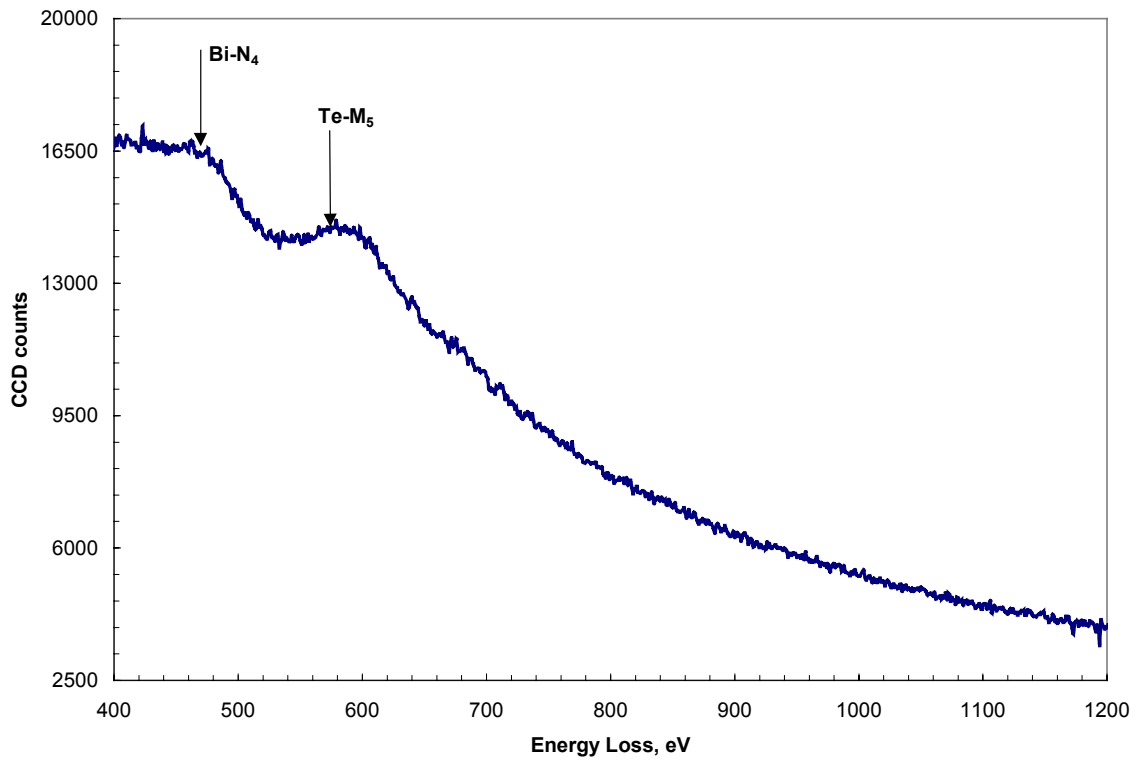


Fig. 4.3.4 Electron energy loss data plot obtained on the nano-structured films shown in fig. 4.3.3.

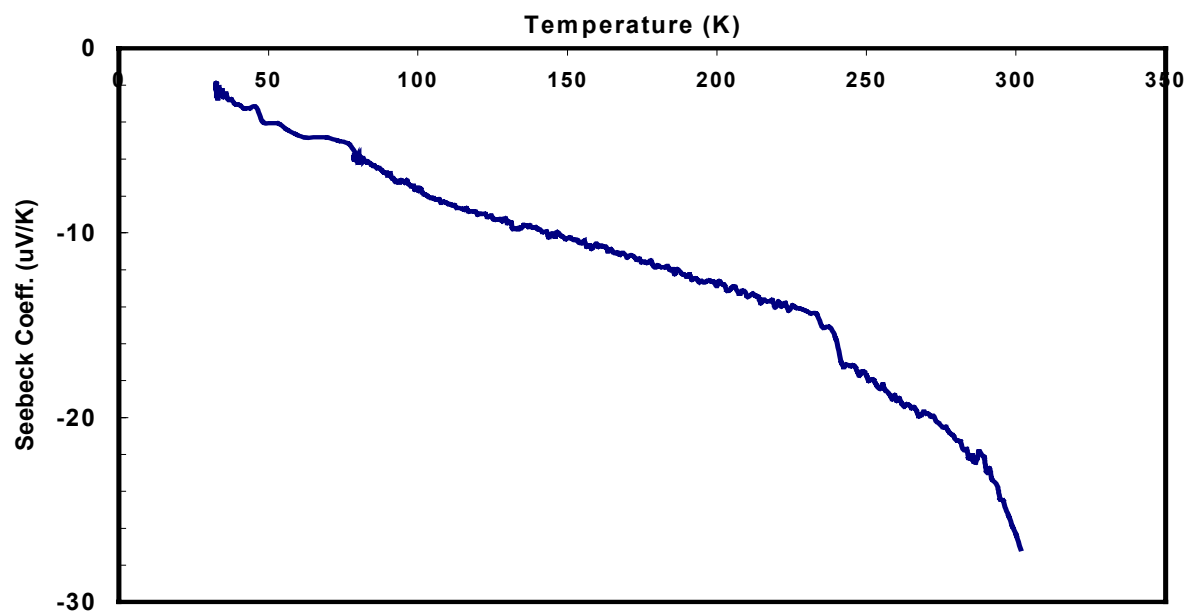


Fig. 4.4.1 Plot of Seebeck coefficient or thermopower as a function of temperature for the n-type films deposited at 300°C

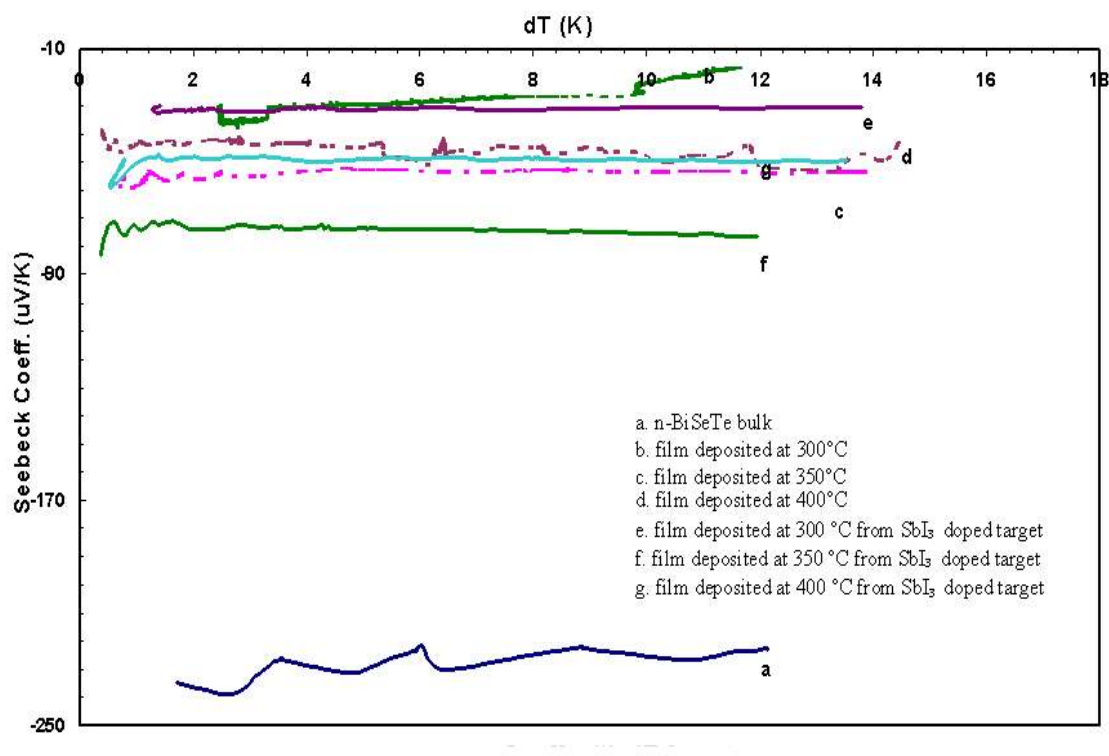


Fig. 4.4.2 Plot of Seebeck coefficient or thermopower as a function of temperature for the n-type films deposited on mica.

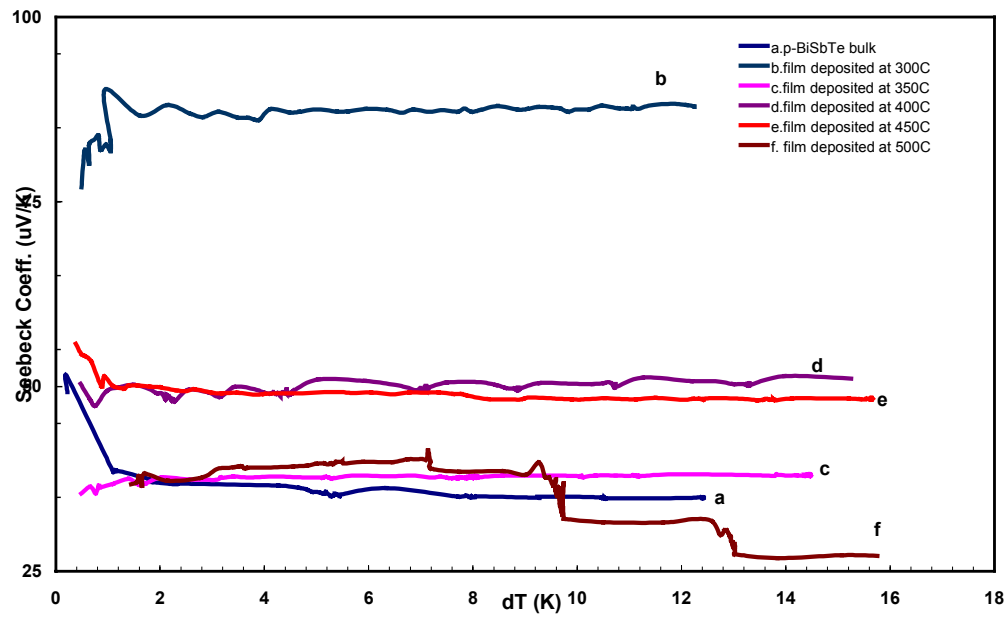


Fig. 4.4.3 Plot of Seebeck coefficient or thermopower as a function of temperature for the p-type films deposited on mica.

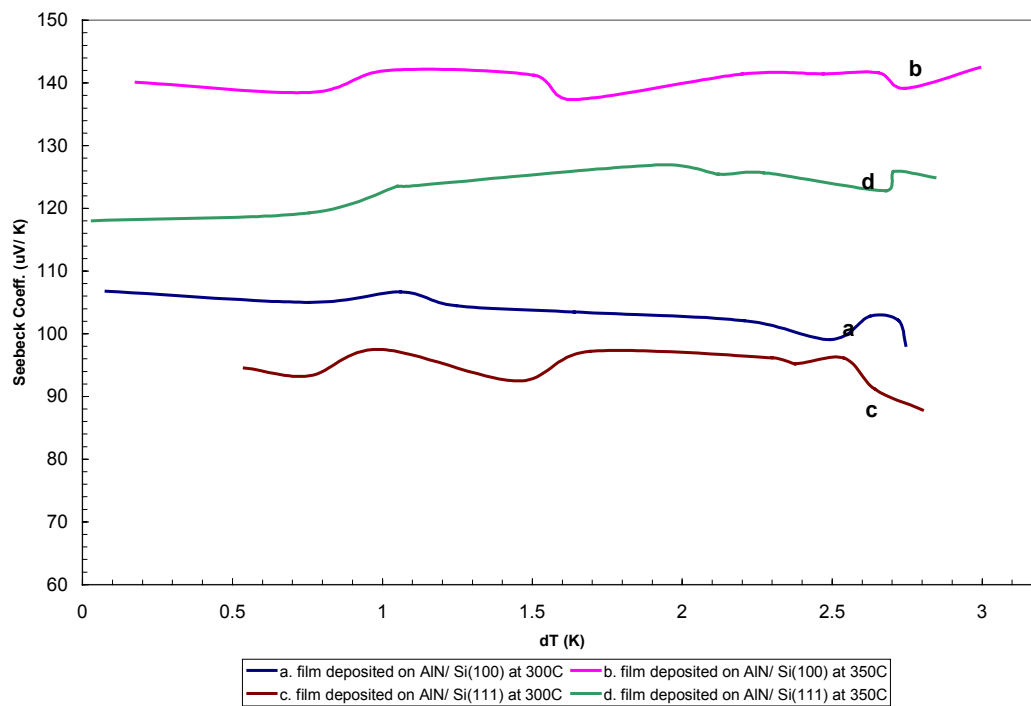


Fig. 4.4.4 Plot of Seebeck coefficient or thermopower as a function of temperature for the p-type films deposited on AlN.

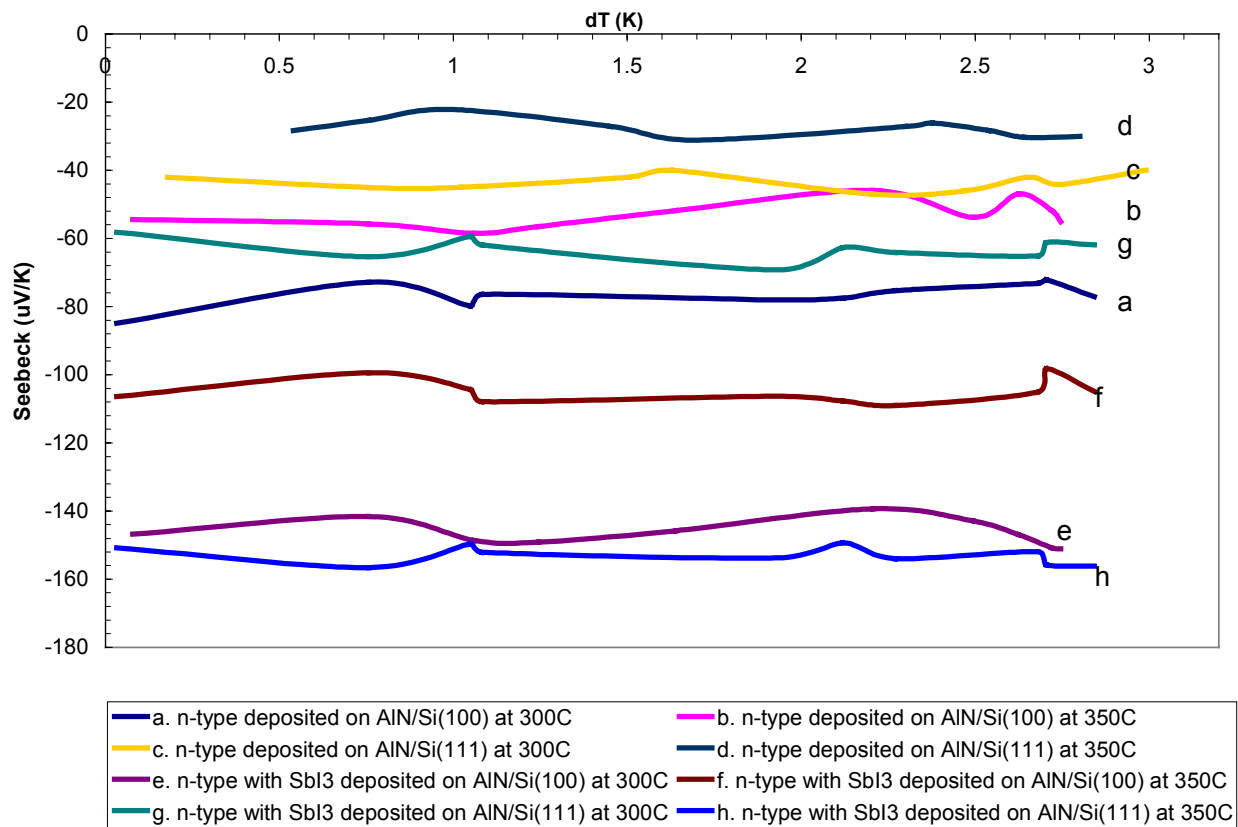


Fig. 4.4.5 Plot of Seebeck coefficient or thermopower as a function of temperature for the n-type films deposited on AlN.

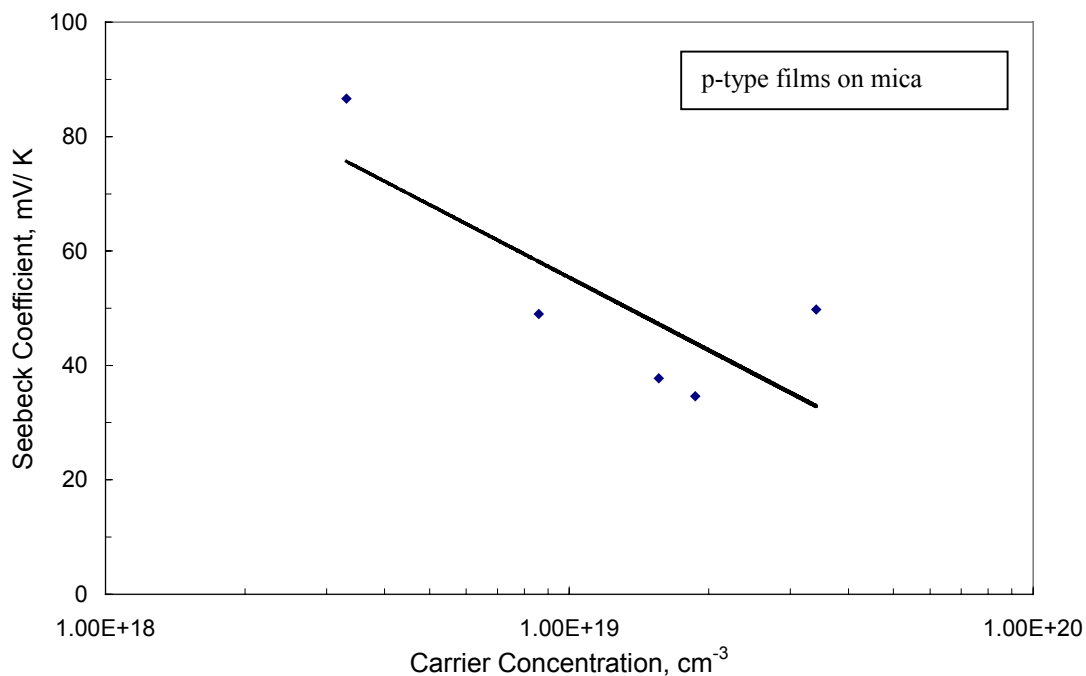


Fig. 5.4.1 Plot of variation of thermoelectric power with carrier concentration for p-type films deposited on mica.

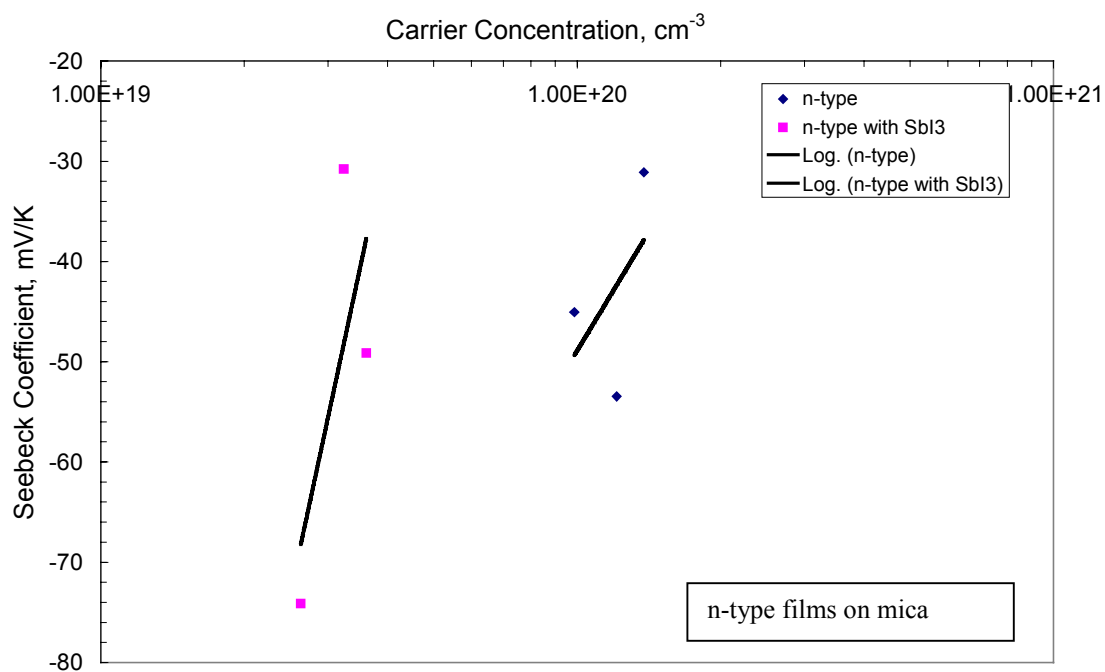


Fig. 5.4.2 Plot of variation of thermoelectric power with carrier concentration for n-type films deposited on mica.

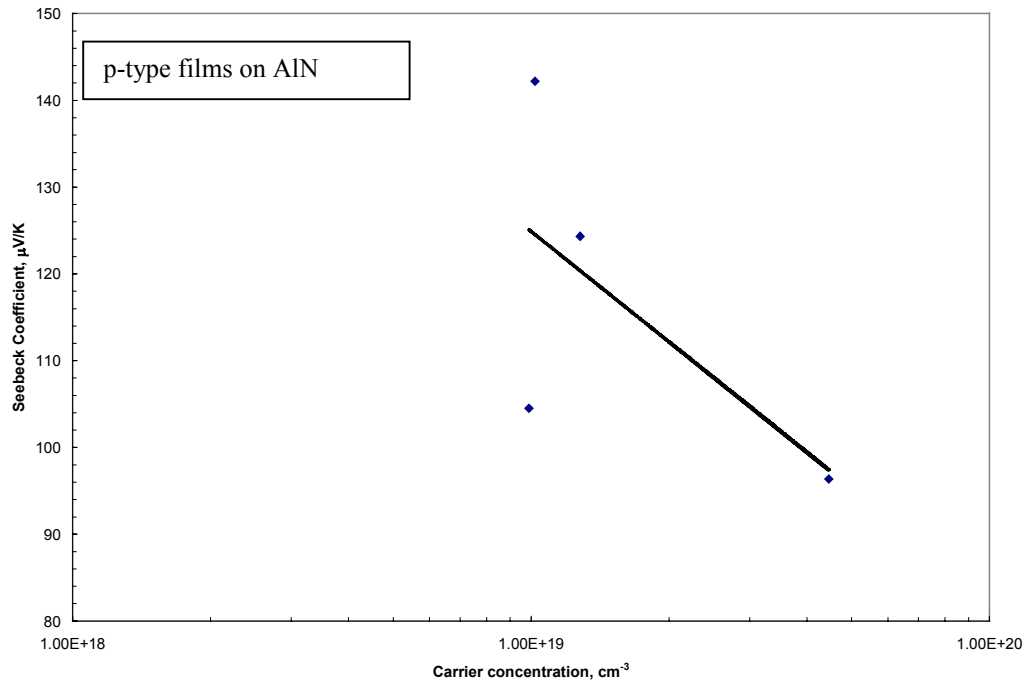


Fig. 5.4.3 Plot of variation of thermoelectric power with carrier concentration for p-type films deposited on AlN.

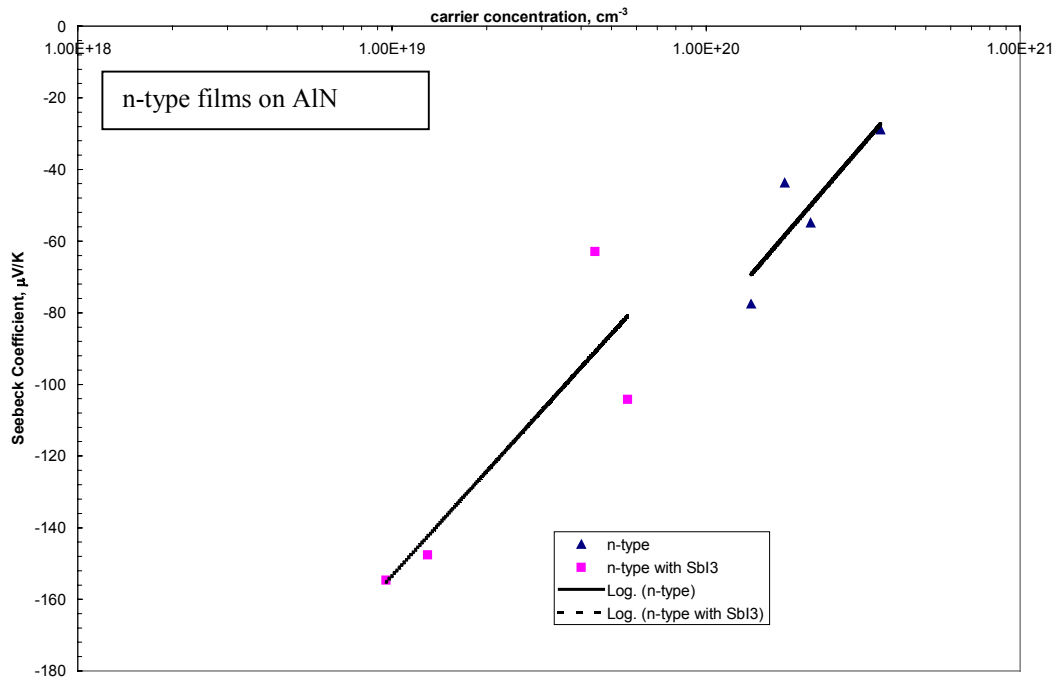


Fig. 5.4.4 Plot of variation of thermoelectric power with carrier concentration for n-type films deposited on AlN.

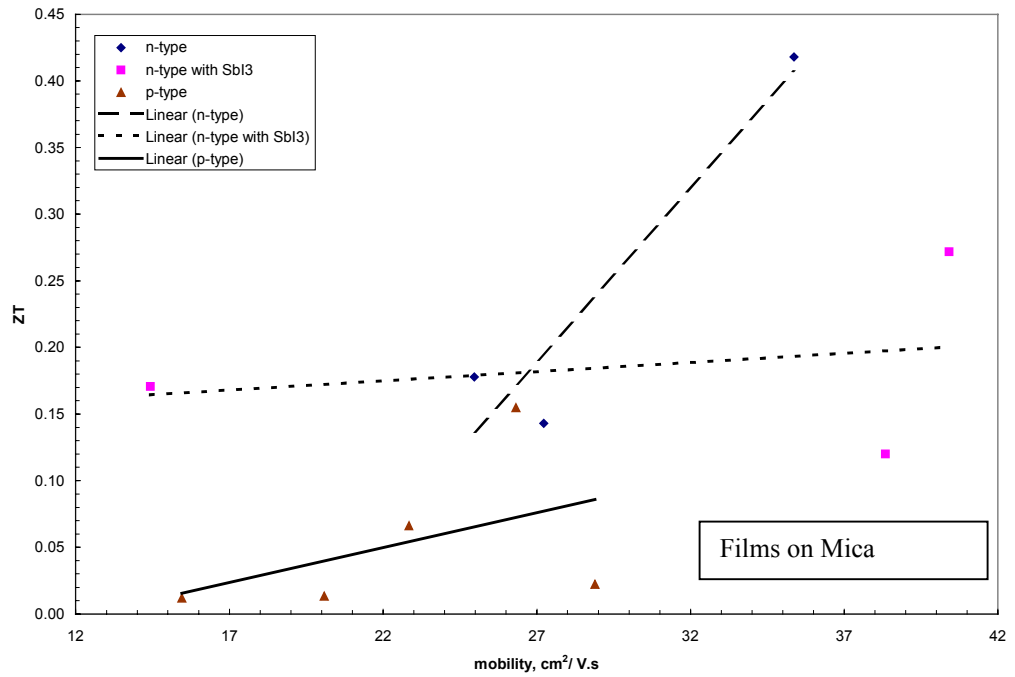


Fig. 5.4.5 Plot of ZT versus carrier mobility for thermoelectric films deposited on mica.

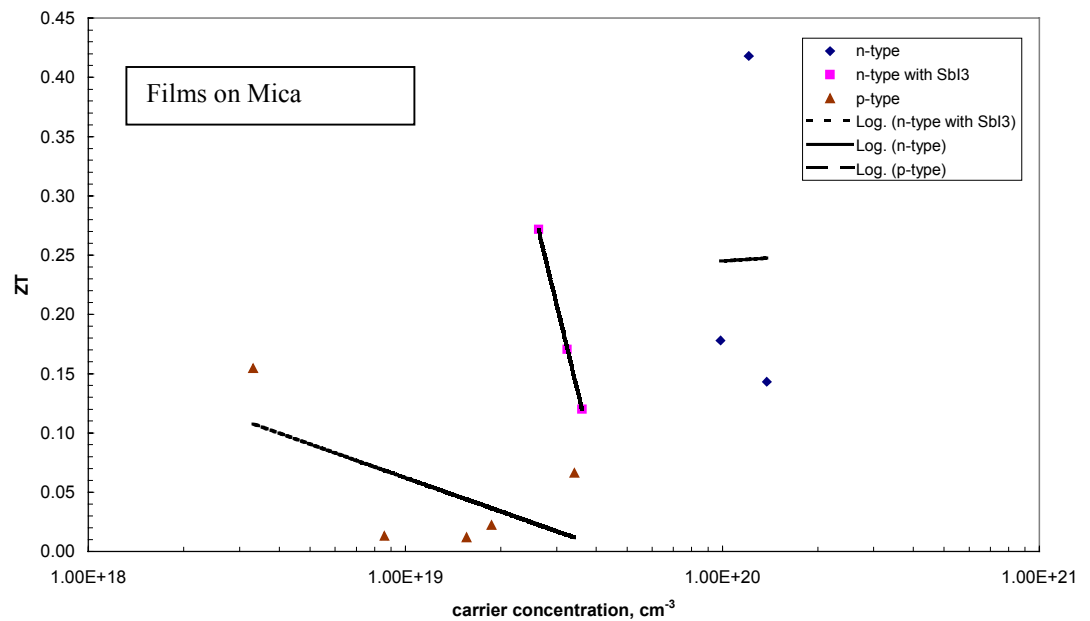


Fig. 5.4.6 Plot of ZT versus carrier concentration for thermoelectric films deposited on mica.

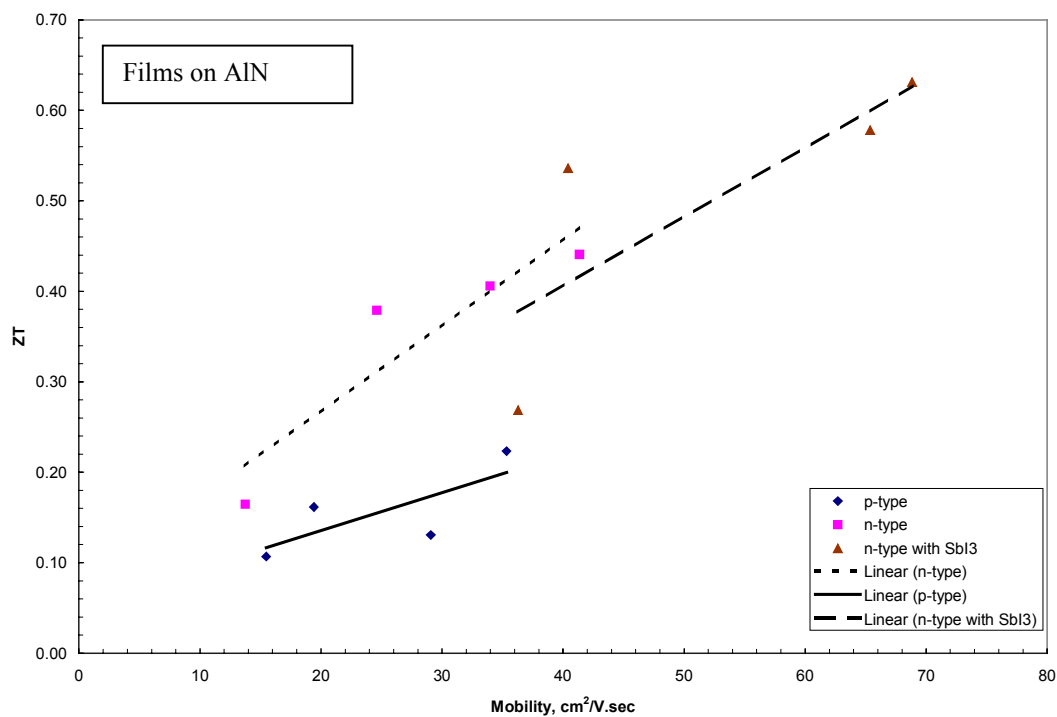


Fig. 5.4.7 Plot of ZT versus carrier mobility for thermoelectric thin films deposited on AlN.

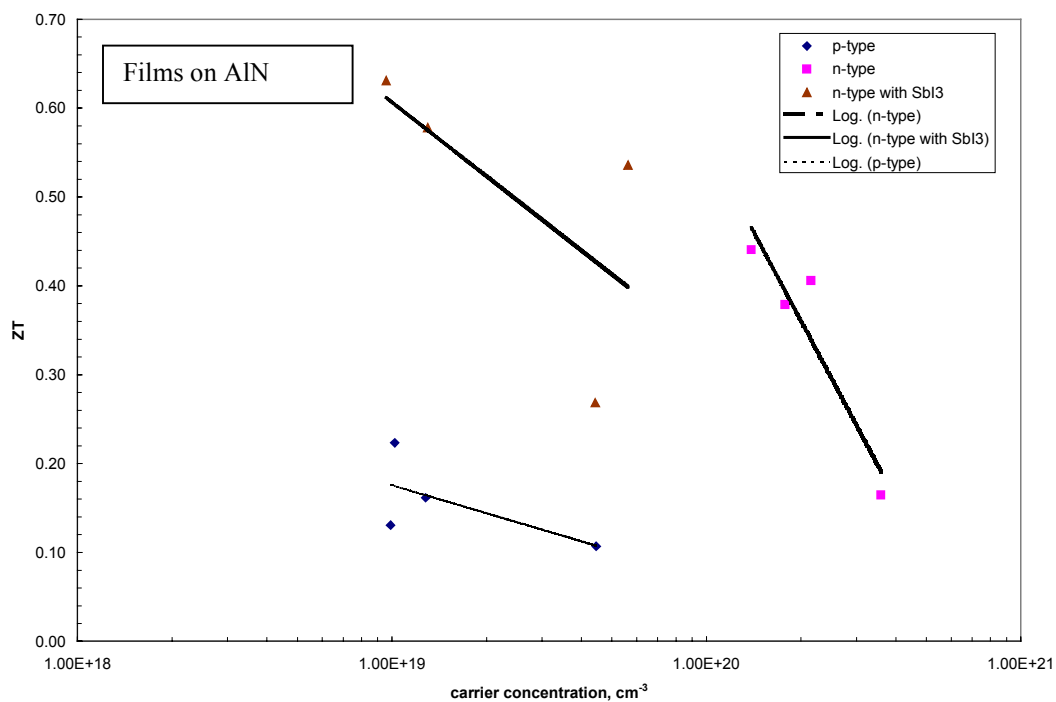


Fig. 5.4.8 Plot of ZT versus carrier concentration for thermoelectric films deposited on AlN.